

Politecnico di Torino

Corso di Laurea Magistrale Ingegneria dei Materiali per l'Industria 4.0
A.a. 2024/2025
Sessione di Laurea Ottobre 2025

Study and development of fusion strategies for support-less manufacturing with Electron Beam Powder Bed Fusion technology

Relatori:

Prof. Damjan Klobčar Prof. Prof. Daniele Ugues Prof. Prof. Cédric Courbon Candidati:

César Villatoro

Abstract

Study and development of fusion strategies for support-less manufacturing with Electron Beam Powder Bed Fusion technology

Cesar Villatoro

Keywords: Powder Bed Fusion

Additive Manufacturing

Electron Beam

Supports
Defects
Porosity
Warping

Overhang regions in Electron Beam Powder Bed Fusion (EB-PBF) are prone to defects like warping, curling or side loss due to poor heat dissipation and residual stresses. Traditionally, defects are mitigated by support structures that introduce material waste and post-processing operations. This study investigates whether adjusting fusion strategies and energy input parameters can reduce overhang defects without the use of supports. A series of experiments were conducted on an ARCAM A1 machine in which multiple fusion strategies, process parameters, energy densities and build themes were studied when building without support structures. Results show that optimized parameters and an optimized fusion strategy of *Quad Islands* can achieve the best results in terms of geometric accuracy, drastically eliminating warping and side loss defects. This improvement, however, comes at the expense of an increase in the part porosity.

Acknowledgments

I would like to acknowledge and thank Prof. Cédric Courbon and Dr. Aurélie Brayet for making Erasmus Mundus meta4.0 possible. I'm very grateful to have been part of the first-ever cohort of this incredible program. This opportunity has helped me grow both professionally and personally.

I would also like to give thanks to all the professors, colleagues and friends I met in Centrale Lyon ENISE, Politecnico di Torino and University of Ljubljana. They had made every moment in France, Italy and Slovenia completely unforgettable and full of memories. Special thanks to Prof. Damjan Klobčar for its advice during the writing of my thesis, and to Prof. Pierre-Thomas Doutre for its guidance during my internship at G-SCOP Laboratory.

Finally, I want to thank my family for their unconditional support and encouragement. To my mother, Marisela, for providing me with love and everything I needed throughout my life. To my second-mother, Maria Eugenia, for taking care of me with boundless love since I was born. To my brother, Diego, for motivating me to improve myself and never give up. And to my girlfriend, Shadia, for always being there when I need it. I love you all.

Table of contents

1	Table of	figures	vii
1	Table of	tables	X
1	Table of	appendices	xi
		mbols used	
	·	bbreviations used	
			2222
1	Intro	duction	1
	1.1 B	ackground of the problem	1
	1.2 O	Objectives	1
	1.2.1	Main objective	
	1.2.2	Specific objectives	2
	1.2.3	Research question	2
2	Theo	retical foundations and literature review	3
	2.1 A	dditive Manufacturing and Powder Bed Fusion technologies	3
	2.1.1	Overview of Metallic Additive Manufacturing	
	2.1.2	Powder Bed Fusion technologies	6
	2.1.3	Comparison between LB-PBF and EB-PBF technologies	8
	2.2 F	undamentals of Electron Beam Powder Bed Fusion (EB-PBF)	9
	2.2.1	EB-PBF process	9
	2.2.2	Advantages and Limitations	11
	2.2.3	Process Parameters	12
	2.3 N	letallurgy of Ti-6Al-4V	13
	2.3.1	Microstructure Formation	14
	2.3.2	Thermal Gradients and Solidification	15
	2.3.3	Mechanical Properties of Ti-6Al-4V	16
	2.4 S	upport structures	17
	2.4.1	Defects formation	17
	2.4.2	Role of support structures	18
	2.4.3	Problematic with supports structures	19
	2.4.4	Alternatives to supports structures	20
3	Resea	arch methodology	21

	3.1 M	laterials	21
	3.1.1	ARCAM A1 EB-PBF machine	21
	3.1.2	ARCAM Ti6Al4V Grade 5 powder	22
	3.1.3	Powder Recovery System (PRS)	23
	3.1.4	Geometry of the part	25
	3.2 P	rocess chain for ARCAM A1 machine	26
	3.2.1	Preparation of digital file	26
	3.2.2	Machine set-up	29
	3.2.3	Manufacturing process	34
	3.2.4	Post-processing of parts	36
	3.3 P	reliminary exploratory work	37
	3.3.1	Set-up for preliminary exploratory work (no powder)	37
	3.3.2	Effect of ARCAM build themes	38
	3.3.3	Melting order of the models	43
	3.4 E	xperimental plan with Melt and Point-net theme	45
	3.4.1	CAD division into small squares (colors)	
	3.4.2	Size of squares	46
	3.4.3	Energy density reduction	47
	3.4.4	Waiting time between melts	47
	3.4.5	Problematic with EBMControl 5.0	48
	3.5 E	xperimental plan with Wafer theme	50
	3.5.1	Controlled waiting time between melts	50
	3.5.2	Fusion strategies with Netfabb	51
	3.5.3	Design of Experiments for Quad Islands strategy	53
	3.6 E	valuation methods to assess part quality	55
	3.6.1	Geometrical accuracy measurement	55
	3.6.2	Measurement of density and porosity	57
4	Resul	ts and Discussion	59
		Results by number of colors	
	4.1.1	•	
	4.1.2	Results by size of squares	
		Results by time between melts	
		Page1ts by different fusion strategies	
	4.2.1 4.2.2	Results by different fusion strategies	
	4.2.2	Effects of Quad Islands parameters	
	4.2.3	Effects of Quan islands parameters	63

5	Conclusions	7 0
Bi	bliography	71
A	ppendix	81

Table of figures

Figure 2.1: ASTM/ISO categories of Additive Manufacturing [3]	4
Figure 2.2: Typical MAM process workflow [4]	
Figure 2.3: Metal Additive Manufacturing Market (2020) [7]	5
Figure 2.4: Overview of the Powder Bed Fusion manufacturing process [16]	7
Figure 2.5: Timeline chart of the evolution of PBF technologies for orthopedics [34]	9
Figure 2.6: Process chain of a typical EB-PBF process [37]	. 10
Figure 2.7: Main components of an EB-PBF machine [42]	. 10
Figure 2.8: Illustration of process parameters in LB-PBF process (applicable for EB-PBF) [56]	. 13
Figure 2.9: Ti-6Al-4V phase diagram [57]	. 13
Figure 2.10: Schematic microstructure of EB-PBF-built Ti-6Al-4V (X-Z plane) [59]	14
Figure 2.11: Optical micrograph of typical bulk EB-PBF Ti-6Al-4V microstructure [60]	14
Figure 2.12: Solidification map for EB-PBF using 6 and 12 mA beam currents [60]	. 15
Figure 2.13: Stress-Strain plots of Ti-6Al-4V samples [62]	16
Figure 2.14: S-N curves of as-fabricated and HIPed Ti-6Al-4V samples [64]	16
Figure 2.15: Types of support structures in PBF	17
Figure 2.16: Overhang warping process [69]	. 17
Figure 2.17: Geometrical defects of overhang part [73]	18
Figure 2.18: Comparison of defects with and without supports in EB-PBF [77]	. 18
Figure 2.19: Support structure failure [80]	19
Figure 2.20: Undesired marks due to supports removal [82]	19
Figure 3.1: ARCAM A1 machine [92]	21
Figure 3.2: ARCAM A1 chamber	. 22
Figure 3.3: ARCAM Powder Recovery System (PRS)	. 24
Figure 3.4: Vacuum cleaner for Ti6Al4V powder	24
Figure 3.5: Sieving cabinet for Ti6Al4V powder	. 24
Figure 3.6: Geometry of the part for experiments (dimensions in mm)	. 25
Figure 3.7: Isometric view of part	. 25
Figure 3.8: Example of identification marks (cuboids)	. 25
Figure 3.9: CAD in Onshape software	26
Figure 3.10: Part positioning in Rhinoceros 3D	. 26
Figure 3.11: Part slicing in Grasshopper	. 27
Figure 3.12: ARCAM Build Assembler software	. 27
Figure 3.13: Slicing in Autodesk Netfabb software	. 28
Figure 3.14: Workflow for digital file generation	. 28
Figure 3.15: "Build" window in EBMControl	. 29
Figure 3.16: "Process" window in EBMControl	. 29
Figure 3.17: Placing of the build plate	30
Figure 3.18: Calibration of the rake	30

Figure 3.19: Placing of the heat shield	31
Figure 3.20: "Hardware" window in EBMControl	31
Figure 3.21: "Center Beam" window in EBMControl	32
Figure 3.22: Process of beam centering	32
Figure 3.23: "Align Beam" window in EBMControl	33
Figure 3.24: Process of beam alignment	33
Figure 3.25: Workflow for machine set-up	33
Figure 3.26: Initial build plate heating	34
Figure 3.27: Pre-heating process	34
Figure 3.28: Selective melting of a part	35
Figure 3.29: Spreading of powder for a new layer	35
Figure 3.30: Workflow for manufacturing process	36
Figure 3.31: Depowdering in ARCAM PRS	36
Figure 3.32: ARCAM A1 as a black-box system	37
Figure 3.33: Vacuuming of powder for preliminary experiments	38
Figure 3.34: Snapshots of the experiments without powder	38
Figure 3.35: Melt Build Theme process parameters	39
Figure 3.36: Melt theme beam trajectory	40
Figure 3.37: Point-Net Build Theme process parameters	41
Figure 3.38: Point Net theme beam trajectory	41
Figure 3.39: Wafer Build Theme process parameters	42
Figure 3.40: Wafer theme beam trajectory	42
Figure 3.41: Geometry used for studying melting order	43
Figure 3.42: Melting parts at the same time	44
Figure 3.43: Melting parts at configured order	44
Figure 3.44: Part division into subparts (colors)	45
Figure 3.45: Patterns with different amount of colors	45
Figure 3.46: Patterns with different square sizes	46
Figure 3.47: Pattern for waiting times between melts	48
Figure 3.48: Set-up for time between melts (Melt theme)	48
Figure 3.49: Set-up for time between melts (Wafer theme)	50
Figure 3.50: Fusion strategies for first set of experiments with Netfabb	52
Figure 3.51: Parameters studied for DOE of Quad Islands strategy	53
Figure 3.52: Physical set-up for the 3D scanning of the parts	55
Figure 3.53: Aligning and merging of scans	56
Figure 3.54: Scalar field between scanned part and its CAD	56
Figure 3.55: Analytical balance used for measurements	57
Figure 3.56: Physical set-up for measuring density	57
Figure 4.1: Results of measured porosity vs number of colors	
Figure 4.2: Results of measured porosity vs size of squares	60
Figure 4.3: Results of measured porosity vs energy density	61

Figure 4.4: Results of measured porosity vs time between melts	61
Figure 4.5: Results of measured porosity vs different fusion strategies	62
Figure 4.6: Results of measured deviation vs different fusion strategies	63
Figure 4.7: Results by different fusion strategies (pictures)	63
Figure 4.8: Results of measured porosity in Quad Islands strategy	64
Figure 4.9: Results of measured max deviation in Quad Islands strategy	64
Figure 4.10: Results by Quad Island strategy (pictures)	65
Figure 4.11: Main effects plots for porosity and deviation	66
Figure 4.12: Interaction plots for porosity and deviation	67
Figure 4.13: 3D Surface graph for models	69

Table of tables

Table 2.1: Key differences between LB-PBF and EB-PBF technologies [30]	8
Table 2.2: Advantages and disadvantages of EB-PBF technology [49]	12
Table 3.1: Characteristics of ARCAM A1 machine [93]	22
Table 3.2: Chemical composition of ARCAM Ti6Al4V powder [94]	23
Table 3.3: Mechanical properties of ARCAM Ti6Al4V powder [95]	23
Table 3.4: Experimental plan for studying different number of colors	46
Table 3.5: Experimental plan for studying different square sizes	47
Table 3.6: Experimental plan for studying lower energy densities	47
Table 3.7: Process parameters for ARCAM Melt theme	49
Table 3.8: Process parameters for ARCAM Point-Net theme	49
Table 3.9: Process parameters for ARCAM Wafer theme	50
Table 3.10: Experimental plan for studying waiting times between melts with Wafer theme	51
Table 3.11: Experimental plan for studying different fusion strategies with Netfabb	53
Table 3.12: Factors and levels for the DOE	54
Table 3.13: Experimental plan for studying Quad Islands strategy	54

Table of appendices

Appendix A: Table of all manufactured parts and their process parameters	81
Appendix B: Table of parts with their measured density and porosity	82
Appendix C: Table of parts with their measured geometric deviation	83
Appendix D: Scalar fields between all scanned part and their CAD	84
Appendix E: Pictures of all manufactured parts	86

List of symbols used

-		
Symbol	Unit	Meaning
d	mm	gap distance
h	mm	hatch distance
I	mA	beam current
m	g	mass
P	%	porosity
S	mm	square size
t	ms	time
ť'	mm	layer thickness
U	kV	acceleration voltage
v	mm/s	scan speed
VED	J/mm^3	volumetric energy density
ho	g/cm ³	density
Indexes		
0	initial	
air	dry	
H2O	water	
on	spot	
sub	submerged	

List of abbreviations used

Abbreviation	Meaning
11001011111011	1120111115
2FI	Two-Factor Interaction
ABF	ARCAM Build File
AM	Additive Manufacturing
ANOVA	Analysis of Variance
ASTM	American Society for Testing and Materials
BBD	Box-Behnken Design
CAD	Computer-Aided Design
CAM	Computer-Aided Manufacturing
CLF	Common Layer File
CNC	Computer Numerical Control
DMLS	Direct Metal Laser Sintering
DOE	Design of Experiments
EB	Electron Beam
EBM	Electron Beam Melting
FGM	Functionally Graded Materials
HIP	Hot Isostatic Pressing
ISO	International Organization for Standardization
LB	Laser Beam
MAM	Metal Additive Manufacturing
OFAT	One-Factor-At-a-Time
PBF	Powder Bed Fusion
PRS	Powder Recovery System
RMS	Root Mean Square
RSM	Response Surface Methodology
SD	Standard Deviation
SF	Speed Function
SHS	Selective Heat Sintering
SLM	Selective Laser Melting
SLS	Selective Laser Sintering
STL	Standard Tessellation Language

1 Introduction

1.1 Background of the problem

In Electron Beam Powder Bed Fusion (EB-PBF), overhangs are particularly challenging to fabricate due to the lack of solid underlying material, leading to poor heat dissipation, thermal gradients, and resulting defects such as sagging, warping, and surface irregularities. Traditionally, support structures are used to mitigate these issues by providing mechanical and thermal stabilization. However, supports introduce several drawbacks: they increase material waste, prolong processing times, degrade surface finish, and often leave unwanted marks on the part that requires post-processing. While support minimization strategies have been explored extensively in Laser Powder Bed Fusion (LB-PBF), the EB-PBF process remains underexplored, with limited research focusing on optimizing fusion strategies and energy input to enable support-free manufacturing. This gap motivates the investigation of whether modifying process parameters and fusion strategies can effectively reduce overhang defects without relying on support structures in EB-PBF, thereby improving efficiency of the process.

1.2 Objectives

The objectives of this work are presented by main and specific objectives; and are synthesized in a final research question.

1.2.1 Main objective

The main objective is to study different fusion strategies and energy densities with the objective of fabricating parts without support structures with the highest possible geometrical accuracy and evaluate their influence on the material properties of the parts with EB-PBF technology.

1.2.2 Specific objectives

- Investigate and evaluate different methods to apply different fusion strategies in an ARCAM A1 machine.
- Measure the magnitude of the geometrical defects and mechanical properties with the equipment available in the laboratory: 3D scanner and analytical balance.
- Study the effect of different process parameters in the developing of geometrical defects and evolution of mechanical properties when manufacturing without support structures.
- Find a fusion strategy that potentially reduces the geometrical defects and evaluate its impact on the mechanical properties.

1.2.3 Research question

• Can overhang defects be reduced by applying different fusion strategies and modifying the energy density when manufacturing without supports in an ARCAM A1 machine?

2 Theoretical foundations and literature review

2.1 Additive Manufacturing and Powder Bed Fusion technologies

Additive Manufacturing (AM) is one of the key technologies in the industry 4.0 because it allows the production of parts that are not possible by any other technology, also it helps to reduce material waste and improve functionality. It consists of joining materials typically layer by layer by applying different techniques depending on the technology. Additive manufacturing brings together a range of advanced technologies including computer-aided design (CAD), computer-aided manufacturing (CAM), laser and electron beam energy systems, CNC (computer numerical control) machining, and laser scanning. While many of these technologies originated as early as the 1950s, it wasn't until the 1980s that their development reached a level of maturity that made additive manufacturing possible.

Additive manufacturing initially emerged with materials like polymers, waxes, and laminated paper, primarily serving as a tool for rapid prototyping, which aligns with its initial focus. By the 1990s, the first commercial systems were already introduced to the market. Today, the technology has evolved to create functional parts, many of which utilize advanced materials such as ceramics, composites, and metals [1], [2].

Additive Manufacturing (AM) technologies can be categorized in several ways depending on specific criteria such as the method of material deposition, the type of energy source used for material fusion, or the underlying operating principles of the process. Nevertheless, the most widely accepted classification system is the one defined by the International Organization for Standardization (ISO) and the American Society for Testing and Materials (ASTM). According to this framework, AM processes are grouped into seven distinct categories, each representing a different technological approach to building parts layer by layer. Figure 2.1 shows the seven categories established by the framework of ASTM and ISO.

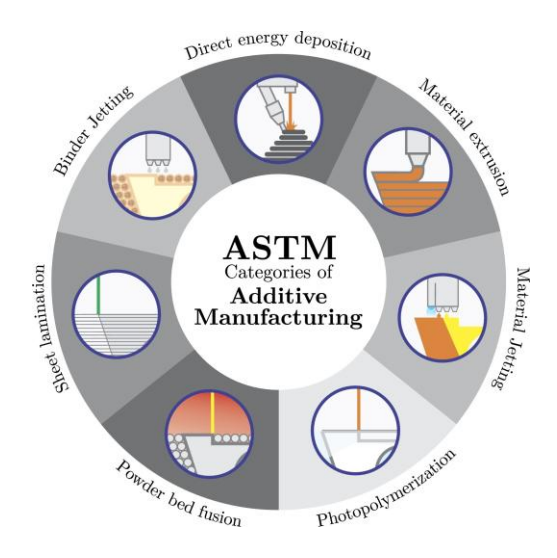


Figure 2.1: ASTM/ISO categories of Additive Manufacturing [3]

2.1.1 Overview of Metallic Additive Manufacturing

Metal Additive Manufacturing (MAM) refers to the technologies of Additive Manufacturing applied directly to metallic materials. Among the diverse technologies developed for various materials, metal additive manufacturing (MAM) stands out as the one that has made the greatest impact across a wide range of industries. Among some of the most common applications, it can be found implants for biomedical industry, heat exchangers in avionics and engines for aerospace industry [4].

The metal additive manufacturing process begins with the creation of a 3D CAD model that digitally represents the final product, including not only its external geometry but also internal features such as infills and support structures. Once the design is finalized, it must be converted into a format that can be interpreted by the manufacturing machine, typically by exporting it as a standard tessellation language (STL) file. This file is then transferred to the machine or a slicing software, which slices the 3D model into 2D layers and generates toolpaths or G-code for fabrication. Before printing, the machine must be configured with appropriate process parameters depending on the technology used such as part orientation, layer thickness, and support structures, which typically can also be adjusted within the slicing software. The printing stage itself varies by technology and can take anywhere from hours to days, requiring minimal human intervention beyond occasional monitoring. After printing, parts are removed from the build platform and may undergo additional steps such as debinding or sintering, depending on the material and process used. Optional postprocessing steps can include machining to improve tolerances or surface finish, heat treatment to relieve internal stresses or enhance mechanical properties (e.g., via HIP, annealing, or aging), and inspection using non-destructive testing methods like X-ray, ultrasonic, or surface roughness analysis. Finally, after quality control is complete, the part is handed over for its intended use. Figure 2.2 summarizes the typical workflow for MAM technologies.

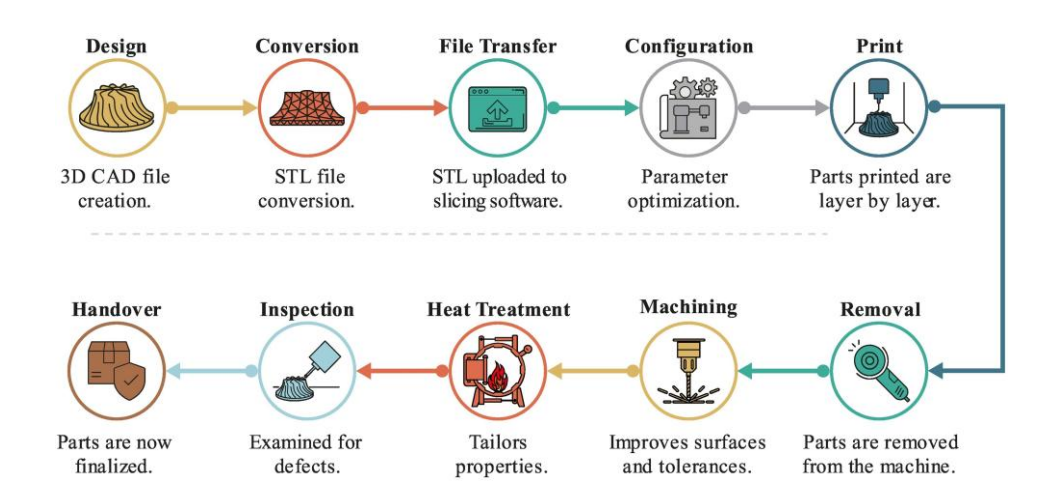


Figure 2.2: Typical MAM process workflow [4]

ASTM/ISO 52900:2021 [5] categorizes the Metal Additive Manufacturing technologies in 4 groups: Material Extrusion (ME), Binder Jetting (BJ), Directed Energy Deposition (DED) and Powder Bed Fusion (PBF). Out of these 4 technologies, Powder Bed Fusion (PBF) is the most widely used in industry. Some of the most common applications include aerospace, medical, automotive, industrial, tooling, and consumer goods [6]. Figure 2.3 shows the market for MAM technologies, where PBF technologies hold more than half of the share.

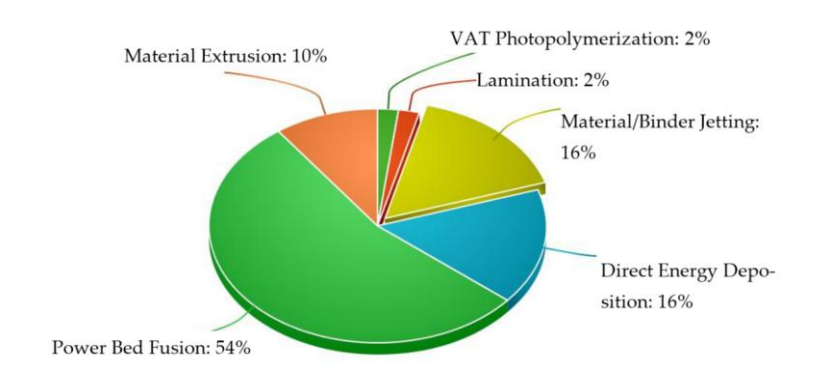


Figure 2.3: Metal Additive Manufacturing Market (2020) [7]

Metal Additive Manufacturing is projected to continue growing in market in the following years. With the arrival of Industry 4.0 and Industry 5.0, every industrial sector will be making significant efforts to move away from traditional methods of manufacturing to the adoption of disruptive technologies like AM. Several factors make MAM extremely attractive for industry, but one of the most important is the fact that MAM enables on-demand production of parts, significantly reducing the need to maintain large inventories of spare components. It also shortens lead times, especially for critical or hard-to-find obsolete parts, by allowing rapid fabrication directly from digital files [8].

Compared to traditional methods, MAM significantly lowers production costs and shortens development time, allowing quicker design iterations and speeding up the entire product development cycle. For instance, components like molds that typically take 4–6 months to produce conventionally can be completed in just 2–3 months using MAM. This enables fast and cost-effective production of functional prototypes, making it ideal for on-demand

prototyping [9]. Additionally, the creation of highly complex geometries doesn't necessarily mean increased production costs like in traditional methods. This is how the very well know statement "with AM, complexity is for free" delivers other great advantage for the usage of MAM technologies. However, this freedom has limits; certain complex features, like overhangs, can introduce challenges such as residual stresses or defects due to process constraints in MAM [10].

In other hand, AM simplifies the supply chain and offers a cost-effective solution for low-volume, niche production, which is often too expensive with traditional manufacturing methods. Unlike conventional manufacturing, where each part may require custom molds and high initial investment, MAM eliminates the need for specialized tooling, significantly reducing fixed costs. This makes it easier to reach profitability even at smaller production scales. While MAM still lags behind traditional techniques like casting and forging for mass production, it excels in low-volume applications due to faster turnaround and fewer supply chain dependencies. As material costs decrease and AM supply chains mature, its use in limited-run manufacturing is expected to grow steadily in the following years [11].

Another great advantage of the usage of MAM is the production of lightweight structures, which lowers material usage and decreases energy consumption. MAM in combination with techniques like topology optimization and lattice structure design, enables the creation of high strength yet lightweight parts that are difficult or impossible to produce using traditional methods. MAM also allows the production of functionally graded materials (FGMs) and functionally graded structures (FGSs), where material composition or density can be gradually varied within a part to meet specific performance requirements [12].

The capability to visualize and produce highly intricate geometries, coupled with greater design freedom and minimal raw material waste, are just some of the many advantages that make MAM highly suitable across a wide range of industries. Despite these strengths, several challenges still limit its widespread adoption and highlight the need for continued research and development. Constraints such as limited material availability, restricted build volumes, anisotropic mechanical properties, reduced structural integrity, and surface imperfections like the staircase effect remain significant barriers for its full development. Nevertheless, the potential of AM, particularly in terms of sustainability, material efficiency, and functional performance, makes it a powerful and increasingly indispensable tool in modern manufacturing [13].

2.1.2 Powder Bed Fusion technologies

Powder bed fusion (PBF) is a category of Metal Additive Manufacturing (MAM) techniques in which a directed energy source selectively binds or melts metal powder particles, layer by layer, to create parts with precise geometric specifications. PBF can be divided into multiple categories. The types of PBF processes are: Selective Laser Sintering (SLS), Selective Laser Melting (SLM), Direct Metal Laser Sintering (DMLS), Selective Heat Sintering (SHS) and Electron Beam Melting (EBM) [14].

Regardless of the PBF technology, all the processes follow the same overall steps: The 3D model of the desired part is divided into multiple horizontal slices, and each layer is produced as a flat 2D cross-section, stacked sequentially to form the final component. In Powder Bed Fusion (PBF), a fine layer of material powder is evenly spread across the build platform

using a roller, scraper or blade. Then, the laser or electron beam selectively melts or sinters the desired area of that layer based on the part's geometry. Once the material is solidified, the platform lowers slightly to accommodate a new powder layer, and the process repeats again layer by layer [15]. Figure 2.4 shows an overview of a simple PBF system, highlighting the main components of a typical PBF machine.

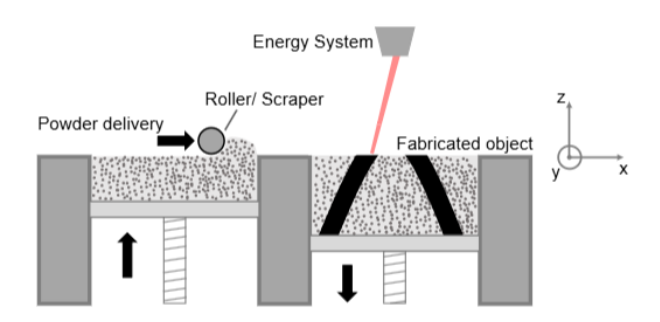


Figure 2.4: Overview of the Powder Bed Fusion manufacturing process [16]

Selective Laser Sintering (SLS) refers to a PBF technology that uses a laser to sinter a mixture of powder consisting of a low meting point powder and another with high melting point, fusing particles together without fully melting them. It is typically used for polymer materials [17]. Selective Laser Melting (SLM) refers to other PBF technology, that uses a high-power laser that fully melts the powder material, which leads to fully dense parts, it is typically used for metals, and it is performed in an inert atmosphere [18]. In the other hand, Direct Metal Laser Sintering (DMLS) is very similar to SLM, but it was originally developed for sintering rather than full melting, it is especially useful for processing non-weldable or crack-prone alloys, however, nowadays DMLS also achieve full melting like SLM [19]. Selective Heat Sintering (SHS) refers to a PBF technology that uses a thermal print head instead of a laser to selectively sinter layers of powder, it is considered a low-cost AM technique and is often used for polymer materials, in the same way as SLS [20]. Finally, Electron Beam Melting (EBM) uses a beam of electrons as a heat energy source to melt a metal powder. In EB-PBF, contrary to other PBF technologies, a high vacuum and high temperature is maintained in the chamber during the build process [21].

The PBF technologies normally used for processing metal powders are typically LB-PBF (SLM) and EB-PBF (EBM). These two technologies achieve the melting point of the material, therefore, achieving a much higher density compared to the powder sintering PBF technologies like DMLS, SLS, and SHS [22]. When Metal Additive Manufacturing (MAM) is discussed, LB-PBF and EB-PBF are the typically considered technologies in this category [23].

According to standard ISO/ASTM 52900:2021 [5], the official terminology for Electron Beam Melting (EBM) is Powder Bed Fusion-Electron Beam/Melting (PBF-EB/M), and for laser-based processes like Selective Laser Melting (SLM), it is Powder Bed Fusion-Laser Beam/Melting (PBF-LB/M). The term SLM, which is used as a synonym of LB-PBF, originated in the late 1990s through research at the Fraunhofer Institute for Laser Technology (ILT) in Germany, and was later commercialized by companies such as SLM Solutions to describe the full melting of metal powders using a laser [24]. Despite the formal adoption of PBF-based terminology, SLM/LB-PBF and EBM/EB-PBF are often used interchangeably

in scientific literature and industry. However, in this work, the terms EB-PBF and LB-PBF will be used for clarity and consistency.

2.1.3 Comparison between LB-PBF and EB-PBF technologies

As mentioned before, both LB-PBF and EB-PBF technologies are the main metal PBF technologies. Both technologies achieve the melting point of the material and are quite similar in terms of the overall PBF process. However, key differences are identified between LB-PBF and EB-PBF technologies. For instance, using electron beam as an energy source was first introduced to overcome the laser limitations of speed and power. Electron Beam produces much higher power, around 3000 W with standard machines from ARCAM, in comparison to the 400 W with standard machines from EOS. Both ARCAM and EOS are common industrial manufacturers of PBF machines. In the other hand, since an Electron Beam doesn't depend on mechanical optical systems like a Laser Beam, the beam speed can be much faster, achieving around 8000 m/s in Electron Beam technologies (ARCAM) against around 7 m/s in Laser technologies (EOS). This difference in power and speed, can allow Electron Beam technologies to have a much shorter build time than Laser technologies [25], [26].

Another important difference between EB-PBF and LB-PBF is the typical layer thickness used. EB-PBF uses larger layer thickness, which also contributes to shorter build times, but results in rougher surfaces and less dimensional accuracy compared to LB-PBF. In terms of the atmosphere required for the process, LB-PBF uses a chamber at ambient pressure filled with an inert gas like Argon or Nitrogen to prevent reactions, while EB-PBF requires to be performed under high vacuum with a partial pressure of Helium, this is because the presence of air molecules can scatter the electron beam reducing its precision [27].

For the build plate, EB-PBF uses preheating in the build plate throughout the process where temperature is kept at a higher level in order to reduce thermal gradients in the part. Therefore, EB-PBF process typically has lower cooling rates and lower residual stresses, which reduces the need for heat treatments, in contrast with LB-PBF which uses a cold plate during the fabrication [28]. This characteristic of EB-PBF also allows it to require, in general, fewer support structures for the building of overhang parts, something that is strictly necessary in SLM technology, which relies heavily on the usage of support structures for heat dissipation and structural integrity during fabrication [29]. Table 2.1 summarizes the key differences.

Table 2.1: Key differences between LB-PBF and EB-PBF technologies [30].

Technology	LB-PBF	EB-PBF
Energy source	Laser beam	Electron beam
Scanning mechanism	Galvanometers	Deflection coils
Atmosphere	Argon, Nitrogen	Vacuum
Beam spot size	0.1 mm - 0.5 mm	0.2 mm - 1.0 mm
Scanning speed	~ 10 m/s	$\sim 8000 \text{ m/s}$
Build rate	50 cm ³ /h	$55-80 \text{ cm}^3/\text{h}$
Surface finish	$Ra = 9-12 \mu m$	$Ra = 25-35 \mu m (min)$
Residual stresses	High	Minimal
Particle size	15-45 μm	45-106 μm
Particle shape	Spherical	Spherical
Powder bed temperature	100-200°C	600-1100 °C

2.2 Fundamentals of Electron Beam Powder Bed Fusion (EB-PBF)

Electron Beam Powder Bed Fusion (EB-PBF) is a metal additive manufacturing process under the powder bed fusion (PBF) category that utilizes a high-power electron beam to selectively melt metal powder in a vacuum chamber. EB-PBF is especially well-suited for producing structural components and biomedical implants due to its ability to process reactive metals like titanium in a vacuum environment. Some common applications include orthopedic implants, aerospace components and Turbomachinery and Heat-Resistant Parts [31], [32].

Historically, the electron beam itself has been applied in metallurgy since the mid-20th century, but its application in layer-by-layer manufacturing evolved alongside developments in computational control and powder metallurgy. The EB-PBF technology became commercially viable in 1997, with Arcam AB (Sweden) being the first to introduce EB-PBF systems designed specifically for AM applications [33]. In the last years, EB-PBF technology has evolved, leading in 2007 to the first acetabular component produced using EB-PBF to obtain the CE-certification [34]. Figure 2.5 shows a timeline chart of the evolution of PBF, especially EB-PBF technology.

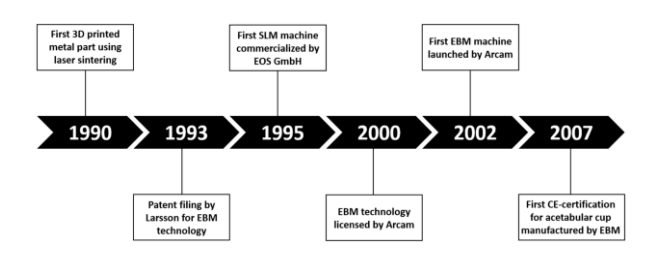


Figure 2.5: Timeline chart of the evolution of PBF technologies for orthopedics [34]

2.2.1 EB-PBF process

The EB-PBF process begins with the spreading of a thin layer of metal powder onto a build platform. The electron beam, controlled by electromagnetic coils, scans the powder bed according to the sliced CAD data of the 3D model. Before melting, a preheating phase is executed, where the entire layer is sintered to reduce thermal gradients and minimize powder charging, a phenomenon where particles become electrically charged due to the interaction with the high-energy electron beam. This is essential due to the insulating nature of the powder and the high energy of the beam [35].

After melting, the molten metal rapidly solidifies as it cools, fusing with the underlying layer to form a strong metallurgical bond. Once the layer is complete, the build platform is lowered by a predetermined layer thickness, often between 50 to 100 microns, preparing the system for the next deposition cycle. Then the platform is lowered, and a new layer of metal powder is distributed evenly across the build surface using a recoater or rake mechanism. This process continues until the part is fully built [36]. The vacuum environment used in EB-PBF minimizes oxidation and is particularly well-suited for reactive metals. Figure 2.6 shows a picture of the process chain of a typical EB-PBF process. The process is repeated layer by layer until the last layer of the part is fabricated.

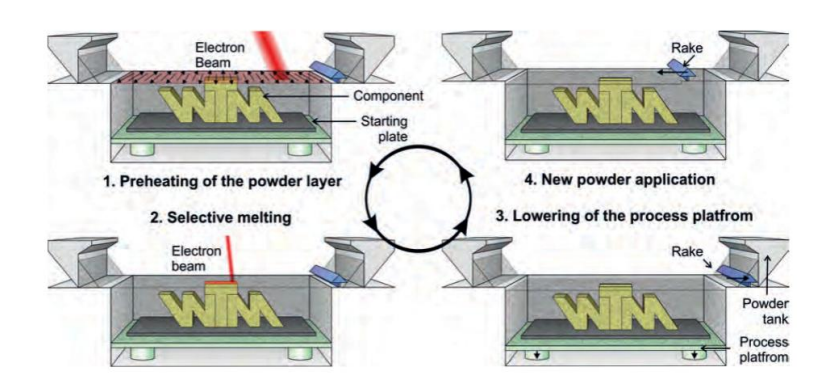


Figure 2.6: Process chain of a typical EB-PBF process [37]

The main components of an EB-PBF machine are described as the following: The Electron Beam column is a vertical structure that houses the entire beam generation system. It includes the filament, which is a tungsten wire that thermionically emits electrons when heated, these electrons form the basis of the electron beam which is accelerated by a voltage of typically 60 kV [38]. The astigmatism lens corrects the asymmetry in the beam's shape, ensuring a circular and focused spot. The focus lens concentrates the electron beam to a fine spot, critical for energy density and resolution during melting. Finally, the deflection lens directs the beam across the powder bed in X and Y directions, enabling the selective melting [33].

The heat shield protects sensitive components from the intense thermal radiation and reflected heat within the vacuum chamber during operation [35]. The vacuum chamber maintains a high-vacuum environment (~10⁻⁵ mbar) to prevent oxidation of reactive metals like titanium and to allow unscattered beam propagation. It encloses the build platform, hoppers, and rake system [39]. The powder hoppers store the pre-alloyed powder, and they dispense precise layers of powder across the build area after each melting cycle [40]. Then the rake spreads powder from the hoppers evenly onto the build platform. A consistent layer thickness essential for uniform part formation [41]. Figure 2.7 illustrates the main components of an EB-PBF machine.

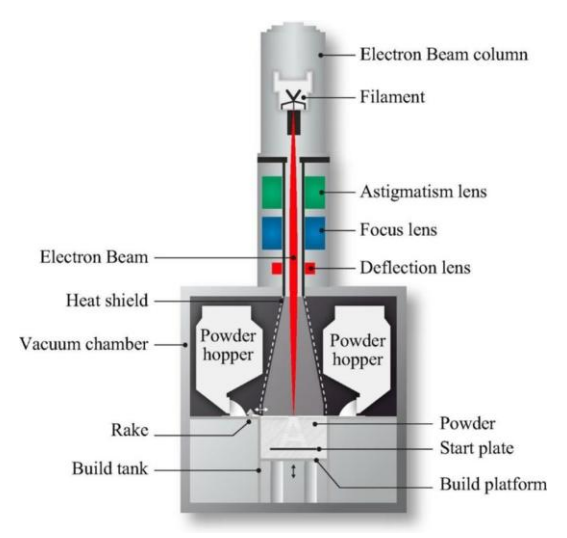


Figure 2.7: Main components of an EB-PBF machine [42]

2.2.2 Advantages and Limitations

The specific characteristics of EB-PBF offer a series of advantages compared to other Metal Additive Manufacturing technologies. Some of them are:

- High build temperature reduces residual stresses: EB-PBF operates at elevated temperatures (up to 1000 °C), resulting in lower thermal gradients. This helps relieve internal stresses during fabrication, minimizing distortion and often eliminating the need for support structures and post-processing steps [33].
- Excellent material utilization and recyclability: Unmelted powder is recoverable and reusable, thanks to the vacuum environment which limits contamination, making EB-PBF highly material efficient [43].
- Ideal for reactive metals: The vacuum chamber prevents oxidation, making EB-PBF particularly suitable for reactive alloys such as titanium and Inconel, especially in aerospace and biomedical implants [35].
- Complex geometries without tooling: EB-PBF can produce intricate geometries and lattice structures directly from CAD without the need for dies, molds, or cutting tools, reducing lead times and costs [44].
- Full density components: With proper parameters, EB-PBF can achieve >99.9% dense parts, comparable to wrought or cast materials in mechanical properties [45].

However, EB-PBF technology often presents some problems when it is applied, which are described due to its following limitations:

- Surface roughness and post-processing needs: Due to partially sintered powder and high energy input, EB-PBF parts often exhibit high surface roughness, requiring post-processing such as machining or polishing [46].
- Lower dimensional accuracy: The broader electron beam spot size compared to laser systems leads to slightly reduced resolution and dimensional accuracy, which can be a drawback for highly detailed features [38].
- High energy consumption and complex maintenance: The need for vacuum pumps, beam generation systems, and high operational temperatures make EB-PBF energy-intensive and demanding in terms of system maintenance [41]
- Limited material palette: EB-PBF is primarily optimized for titanium alloys and nickel-based superalloys. Other materials like aluminum and copper are challenging due to their high reflectivity or poor electron absorption [47].
- Cost of equipment: The initial capital cost of EB-PBF machines is high, and the requirement for vacuum operation adds complexity and cost to the workflow [48].

In summary, EB-PBF is great at producing complex, high-performance metal components. Its key advantages include rapid build speeds enabled by a powerful electron beam, efficient use of materials with minimal waste, and the ability to fabricate intricate geometries in a vacuum environment, which reduces oxidation and enhances material purity. EB-PBF is particularly well-suited for reactive metals like titanium, making it ideal for aerospace and biomedical applications. However, the technology also presents limitations: parts typically have a rough surface finish that requires post-processing, the range of compatible materials is relatively narrow, and the process involves high operational costs due to the need for vacuum systems and electron beam equipment. Table 2.2 summarizes the key advantages and disadvantages of EB-PBF technology.

Table 2.2: Advantages and disadvantages of EB-PBF technology [49]

Advantages	Limitations
Possibility of working at elevated temperatures	High fatigue
Better protection against contamination	Danger for electrostatic charge of the powder
Low level of residual stresses	Only conductive alloys can be obtained
Absence of shrinkage, no thermal post-	Rough finish that requires polishing (depending on
processing	process conditions)
Freedom of design, because of fewer supports	
Allows stacking parts and obtaining meshes	

2.2.3 Process Parameters

In Electron Beam Powder Bed Fusion (EB-PBF), key process parameters such as beam current, scan speed, hatch distance, layer thickness, focus offset, and preheat temperature critically influence part quality, microstructure, and build reliability. The most important process parameters in EB-PBF are the following:

- Beam current (mA): This controls the power of the electron beam and thus the energy delivered to the powder bed. Higher beam currents increase melt pool depth and width, improving densification but also increasing the risk of vaporization and distortion if excessive [50].
- Scan speed (mm/s): The velocity at which the electron beam moves affect the interaction time and heat input. Slower speeds allow for deeper melting but may cause overheating, while faster speeds reduce thermal penetration and can lead to lack-of-fusion porosity [38].
- Hatch distance (mm): This is the spacing between adjacent scan lines in the same layer. A smaller hatch distance ensures better overlap and melt pool continuity, improving density but increasing build time. Larger distances risk defects such as unmolten regions and porosity [51].
- Layer thickness (mm): Thinner layers allow for finer resolution and surface finish but increase build time. Thicker layers speed up the process but can compromise interlayer bonding and lead to stair-stepping effects on inclined surfaces [52].
- Focus offset: The focal length of the beam alters the beam diameter at the surface. A tighter focus yields higher energy density for precise features, while a defocused beam covers wider areas, which can be beneficial for larger melt pools [53].
- Preheat temperature (°C): EB-PBF systems preheat the powder bed to minimize thermal gradients and mitigate residual stresses. Higher preheat temperatures reduce warping and improve part integrity but must be carefully managed to avoid powder sintering beyond intended zones [54].

These parameters are just some of the most influential parameters identified for EB-PBF. However, EB-PBF process, and PBF technologies in general, have a lot of parameters that affect the overall quality and properties of the final built part. Often, these parameters are refined and optimized through simulation and in-situ process monitoring to minimize defects and improve repeatability of the process. It is worth noting that the optimal process parameters differ between materials and they need to be optimized specifically for the material being processed [55]. Figure 2.8 shows a schematic of some of the most influential process parameters in LB-PBF, which is also valid for EB-PBF.

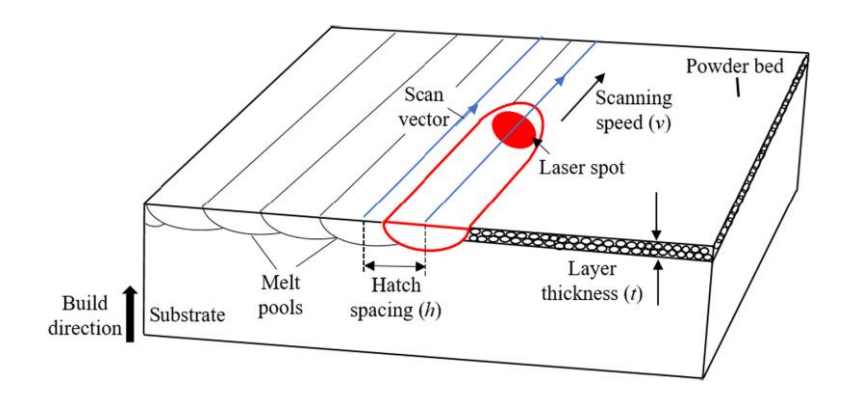


Figure 2.8: Illustration of process parameters in LB-PBF process (applicable for EB-PBF) [56]

2.3 Metallurgy of Ti-6Al-4V

Nowadays, Titanium alloys are direct competitors of stainless and specialty steels, nickel-based alloys and composites. They have high strength, which makes them suitable for aerospace applications, but also good corrosion resistance, due to its protective oxide film, making it good for seawater, marine and industrial chemical applications. The most commonly used titanium alloy is Ti-6Al-4V, which has a chemical composition of 6% Aluminum, 4% Vanadium, 0.25% (maximum) Iron, 0.2% (maximum) Oxygen, and the remainder Titanium. Ti-6Al-4V is an α + β titanium alloy, meaning it contains both the hexagonal close-packed (HCP) alpha (α) phase and the body-centered cubic (BCC) beta (β) phase. At room temperature, this alloy is composed of 91% of α -phase and 9% of β -phase. Aluminum acts as an α -phase stabilizer, while vanadium is a β -phase stabilizer. This dual-phase nature enables the alloy to achieve a grate balance between strength, ductility, corrosion resistance, and fatigue performance [57]. Figure 2.9 shows the phase diagram of the alloy Ti-6Al-4V.

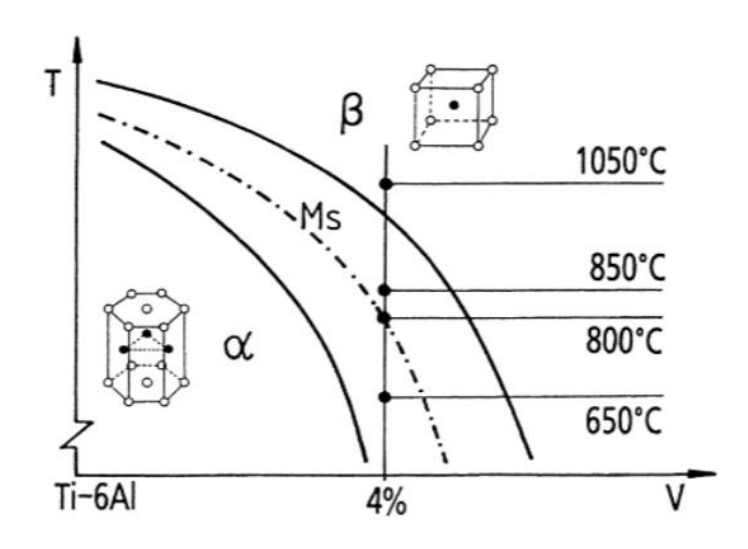


Figure 2.9: Ti-6Al-4V phase diagram [57]

2.3.1 Microstructure Formation

The typical as-built microstructure of Ti–6Al–4V processed by Electron Beam Powder Bed Fusion consists of elongated columnar prior β grains aligned along the build direction, outlined by wavy grain boundary α . Within these grains, a transformed $\alpha + \beta$ structure develops, exhibiting both cellular colony and basket-weave (Widmanstätten) morphologies. Isolated α bulges also appear within the prior β grains. The β phase forms as flat rods embedded in a continuous α matrix. α' martensite is absent, as it decomposes into stable α and β phases during the built. This architecture forms due to the elevated baseplate temperature (~700–800 °C) and multiple reheating cycles, leading to near-equilibrium solidification and preventing martensitic transformation [58]. Figure 2.10 illustrates a schematic of the microstructure of Ti-6Al-4V built in EB-PBF.

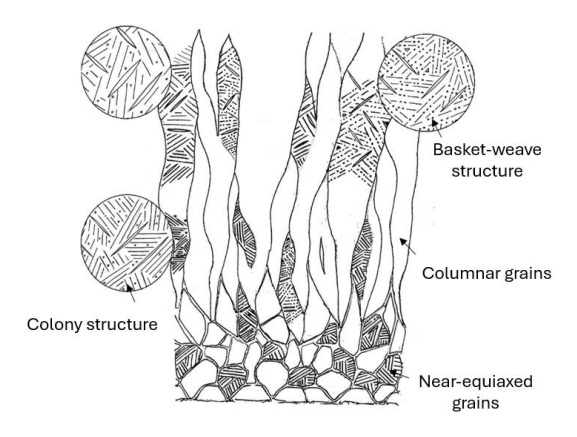


Figure 2.10: Schematic microstructure of EB-PBF-built Ti-6Al-4V (X-Z plane) [59]

Figure 2.11 shows an example of an optical micrograph of a typical bulk EB-PBF. In contrast to certain additive layer manufacturing (ALM) techniques, the individual layers are not easily distinguishable in this case. However, it is evident that the prior β grains grow epitaxially and span multiple layers. Their columnar morphology is a direct result of the vertical thermal gradient present during the process. As the electron beam supplies heat from above, the base plate and previously deposited material function as a heat sink, directing solidification along the build direction (Z-axis) [60].

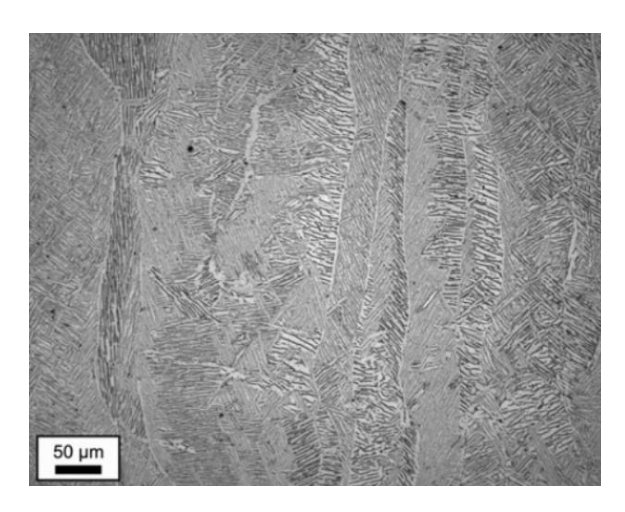


Figure 2.11: Optical micrograph of typical bulk EB-PBF Ti-6Al-4V microstructure [60]

2.3.2 Thermal Gradients and Solidification

In EB-PBF, the preheating of the powder bed (typically 600–800 °C) and the vacuum environment create lower cooling rates and higher thermal gradients compared to laser-based systems. These thermal gradients govern melt pool dynamics, grain morphology, and residual stress profiles.

Al-Bermani et al. [60] developed a solidification map shown in Figure 2.12. This map was constructed using equations and criteria from Kobryn and Semiatin, which predicts the transition between different grain morphologies (columnar, mixed, and equiaxed) during the solidification of Ti-6Al-4V in Electron Beam Powder Bed Fusion (EB-PBF). Initially, the high thermal gradient (G) and relatively low solidification velocity (R) favor fully columnar grain growth. As the melt pool size decreases during solidification, the thermal gradient reduces and the solidification velocity increases, theoretically shifting conditions toward a mixed grain regime on the solidification map. However, experimental observations show no such transition: the microstructure remains fully columnar. This is attributed to the rapid solidification process in EB-PBF, where once columnar grains form, they dominate growth and suppress the nucleation of equiaxed grains. Thus, both theoretical modelling and experimental evidence confirm that standard EB-PBF conditions promote sustained columnar growth throughout the build.

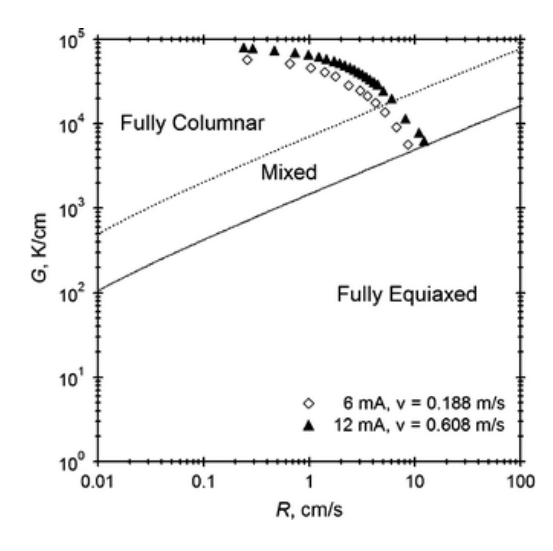


Figure 2.12: Solidification map for EB-PBF using 6 and 12 mA beam currents [60]

The solidification mode in EB-PBF is predominantly directional solidification, with epitaxial growth of columnar β grains. Due to slow cooling rates, diffusional transformations $(\beta \to \alpha)$ dominate, and martensitic α' is typically absent, because initial cooling rates during EB-PBF have been calculated to be in the range $\sim 10^3$ to 10^5 K s⁻¹, well more than that required to form martensite in Ti-6Al-4V. Also, heat extraction mechanisms in EB-PBF occur through both conduction (to the substrate) and radiation (to the chamber), which contribute to the thermal gradients that drive columnar grain formation and the observed microstructural anisotropy [61]. Finally, graded microstructures appear along the build height due to cyclic reheating and evolving thermal histories, causing coarse lamellar α phase near the build plate, while finer features develop near the top of the build [59]. All these characteristics affect the overall microstructure of the material, which by consequence affects its mechanical properties.

2.3.3 Mechanical Properties of Ti-6Al-4V

EB-PBF Ti-6Al-4V typically exhibits high tensile strength, excellent fatigue performance, and anisotropic mechanical behavior due to the layer-by-layer build process. EB-PBF-fabricated Ti6Al4V parts show an ultimate tensile strength (UTS) of approximately ~928 MPa and yield strength (YS) of ~869 MPa, values slightly lower than LB-PBF counterparts. However, EB-PBF parts offer a greater ductility (elongation ~10%) [62]. Figure 2.13 shows the Stress-Strain plots of Ti6Al4V samples (a) EB-PBF specimen built in vertical orientation and (b) LB-PBF specimen built in vertical orientation.

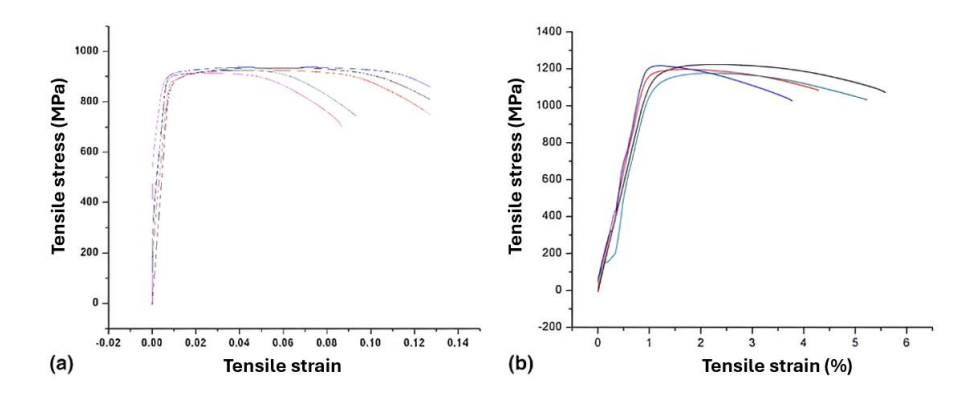


Figure 2.13: Stress-Strain plots of Ti-6Al-4V samples [62]

Directional dependence in mechanical behavior is a notable feature of EB-PBF; the build direction significantly affects both static and fatigue properties. Vertical specimens (built along the Z-axis) usually show slightly lower ductility and fatigue life due to layer bonding orientation, though yield strength remains nearly constant across orientations. Best results are obtained if the sample is oriented at a 45° angle in both EB-PBF and LB-PBF technologies [63]. The fatigue performance of Ti-6Al-4V fabricated via LB-PBF EB-PBF is generally inferior to that of conventionally processed counterparts, with fatigue limits falling below those of cast (~450 MPa) and annealed (~500 MPa) alloys. Among the two, EB-PBF specimens typically exhibit slightly higher fatigue resistance. However, following Hot Isostatic Pressing (HIP), which effectively eliminates internal pores in both LB-PBF and EB-PBF materials, a substantial enhancement in fatigue strength is observed, often exceeding 550 MPa [64]. Figure 2.14 shows the S-N curves illustrating the fatigue behavior of as-fabricated and HIPed Ti-6Al-4V samples.

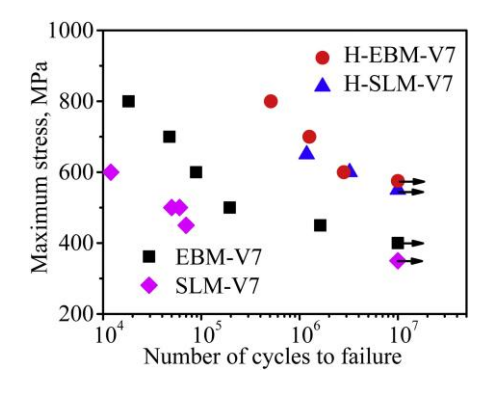


Figure 2.14: S–N curves of as-fabricated and HIPed Ti–6Al–4V samples [64]

2.4 Support structures

In the context of Additive Manufacturing, support structures serve multiple purposes depending on the technology. In Metal Additive Manufacturing, especially in PBF technologies, support structures serve as a key factor for geometrical stability. They help to fix the part on the build plate, carry the weight of the structure, act as thermal sinks or heat dissipators from the part to the plate, thus preventing distortion [65]. Figure 2.15 shows the typical types of support structures applied in Powder Bed Fusion (PBF) technologies.

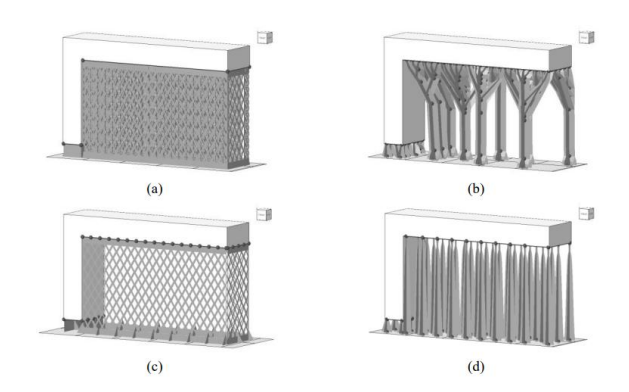


Figure 2.15: Types of support structures in PBF: (a) Block-Support, (b) Tree-like-Support, (c) Polyline-Support and (d) Bar-Support [66]

2.4.1 Defects formation

In overhanging regions (down-skin surfaces without support structures), the initial layers are deposited directly onto unconsolidated powder rather than onto solid substrate or presintered support structures. This loose powder base has inherently low mechanical stiffness and limited thermal conductivity, which impairs its ability to conduct heat away from the melt pool or provide mechanical support during solidification [67]. In areas with poor heat dissipation, pronounced thermal gradients develop, which leads to the formation of residual thermal stresses within the overhanging layers. These stresses frequently result in shape distortions like warping and curling, as the molten material solidifies irregularly and contracts unevenly due to non-uniform temperature distribution. Furthermore, the lack of support beneath these regions allows gravity to induce sagging or downward deflection, particularly in larger or extended overhang structures [68]. Figure 2.16 illustrates the warping process in overhang regions.

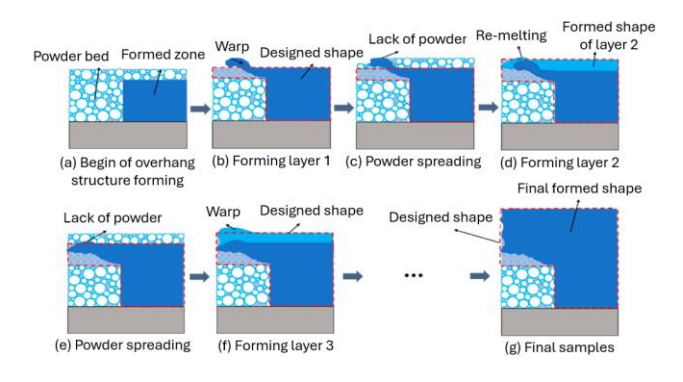


Figure 2.16: Overhang warping process [69]

Additionally, in unsupported overhang regions, surface quality often suffers due to melt pool instability and incomplete powder fusion. These issues lead to noticeable defects, such as rough surfaces, dross buildup, and stair-step patterns, caused by inadequate layer bonding and poor powder compaction beneath the melt path [70]. Furthermore, uneven thermal distribution contributes to various forms of porosity, including lack-of-fusion gaps, keyhole-type voids, and trapped gas pockets, all of which can degrade the part's mechanical strength and overall density [71]. Finally, these combined phenomena result in dimensional inaccuracies, such as deviations from intended geometry or misalignment of subsequent layers. As overhangs cool at inconsistent rates and with minimal constraint, shrinkage-induced distortion accumulates over multiple layers [72]. Figure 2.17 illustrates some common geometrical defects in overhang regions produced by EB-PBF.

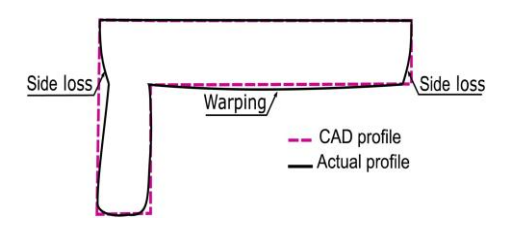


Figure 2.17: Geometrical defects of overhang part [73]

2.4.2 Role of support structures

Due to the reasons mentioned earlier, it is understood the importance of using support structures. Their primary function is to provide mechanical stability during the layer-bylayer build process, especially for overhangs, bridges, and inclined features that would otherwise collapse or deform without a stable foundation. These structures prevent warping, delamination, and collapse by anchoring the part to the build plate and absorbing mechanical stresses induced by thermal gradients and shrinkage during solidification [74]. An essential function of support structures is managing thermal behavior. They improve heat transfer from thermally isolated regions, aiding in consistent cooling and reducing the buildup of residual stresses. This function is particularly crucial in high-energy additive manufacturing processes like LB-PBF and EB-PBF, where high thermal gradients are common. Inadequate thermal regulation can result in defects such as warping, keyhole-type porosity, or even structural failure [75]. Supports also influence dimensional accuracy and surface quality. Unsupported overhangs often experience poor surface finish due to the lack of a thermal sink. Supports help to maintain the intended geometry by stabilizing thin or isolated features and minimizing distortion during and after fabrication [76]. Figure 2.18 shows an example of how some defects like warping and side-loss are reduced or eliminated by using support structures.

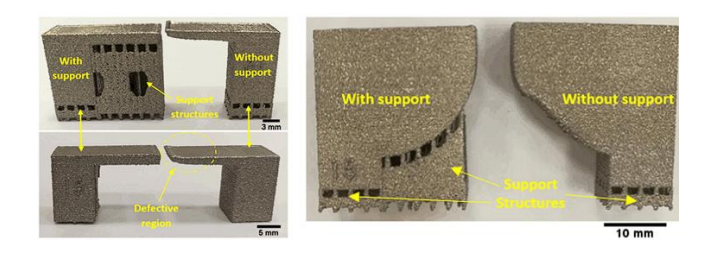


Figure 2.18: Comparison of defects with and without supports in EB-PBF [77]

2.4.3 Problematic with supports structures

The importance of support structures for printing in PBF technologies has already been stated. However, using the use of support structures brings a lot of drawbacks and problems. One of the primary issues is material waste. Support structures are not part of the final component and are discarded after fabrication, consuming additional powder that could otherwise be used for functional parts. This results in increased material costs and inefficient powder utilization, the larger and denser the support, the more powder is needed, directly contributing to waste [78]. Additionally, supports increase processing time, both during and after the build. During the build, the machine must scan and fuse additional layers that make up the supports, lengthening the overall production time. Post-processing is also time-consuming, as supports must be carefully removed, often performed manually by the operator. This labor-intensive step can substantially increase the total production time [79]. Not to mention that in this step, the removal of the support could irreversibly damage the part. Figure 2.19 provides an example of a support structure failure, which damaged the part.

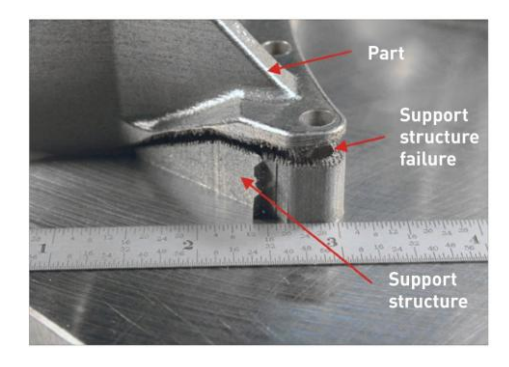


Figure 2.19: Support structure failure [80]

Surface defects and undesired marks are another major concern. The contact regions between the supports and the part typically exhibit degraded surface finish due to fusion inconsistencies and localized overheating. These regions often show rough textures, poor dimensional fidelity, and residual metal that must be machined or polished away by the operator [81]. Figure 2.20 shows an example of a removal of supports leaving undesired marks and rough surfaces.

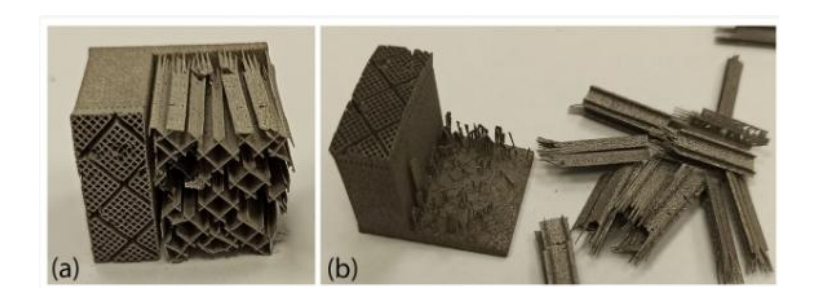


Figure 2.20: Undesired marks due to supports removal [82]

In summary, while support structures are indispensable in PBF technologies, their use comes at the cost of increased material consumption, extended production cycles, and compromised surface quality. This makes the research into alternatives to reduce or eliminate supports highly desirable.

2.4.4 Alternatives to supports structures

Multiple approaches have been studied to eliminate or reduce the use of conventional support structures in PBF technologies. One of these approaches is the use of "no-contact supports". No contact supports refer to support structures that do not touch the part's surface directly. Instead, they are positioned very close to the part, with a small intentional gap between the support and the part. Cooper et al [83] studied this approach and found out that the use of these "no-contact supports" were successful at reducing overhang geometrical distortions like warping in EB-PBF, minimizing in this way the post-processing time required. However, the use of "no-contact supports" brings an additional waste of material, as these supports are also made of solid material.

Another approach is the use of different fusion strategies. A fusion strategy defines how the electron beam moves and melts the powder layer. By adjusting the strategy, it's possible to directly address the root cause of support structures, excessive localized heat and stress. thereby reducing the need for supports. For example, one approach to mitigate distortion is to shorten the scan vectors or break up continuous hatch lines into smaller segments (islands). Studies have found that long scan tracks accumulate higher residual stresses, which translate into greater distortion [84]. By contrast, using short hatch lengths or island (chessboard) patterns can relieve stress buildup. For example, in LB-PBF, Mugwagwa et al [85] compared four scan patterns on tool steel and reported that a successive chessboard strategy (small 5×5 mm islands scanned in sequence) produced the lowest residual stresses with up to 40% lower than a conventional long-stripe island strategy. Beyond geometric hatching changes, researchers have also explored time-based scanning modifications such as pulsed or paused power exposure to mitigate overheating in overhang regions. Gao et al [86] used a "paused-based" scanning strategy which consists of inserting brief delays during hatch scans to allow heat to dissipate. They found that this method significantly reduced overhang displacement by avoiding local heat accumulation. In the other hand, in EB-PBF, GE Additive's ARCAM introduced a "Point Melt" technology in its EBMControl 6.4 software, which melts the powder through a series of small points (pulses) instead of continuous lines. GE reported that Point Melt produces parts with excellent isotropy and surface roughness comparable to laser-based PBF, and this strategy critically reduces the amount of support needed for overhangs [87]. In other studies, it has been shown that discrete point scanning strategies could reduce thermal gradients and residual stresses, thereby improving part stability and enabling larger overhangs without supports [88], [89].

Finally, another approach to reduce supports usage in PBF is optimizing process parameters, therefore, the energy density applied. By adjusting beam settings, researchers have shown it's possible to print overhangs at certain angles without defects like dross or distortion. This is possible because the beam parameters control the energy input delivered on overhangs. Therefore, optimizing it improves surface finish and also mitigates distortion by limiting overheating in those layers [90], [91].

In summary, literature reveals that traditional PBF scan strategies (continuous raster scans) often produce high thermal gradients and residual stresses. While discrete point and island scanning patterns significantly influence thermal gradients in the PBF processes due to smaller scan vector lengths. However, majority of research on this matter has been done with LB-PBF technology. Further research into alternative solutions for supports in EB-PBF is needed.

3 Research methodology

In this section, the research methodology used in this study is described. It describes the machine, tools, and materials employed. At the same time, it details the process and experimental plan developed to evaluate the influence of different fusion strategies in the production of parts without the usage of support structures and how their impact is measured.

3.1 Materials

3.1.1 ARCAM A1 EB-PBF machine

The EB-PBF machine used for all the experiments is an ARCAM A1 from GE Additive (ARCAM AB/Colibrium Additive). This machine was originally released in late 2009, which was adapted to produce orthopedic implants. The ARCAM A1 machine is widely used in scientific research in multiple fields like Mechanical Engineering, Biomedical Engineering, Computer Science, Energy and Materials Science. Figure 3.1 shows the ARCAM A1 EB-PBF machine used for this study.



Figure 3.1: ARCAM A1 machine [92]

This machine uses a constant accelerating voltage of 60 kV, with the capability of varying the beam current, which allows to control the power in a range from 50-3000 W. During the build, the temperature is kept at around 700 °C. In the other hand, this machine is able to deflect the electron beam with a speed of up to 8000 mm/s across the powder bed. The maximum build size is of $200 \times 200 \times 180$ mm and the beam spot size varies between 0.2 mm to 1.0 mm. Finally, the chamber pressure is maintained at around 10^{-4} mbar to prevent oxidation of powder and beam scattering. Table 3.1 summarizes the characteristics of the ARCAM A1 machine used in this study.

Table 3.1: Characteristics of ARCAM A1 machine [93]

Power	50 – 3000 W
Build temperature	~ 700 °C
Deflection rate	Up to 8000 mm/s
Maximum build size	200x200x180 mm
Beam spot size	0.2 mm - 1.0 mm
Chamber pressure	10 ⁻⁴ mbar

Figure 3.2 shows a picture from the inside of the machine, where the build chamber is located. In this picture, the major components of an EB-PBF machine can be observed: Powder hoppers, building tank, powder bed, powder reservoirs and the heat shield which protects sensitive parts of the machine from radiant heat and metal vapor generated during melting.

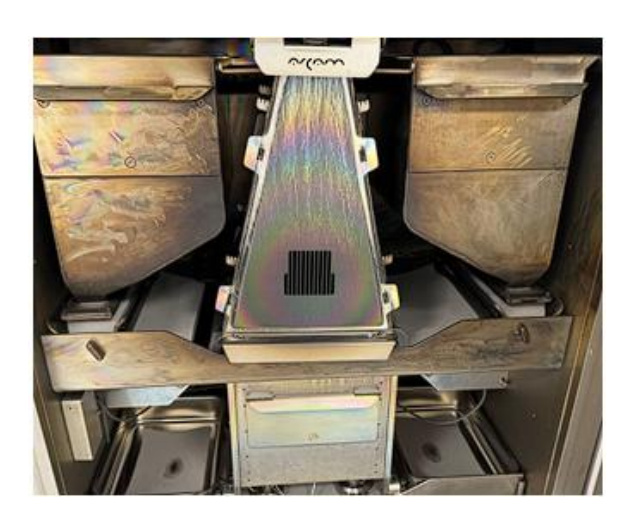


Figure 3.2: ARCAM A1 chamber

3.1.2 ARCAM Ti6Al4V Grade 5 powder

The material used for the experiments is ARCAM Ti6Al4V Grade 5 provided by the machine manufacturer, which is the most common material used in EB-PBF technology. This alloy contains good mechanical properties, corrosion resistance, good behavior at high temperatures and is heat treatable. ARCAM Ti6Al4V powder has a powder particle size distribution ranging from 45 to 100 μ m [45]. Ti6Al4V alloy contains around 5.5% to 6.5% of Aluminum as α -stabilizer and around 3.5% to 5.5% of Vanadium as β -stabilizer. Table 3.2 shows the chemical composition of ARCAM Ti6Al4V powder.

Table 3.2: Chemical composition of ARCAM Ti6Al4V powder [94]

Powder	Aluminum	Vanadium	Iron	Oxygen	Nitrogen	Carbon	Hydrogen	Titanium
	(Al)	(V)	(Fe)	(O)	(N)	(C)	(H)	(Ti)
ARCAM Ti6Al4V Grade 5	5.5 – 6.5%	3.5 – 4.5%	<0.30%	<0.20%	<0.05%	<0.08%	<0.015%	Balance

Ti6Al4V Grade 5 exhibits a strong combination of mechanical properties suitable for high-performance applications. It shows a high yield strength of 950 MPa and an ultimate tensile strength of 1020 MPa, indicating excellent load-bearing capacity. With an elongation at break of 14%, the alloy maintains good ductility, allowing it to deform plastically before failure. Its fatigue strength exceeds 10 million cycles at 600 MPa, demonstrating exceptional durability under cyclic loading. Additionally, the alloy has a modulus of elasticity of 120 GPa, reflecting a high stiffness, and a Rockwell hardness of 33 HRC, providing moderate wear resistance [95]. Table 3.3 shows a summary of the mechanical properties of ARCAM Ti6Al4V powder.

Table 3.3: Mechanical properties of ARCAM Ti6Al4V powder [95]

Mechanical properties	ARCAM Ti6Al4V Grade 5				
Ultimate Tensile Strength (UTS)	1020 MPa				
Yield Strength, R _{p0.2}	950 MPa				
Fatigue Strength @ 600 MPa	>10,000,000 cycles				
Elongation at break	14%				
Reduction of area	40%				
Modulus of Elasticity	120 GPa				
Rockwell Hardness	33 HRC				

3.1.3 Powder Recovery System (PRS)

In ARCAM EB-PBF systems, an auxiliary system called Powder Recovery System (PRS) is used to safely and efficiently reuse the unmelted powder left after each build. In the PRS, compressed air and loose titanium powder is used to free the encapsulated printed parts from the sintered powder block and loosen the remaining powder [96]. This system minimizes the consumption of raw material in the process. When a build is over, the loose powder is recovered with a vacuum cleaner. Then, the build plate with all the sintered powder is put in the PRS system, where the projection of air charged with particles dissolves the bed of semi-sintered powder that surrounds the part. Afterwards, all the powder is recovered from the PRS and the vacuum, then it is inserted into the sieving cabinet, where a mesh filters the powder to remove large particles and to break down lumps and agglomerates. Finally, the sieved powder is returned to the machine for the next build cycle. This cycle ensures that the powder is correctly recycled and that the exposure time of the powder to air and humidity of the environment, is the minimum possible. Figure 3.3 shows a picture of the ARCAM PRS used for this study. In the other hand, Figure 3.4 shows the vacuum cleaner and Figure 3.5 shows the sieving cabinet.



Figure 3.3: ARCAM Powder Recovery System (PRS)



Figure 3.4: Vacuum cleaner for Ti6Al4V powder



Figure 3.5: Sieving cabinet for Ti6Al4V powder

3.1.4 Geometry of the part

The geometry of the part was selected with the objective of evaluating the influence of the different fusion strategies in the building of the overhang zone without support structures. A large overhang zone without any support structures is ideal to observe the typical defects that occur in unsupported parts. This type of geometry is also commonly used in literature to study overhang zone fabrication in PBF technologies. Figure 3.6 shows the dimensions of the geometry selected, while Figure 3.7 shows the isometric view of the part.

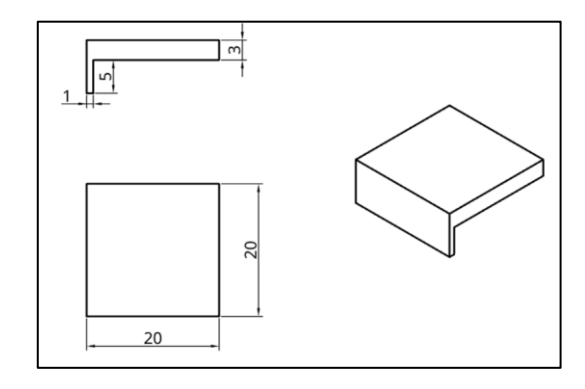


Figure 3.6: Geometry of the part for experiments (dimensions in mm)

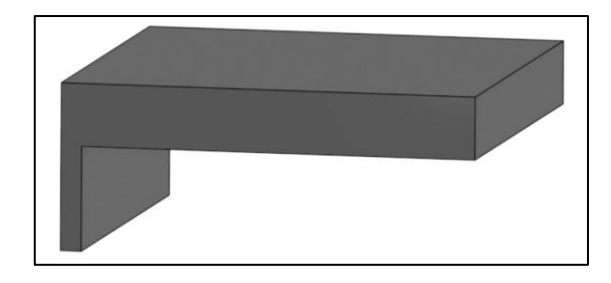


Figure 3.7: Isometric view of part

For identification of each part, identification marks were added at the "foot" of the part. The reason for this is because during the depowdering step in the PRS, parts can easily be thrown away and therefore be confused. Due to this, for each batch, each part has a unique set of identification marks (cuboids), which makes it easy to be identified. Figure 3.8 shows an example of how the identification marks are added in the part.



Figure 3.8: Example of identification marks (cuboids)

3.2 Process chain for ARCAM A1 machine

3.2.1 Preparation of digital file

The first step of the process chain consists of preparing the digital file that is inserted into the ARCAM A1 machine. Initially, the model is designed in a 3D CAD software. In this case, Onshape software is used. The model is then exported in STL format for slicing by layers. Figure 3.9 shows an image of the design process in CAD software.

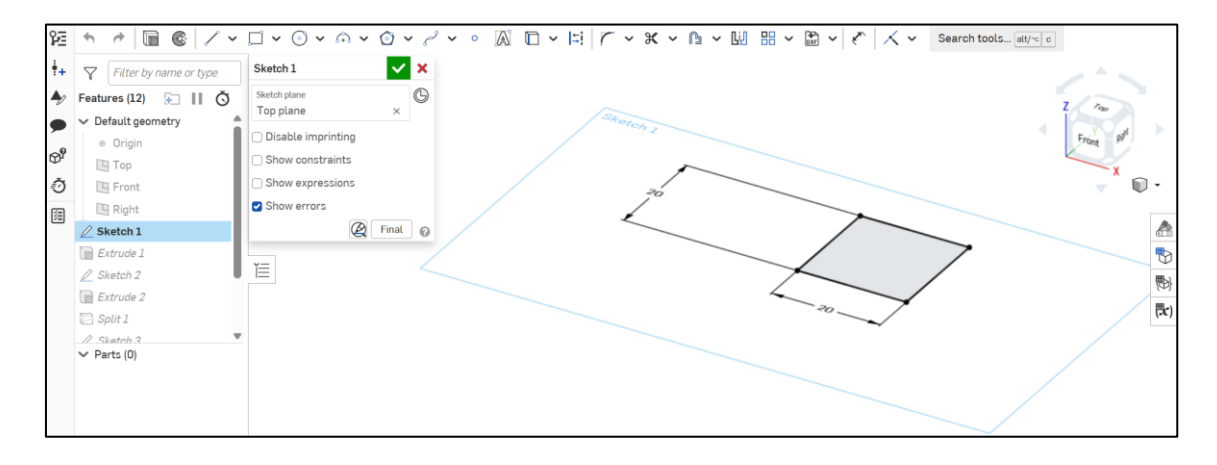


Figure 3.9: CAD in Onshape software

For the slicing of the model, several options were employed. The first one consists of using Rhinoceros 3D software to position the parts in the build and Grasshopper visual programming add-on is used for slicing and generation of the file in the required format for input into the machine. Figure 3.10 shows an image of the Rhinoceros 3D software with a set of parts positioned within the machine build limit.

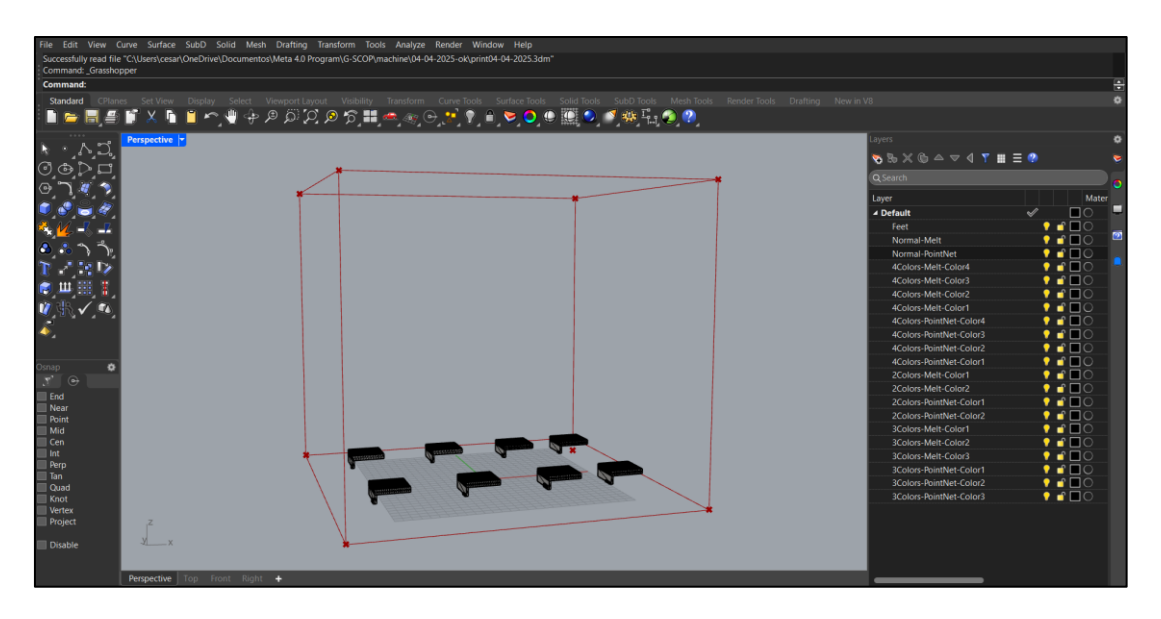


Figure 3.10: Part positioning in Rhinoceros 3D

In Grasshopper, all the meshes from each part are selected and they're put into some programming blocks developed specifically for this process. The first block is EB-PBF Slicer, in here the mesh of the part is inserted into the Part (p) input, the Model type (t) is set to "material" representing a solid part and in Model name (n) the name of the part is entered. The resulting file from this block is a Common Layer File (.CLF), this is then input into the next block, the EB-PBF Build Assembler, where in Build name (b) the name of the file is selected, finally in output folder (f), the desired path for the generation of the file is selected. After executing these blocks, the resulting file is an ARCAM Build File (.ABF) which is directly inserted into the machine. An important remark is that the EB-PBF Build Assembler inputs are expandable, so this means that multiple EB-PBF Slicer blocks can be connected to slice multiple parts present at the build and generate a unique ABF file with all the parts. Figure 3.11 shows an image of the programming blocks used in Grasshopper.

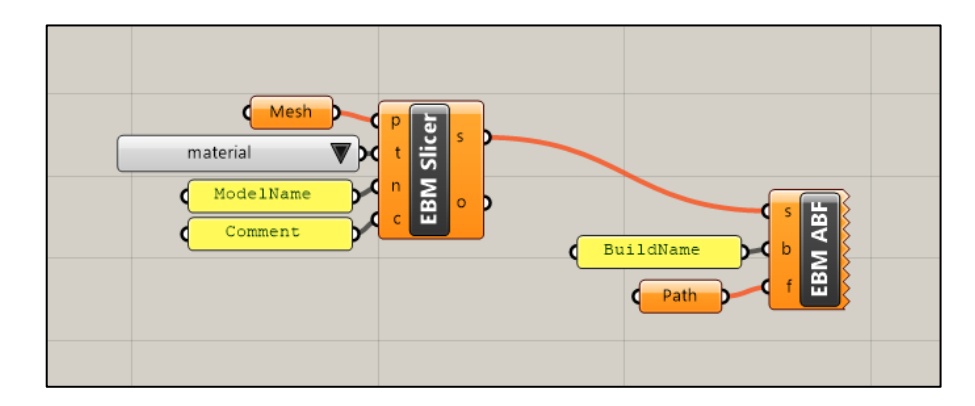


Figure 3.11: Part slicing in Grasshopper

The second way to slice the parts is to use directly the software from the machine manufacturer: ARCAM Build Assembler. In here, the already positioned STL parts are directly imported into the software. Again, the parts are imported as a "Part" representing a solid model. Parameters like "layer thickness" and "build plate size" are set constant to 50 µm and 210x210x10 mm respectively. At the end, a file in ABF format is obtained with all the sliced parts, which is then inserted into the machine. Figure 3.12 shows a picture of ARCAM Build Assembler software.

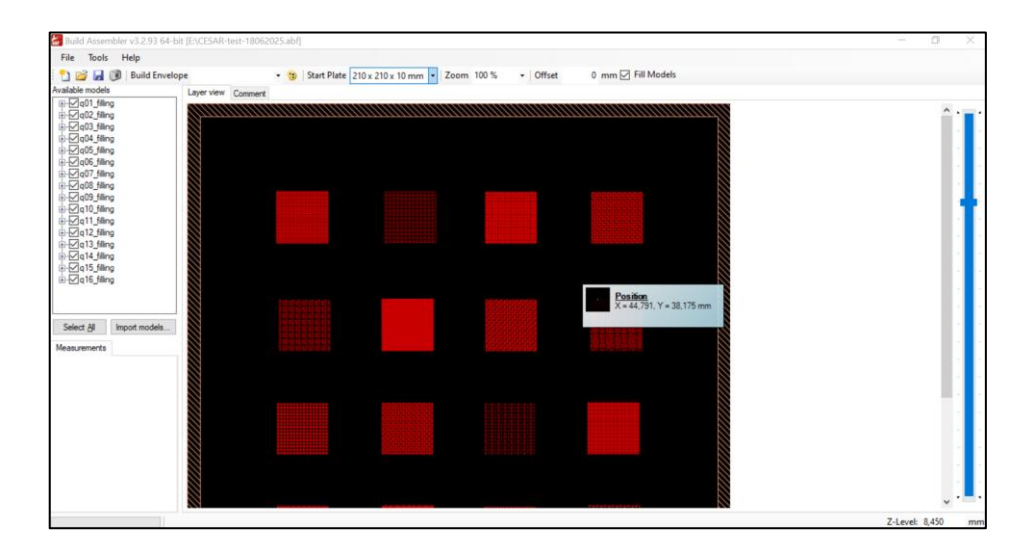


Figure 3.12: ARCAM Build Assembler software

The third way to slice the parts is to use Autodesk Netfabb. This method was used for the first time in this study, due to its ability to convert between open-source formats and ARCAM proprietary formats, this detail is explained in further detail later in this work. Netfabb also allows to position and arrange freely the parts in the build, as Rhinoceros 3D. However, it was decided to not use it for this purpose and only for slicing of the parts and exporting in the required format. For this, the already positioned STL parts are imported into Netfabb, and the "Slice parts" operation is performed. In here, the "layer size" is selected to $50~\mu m$ as well. At the end, an ABF file can be exported, which is then imported into the machine. Figure 3.13~shows an image of the slicing process in Netfabb software.

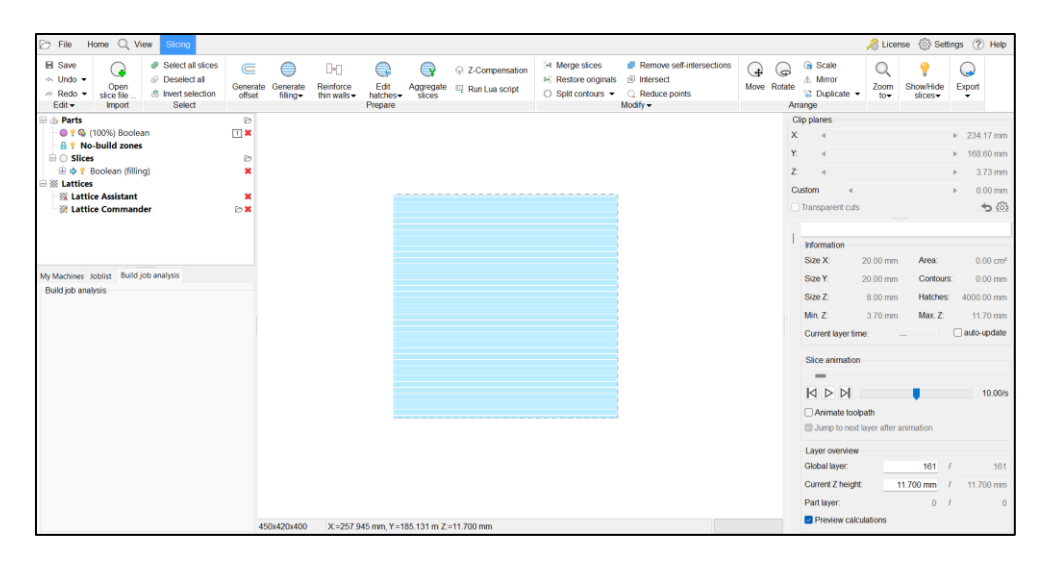


Figure 3.13: Slicing in Autodesk Netfabb software

Regardless of the method used for slicing, the output file is an ABF file containing all the sliced parts in the build. This ABF file is imported in the machine and further parameter configurations are performed. This means that the ABF files don't contain information on the process parameters, these are later configured individually in the machine. Figure 3.14 shows the workflow for the generation of the digital file.

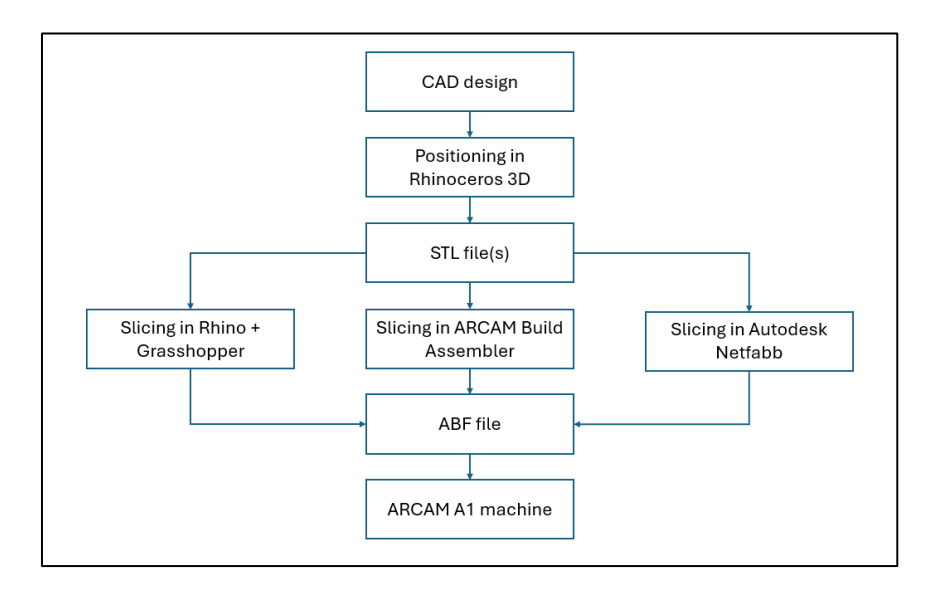


Figure 3.14: Workflow for digital file generation

3.2.2 Machine set-up

After the generation of the digital file, a USB flash drive is used to transfer the ABF file from the computer to the machine. In the machine, EBMControl 5.0 (also 3.2 as explained later) software is used for the machine set-up and operation. In EBMControl, the machine set-up is divided into multiple windows. The first one is "Build" window. In here, the build file is selected (ABF file), as well as other important information like the start plate (210 Plate) and the Start and Stop Z-level (typically 0.05 mm to the maximum height of the parts). Figure 3.15 shows a picture of the "Build" window in EBMControl.



Figure 3.15: "Build" window in EBMControl

The next step is the "Process" window. In here, all the models are selected as well as their process parameters. The first option is "Select Material" which was set to ARCAM Ti6Al4V. Selecting the material gives access to a set of build themes and process parameters directly pre-configured by ARCAM for that specific material. After this, the process steps are configured. In the process steps configuration, for each step, three sections are observed: The step activation (ON/OFF), the build theme (ARCAM theme and parameters) and the model(s). In a typical build, the first step is the pre-heat. For this, the default ARCAM Pre-heat theme is used (no model is selected). Then, in the other steps, the models are selected. For example, a typical set-up includes using a step with all the solid models with the ARCAM Melt theme, and other step with all the supports with the ARCAM Wafer theme. Figure 3.16 shows a picture of the "Process" window in EBMControl.

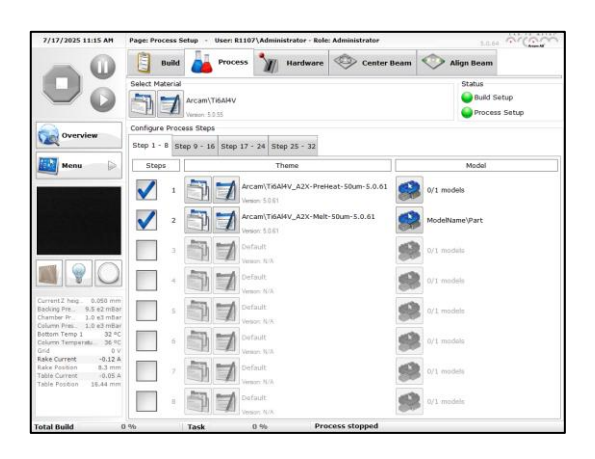


Figure 3.16: "Process" window in EBMControl

The next step is the "Hardware" window. Where the three major components of the machine are configured: rake and table, vacuum and power supply. However, before configuring anything at this window, the physical set-up of the machine must be done. The physical set-up implies cleaning the chamber if it comes from a previous build, re-fill the powder hoppers if needed, and place again the build plate. For cleaning the chamber, two vacuum cleaners are used with the objective of preventing powder contamination. A "dirty powder vacuum" for cleaning everything outside the chamber, and a "clean powder vacuum" for cleaning all the powder inside the chamber. If necessary, the heat shield is also disassembled and cleaned. In the column, there's a protection foil which is also cleaned or replaced is needed. The build plate is also cleaned, and a cross is done with a marker to indicate the center of the plate. Before placing the build plate again, the thermocouple is checked to certify its correct functioning. Figure 3.17 shows a picture of the placing of the build plate.



Figure 3.17: Placing of the build plate

After placing the build plate, the powder hopper outlets are opened with the purpose of letting powder come out into the chamber. The build plate is covered with powder to calibrate the "0" table position. In the "hardware: window in EBMControl, the rake and the table are activated in order to control their movement. With the controls in the software, the table is gradually moved up until finding the position where the rake removes all the powder from the build plate. After finding the "0" position, the table is moved down to -0.4 mm in order to prevent dilatation of the plate due to the electron beam. In parallel, the sensors for detecting powder in right and left positions are checked to verify its correct functioning. Then, the rake is recalibrated if needed, with the objective that the rake displaces the same amount of powder from left to right and from right to left. Figure 3.18 shows a picture of the calibration of the rake.



Figure 3.18: Calibration of the rake

After calibrating the rake, and that the bed is completely and uniformly filled with powder. A small hose connected to the vacuum is used to remove all the powder on top of the build plate with the objective of performing the first preheat in the build plate without melting or sintering any powder at the beginning of the fabrication. Then, the heat shield is placed again in the chamber as shown in Figure 3.19.



Figure 3.19: Placing of the heat shield

When the heat shield is placed, the outer borders of the door are cleaned, and the door is closed. The door is manually pushed, and the vacuum is activated in the "hardware" window. The vacuum causes the pressure to start decreasing gradually. When the chamber pressure reaches a value lower than $5x10^{-4}$ mbar and the column pressure reaches a value lower than $5x10^{-6}$ mbar, the power supply is activated. For activating the power supply in the "hardware" window, first the High Voltage contactor is activated, then the voltage, and finally, when the voltage reaches 60,000 Volts, the filament current is activated. Figure 3.20 shows a picture of the "Hardware" window.

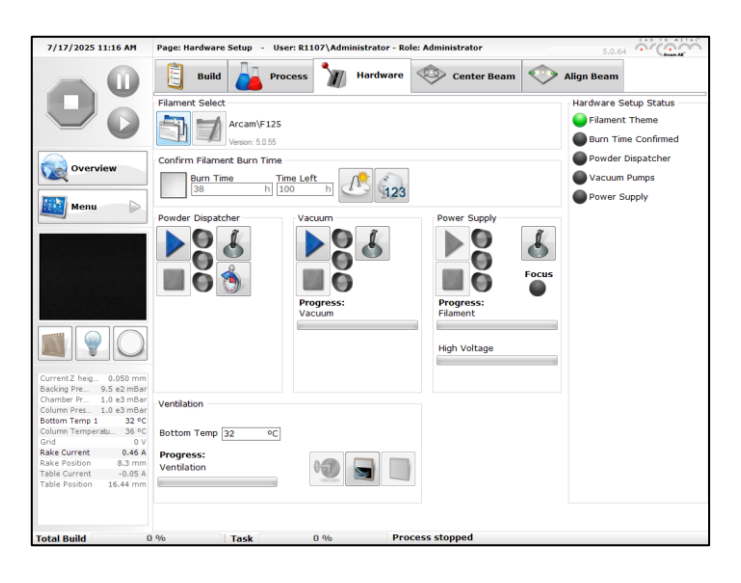


Figure 3.20: "Hardware" window in EBMControl

The next step is the "Center Beam" window. In here, the electron beam is centered in the build plate. For doing that, the electron beam is activated with a small value (~ 0.4 mA) just to be slightly visible. With the controls present in the window the electron beam is displaced along X and Y coordinates. The objective is to align the electron beam with the cross done in the build plate center and save its correct position. Figure 3.21 shows a picture of the "Center Beam" window.

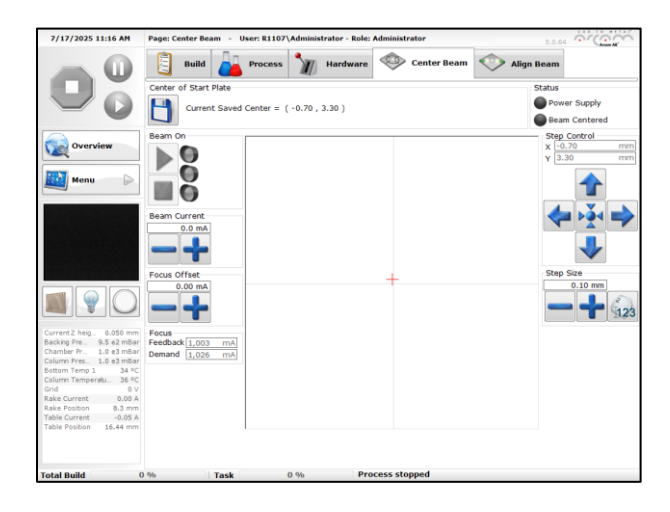


Figure 3.21: "Center Beam" window in EBMControl

Figure 3.22 illustrates the process of beam centering. Originally, the electron beam is displaced some distance from the center, after moving it with the controls in the "Center Beam" the electron beam is aligned with build plate center. Proper centering helps avoid distortion, misalignment, and other defects caused by beam offset during the fabrication.

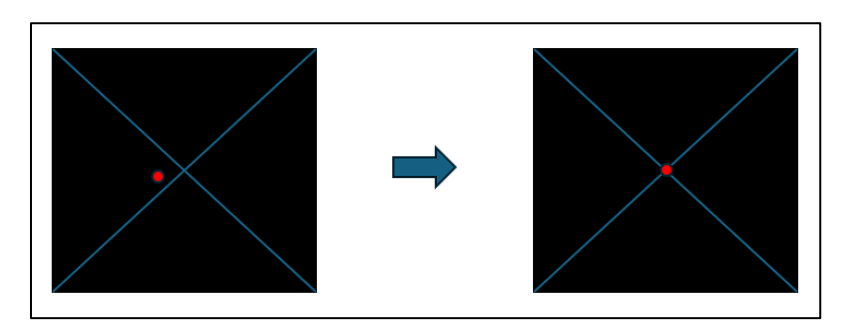


Figure 3.22: Process of beam centering

The next and final step to start the fabrication, is the "Align Beam" window. In here, the deflection system is properly calibrated, so that the beam follows a straight, accurate path across the build area without distortion or deviation. For this, nine beam positions over the build plate are calibrated to ensure an ideal overlap between deflection trajectories of the beam. Each beam position is calibrated one at the time and again, the X and Y coordinates are modified in order to find the spot where there's no flickering of the beam. When the beam is flickering, two moving beam spots are observed, which means that the beam is not correctly aligned. After the proper calibration, only one steady beam spot without flickering must be seen. This process is repeated in the other 8 beam positions across the build plate. Figure 3.23 shows a picture of the "Align Beam" window.

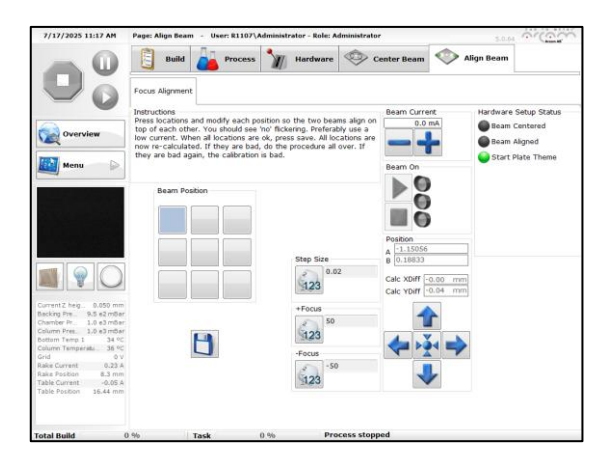


Figure 3.23: "Align Beam" window in EBMControl

Figure 3.24 illustrates the process of beam centering. When correctly aligned, the beam's position is consistent across the entire build plane, preventing focus issues, distortion, and geometric inaccuracy in the printed part.

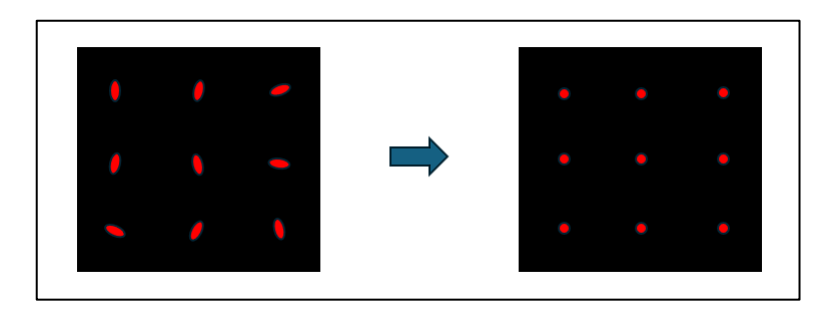


Figure 3.24: Process of beam alignment

After all the steps are successfully completed, the "play" button turns green, allowing the start of the fabrication. When the fabrication is started, a message dialog is displayed asking "Start plate heating", this option is always turn on in a normal production run. Once the button is pressed, the fabrication will start automatically without any necessary human supervision. Figure 3.25 illustrates the workflow for the machine set-up.

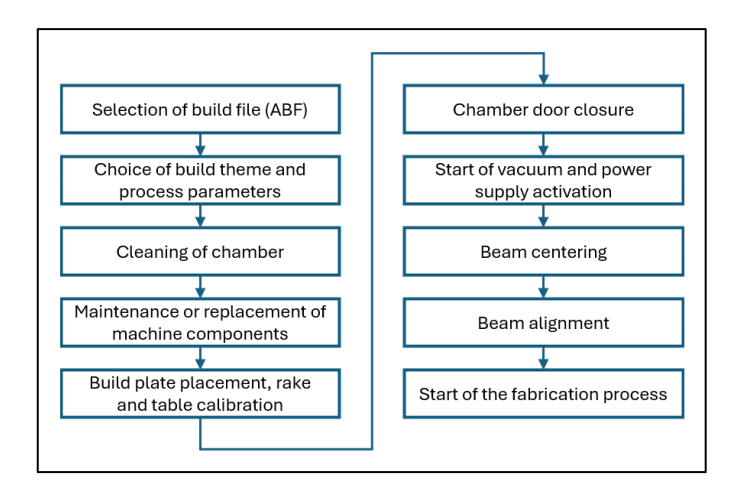


Figure 3.25: Workflow for machine set-up

3.2.3 Manufacturing process

The first step in the manufacturing process, as it was selected before starting, is the initial plate heating. The electron beam rapidly scans all the build plate until it reaches a temperature of around 700 °C for Ti6Al4V in this case, which takes around 40 minutes. The initial plate heating in EB-PBF ensures strong part adhesion, reduces thermal stress and distortion, and stabilizes the powder bed by creating a thermally uniform environment before melting begins. As explained before, this is one of the key differences between EB-PBF technology and LB-PBF technology. Figure 3.26 shows a picture of the initial build plate heating.

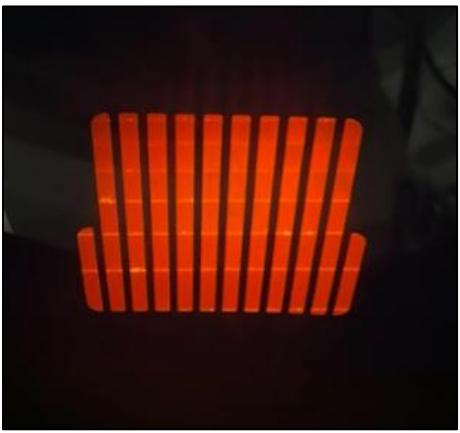


Figure 3.26: Initial build plate heating

After the build plate heating is done, the rake makes two to three movements from one side to another in order to completely spread the powder across the build plate. When the layer is deposited, the preheating of the powder layer starts. The preheating also consists of the rapid scanning of the beam across the plate, with the objective to maintain uniform temperature across the different layers. Depending on the build, sometimes two preheat steps are done, one before the selective melting, and other after the selective melting. The default ARCAM Pre-heat theme is used for all the builds. Figure 3.27 shows a picture of the pre-heating step during the manufacturing process.



Figure 3.27: Pre-heating process

When the preheating step is done, the selective melting of the model is done. Depending on the build theme and parameters selected, the melting is done with a specific scanning speed, hatching strategy and beam current. Figure 3.28 shows a picture of an example of the selective melting of a part in the machine.



Figure 3.28: Selective melting of a part

After the selective melting of all the models in the layer is done, the table is lowered in a distance of 50 µm corresponding to the layer thickness. Then, the rake moves again from side to side to spread the new layer of powder over the build plate, starting again the process. Figure 3.29 shows a picture of the spreading of powder for a new layer.

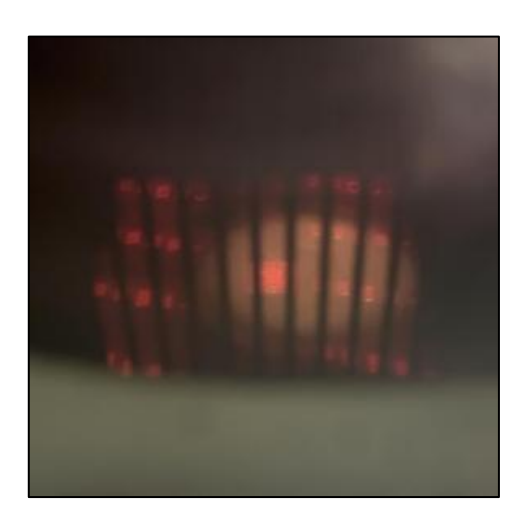


Figure 3.29: Spreading of powder for a new layer

The process of pre-heating, selective melting, table lowering and spreading of the powder is repeated for each layer until the final layer of the build is fabricated. The workflow of the manufacturing process is illustrated in Figure 3.30. The machine automatically resets itself if there's any non-critical alarm or problem, which makes the process completely autonomous. Only if a critical problem surges, the machine will automatically stop, causing the build to fail but protecting the status of the machine components. For the correct functioning of the machine, all the machine set-up steps must be successfully done and regular maintenance on the machine must be performed. This causes the EB-PBF process to require highly skilled operators and a very large learning curve to get the knowledge on how to operate the machine.

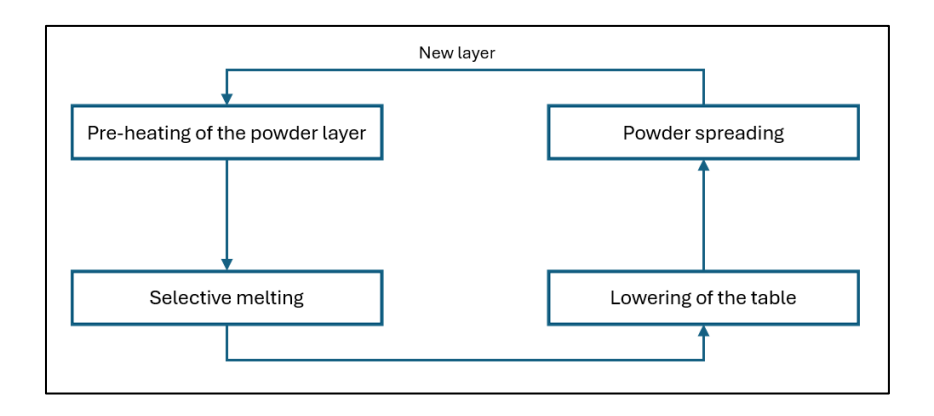


Figure 3.30: Workflow for manufacturing process

3.2.4 Post-processing of parts

Once the last layer is successfully fabricated, the machine automatically stops the process. Helium gas is let into the chamber in order to start decreasing the temperature. Once the temperature reaches 100 °C, the chamber is cooled with air until it reaches ambient temperature. Once the temperature and pressure are in normal values, the machine allows the opening of the door in order to remove the build plate with all the manufactured parts. However, sintered powder particles surround the fully solid parts, and this excess powder is removed using the ARCAM Powder Recovery System (PRS). In the PRS, the parts get completely cleaned up and ready for any other post-processing step required like shot-peening or removal of supports. In this study, no other post-processing techniques are applied; the parts are studied directly as they're built and cleaned up in the PRS. Figure 3.31 shows a picture of a part being depowdered in the ARCAM PRS.



Figure 3.31: Depowdering in ARCAM PRS

Once the parts are completely depowdered and cleaned up, the machine is prepared for the next build. Preparing the machine again means following the machine set-up instructions again and performing any necessary replacement or maintenance of the components in the machine. It is worth noting that every time the machine door is open, or handling of powder is being done, all the necessary security equipment must be used: laboratory gown, face mask, glasses, gloves and security shoes. Even though Ti6Al4V powder particles in EB-PBF are much bigger than in LB-PBF technology, inhalation risks must be prevented.

3.3 Preliminary exploratory work

In order to study the effect of different fusion strategies in parts produced by EB-PBF, the idea of reducing the scanning lengths was decided to be used since it has been proved in other studies to deliver good results in terms of residual stresses due to lower thermal gradients, as stated previously in this work. However, to do this, it was first necessary to do an exploratory work to completely understand how to set a different fusion strategy in an ARCAM A1 machine. The reason for this is that the ARCAM A1 machine is basically a black-box system. Normally, the user sets a set of inputs, and the output is the strategy used to fabricate the part. However, the exact relationship between the inputs and outputs is not exactly known for this machine. Which means that the user does not have precise knowledge of the internal working during the fabrication. The inputs in this machine are basically the ABF file, containing the sliced part, and the build theme with process parameters defined in the process window during the set-up. Depending on the options selected, the output will be a specific fusion strategy and energy density. Figure 3.32 illustrates the concept of the ARCAM A1 machine as a black-box system.



Figure 3.32: ARCAM A1 as a black-box system

The "ARCAM Build themes" are a set of process parameters and functions optimized by the machine manufacturer for the material used [97]. The "Melt" theme is the most used since it is applicable for melting any geometry. The "Net" theme is optimized for thin structures (less than 1 mm diameter struts) as it follows only contour paths. The "Point-net" theme gives process parameters for the fabrication of parts from wireframe geometries. Finally, the "Wafer" theme is made to melt supports [98]. In this machine, no information about the beam trajectory or fusion strategy is included in the current process-chain. The part to be fabricated is sliced and the machine automatically calculates the beam trajectory. Additionally, there is a set of options in the process window that also affects the beam behavior. Therefore, a set of experiments were developed in order to study the effect of each build theme, option and process parameter in the beam trajectory and behavior.

3.3.1 Set-up for preliminary exploratory work (no powder)

To do the preliminary experiments, the same machine set-up described before was used. However, the powder hoppers were left closed and all powder in the chamber was vacuumed. This was done with the objective of watching directly the beam trajectory and behavior in the build plate. The selected geometry was a simple square and a set of squares directly starting in the build plate, as no actual powder was being melted. All the desired parameters to be studied were modified in the "Process window" in EBMControl 5.0, as this is the most recent software version available for this machine and the one that is currently used by all

the users. Figure 3.33 shows a picture of the vacuuming of the powder for the preliminary

experiments.



Figure 3.33: Vacuuming of powder for preliminary experiments

3.3.2 Effect of ARCAM build themes

The square geometry used was sliced like "Part" which means it is a solid part. For these preliminary experiments, no Pre-heating step was used, as no actual powder was being melted. Multiple experiments were conducted to study the effect of each build theme and parameter; the key findings are presented in the following section. Figure 3.34 shows some snapshots of some of the experiments conducted without powder.



Figure 3.34: Snapshots of the experiments without powder

The first studied build theme was the "Melt" one, as this is the normally used for manufacturing any geometry in the machine. The default parameters were used for the experiments, each desired parameter to study was varied once at a time in order to precisely study its influence in the beam behavior. Figure 3.35 shows a picture of the Melt build theme parameters window.



Figure 3.35: Melt Build Theme process parameters

As seen in the figure, the melt theme has a series of folders with different parameters that can be modified. The "power analyze" was left as default. In the "Contours" folder, the inner and outer contours were deactivated, this was done because it was only desired to study the effect in the inner scanning strategy during the melting, so no contours were used for all the experiments. In the hatch folder, there are multiple subfolders, each one containing important information on the fusion strategy and the beam behavior. In the "Beam" subfolder, there is basically the information regarding the energy density and scan speed applied, the so called "Speed function" is an ARCAM function that is used to control the beam current and speed depending on the scan length, thus having a variable value defined automatically by the function.

This speed function works by default in the current set-up, in the so-called "automatic mode", and it's used by the users to change the value of energy density applied into the material. For instance, a higher value of speed function means a higher speed, which translates into a lower energy density (The default value in this software version is SF=70). The objective of the ARCAM speed function is to maintain the thickness of the melting pool constant during the melting process [99]. During the experiments, it was found that it is not possible to specify a fixed value of speed and current with the Melt Theme. A "manual mode" is suggested by other authors working with the same machine, which allow them to set a specific constant value of speed and current. However, this mode could not be activated in this machine. Therefore, the only way to modify the energy density with Melt Theme is by modifying the speed function.

The next subfolder is the "Hatch" one. In this subfolder, basic information regarding the hatching strategy is entered, the line offset, which is the distance between hatching lines and the hatch depth, both were kept by default (0.2 mm and 0.05 mm respectively). The next subfolder is the "Thickness" one, this subfolder contains information on other ARCAM function, the "Thickness function", this function also modifies the scanning speed of the beam, but in the first layers of the part. This is done with the objective of reducing the energy density in the first layers and prevent excessive heat accumulation [100]. This parameter was also left by default (Speed factor = 1.5). Then it follows the "Turning points" subfolder. This contains information on the "Turning points function", which adjusts the speed of the beam

near the edges of a part with the objective to reduce over melting at the corners [101]. This also was left by default (TRUE and pre-exponential factor of 0.9).

The upcoming subfolder is the "Current compensation", with contains information on the ARCAM function by the same name. This function adjusts the melting current based on scan line length, increasing power for longer lines to ensure consistent melting and reduce build time [102]. Again, the default parameters were used (Scan length reference = 45 mm, RefCurrent = 12 mA, MinCurrent = 3.5 mA). The final subfolder is the "Line offset compensation" which also contains the ARCAM function with the same name. This function adjusts the spacing between hatch lines based on scan length to maintain consistent melting and energy distribution [103]. Again, the default parameter (Max Line Offset = 0.2 mm) is used.

In "Melt" theme, the machine does a raster hatching inside the part and makes contours depending on configuration. In this case, no contours were used, and the rotating hatch was deactivated in order to have a consistent order of melting during the melting. In melt theme, the machine does a traditional raster or line hatching. Figure 3.36 shows a picture of the beam trajectory followed with "Melt theme". The blue part represents the part (square geometry) and the red lines the beam trajectory.

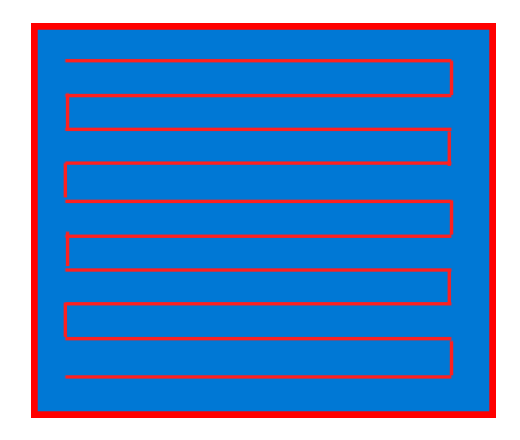


Figure 3.36: Melt theme beam trajectory

Since the scan speed cannot be modified directly to a desired value, the beam follows an extremely high speed, independently of the speed function selected. However, it was possible to see the marks left in the build plate confirming the beam trajectory. It was found that the "UseRotatingHatch" option doesn't deactivate or activate completely the rotation between layers, it just uses 90° rotation (OFF) and 45° (ON) between layers. The contours parameters worked as expected.

The next studied build theme was the "Point-net" one. This theme is not commonly used; however, it was decided to be studied because it provides a quasi-point scan strategy instead of a traditional raster scan. The idea of applying this theme for a solid part instead of only wireframe geometries, could be interesting since point-like scan strategies have been proved to deliver good results as previously stated. The exact functioning of this theme is not well documented in literature, however the effect of each parameter is similar to point-scan strategies applied in other machines, so it is assumed that their values affect in the same way the beam behavior in the ARCAM A1 machine. The amount of process parameters for this theme is much smaller compared to the Melt theme. It consists only of 4 parameters: Current,

Spot time, Focus offset, and Block offset. Figure 3.37 shows a picture of the Point-net build theme parameters window.



Figure 3.37: Point-Net Build Theme process parameters

The first parameter is the "Current", which is just the power of the electron beam as seen previously in traditional process parameters, the higher, the more energy delivered per point. Next is the "Spot time", this one is the amount of time the electron beam stays at a specific point (Maximum =1000 ms). Then, the "Focus offset" parameter, which also as the traditional process parameter, alters the beam diameter at the powder surface, default value of 0 mA was used. The final parameter is the "Block offset", which influence is not clear, but was left with its default value (TRUE).

In "Point Net theme" the machine does a point scan strategy; however, it follows only the contour of the part. The geometry used was the same as the one used for the Melt theme experiments. Figure 3.38 shows a picture of the beam trajectory followed with "Point Net theme". The blue part represents the part (square geometry) and the red lines the beam trajectory. As seen, the red dots represent the scanning points delivered at the contour of the part, they're discrete points and not continuous lines like in traditional fusion strategies.

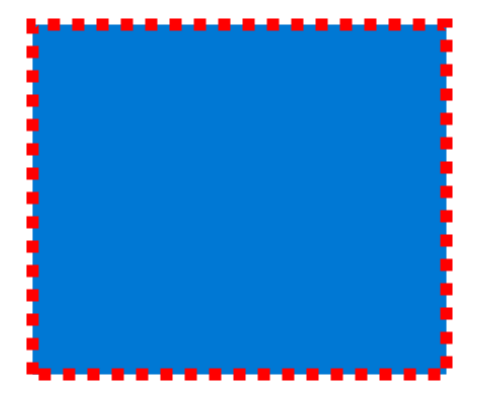


Figure 3.38: Point Net theme beam trajectory

Finally, the last build theme studied was "Wafer" one. This theme is also commonly used to melt support structures. As stated before, a common practice is to use "Melt theme" to melt the solid geometries and "Wafer theme" to melt the support structures. However, it was decided to be studied because this theme allows to precisely control the beam current and

the scan speed with fixed values. Figure 3.39 shows a picture of the Wafer build theme

parameters window.

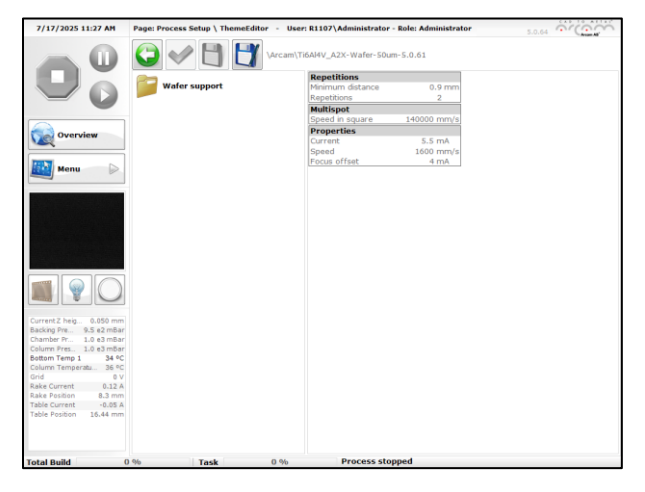


Figure 3.39: Wafer Build Theme process parameters

The first parameter is the "Minimum distance". Not much information is available, but it is deducted from the experiments that it defines the minimum spacing between two scan lines below which a second melting pass will not be applied. Then is the "Repetitions" parameter, which defines how many repetitions will be done if the minimum distance between scan lines is surpassed. Multiple experiments and at the end the "Repetitions" parameter was set to 1. The next parameter is the "Multispot speed in square". This parameter refers to the beam movement speed when the multispot pattern is being used. The multispot creates multiple beams at the same time; In reality, it's just moving the beam extremely fast to create these multiple melt pools quasi-simultaneously. This parameter was left as default as it is not possible to manually deactivate it in this software version.

The next parameters are the classical beam parameters: Current, Speed and Focus offset. These parameters are the same classical parameters described before. The interesting part of this is that Wafer mode allows to set a specific fixed value of these process parameters, which means that the energy density could be exactly calculated. Regarding the beam trajectory and behavior, Wafer theme follows only the contour of the geometry as Point-Net theme. However, it makes continuous scanning and not points. Figure 3.40 shows a picture of the beam trajectory followed with "Wafer theme". Again, the blue part represents the part (square geometry) and the red line the beam trajectory.



Figure 3.40: Wafer theme beam trajectory

This exploratory work was very useful to completely understand the effect of each option and parameter in the beam trajectory. The objective was to find a way to control the beam in order to follow a specific fusion strategy and a specific energy density, instead of just using the traditional fusion strategy used by default.

3.3.3 Melting order of the models

Another important finding was the fact that the order of the melting of the parts can be controlled. It is worth recalling that this machine doesn't allow a lot of customization like other PBF machines. Therefore, in order to simplify the process chain, a typical set-up for fabricating is to put all the parts in a single model, select the build theme, and let the machine fabricate it without much information on how the beam scans the parts. Parts are only divided if a specific set of parameters (typically the speed function) want to be individually modified. However, for this study, the objective is to study different fusion strategies, and the melting order of the parts is something that is very important to achieve it.

To study this, a set of experiments was developed with five squared parts, in order to visualize the effect of different configurations in the "Process" window. The objective was to study what will happen if the five parts are included in the same step or if its melting order can be controlled when multiple steps are used. Figure 3.41 shows the geometry used to study the melting order in this machine. Each square corresponds to a single part, therefore, there is a total of five parts that need to be configured in the process window.

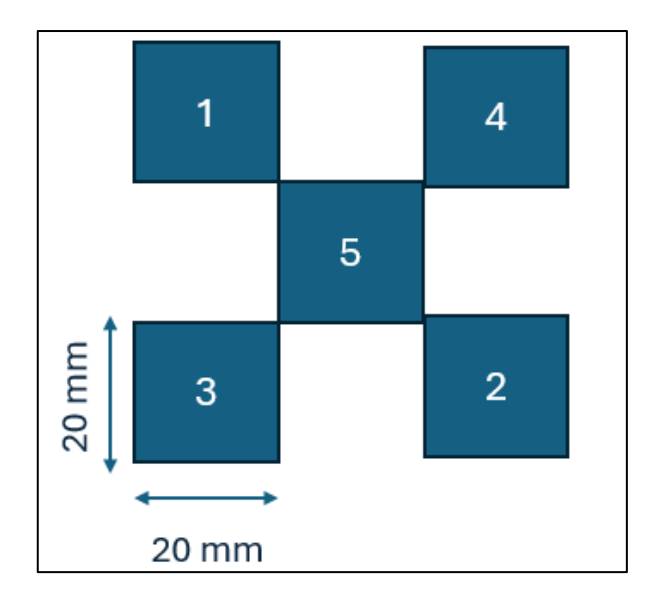


Figure 3.41: Geometry used for studying melting order

The first configuration was configuring all the five parts in the same step. The classic "Melt" theme was used to make these trials. Figure 3.42 shows how this configuration was done in the "Process" window (left image). Only the "Step 1" is activated, in here, the five parts are selected at the same time in the "Model" section. This configuration led to a quasi-simultaneous melting of the five parts as seen in Figure 3.42 (right image). In this configuration, the machine treats the five parts as if it were only one, melting it almost at the same time.

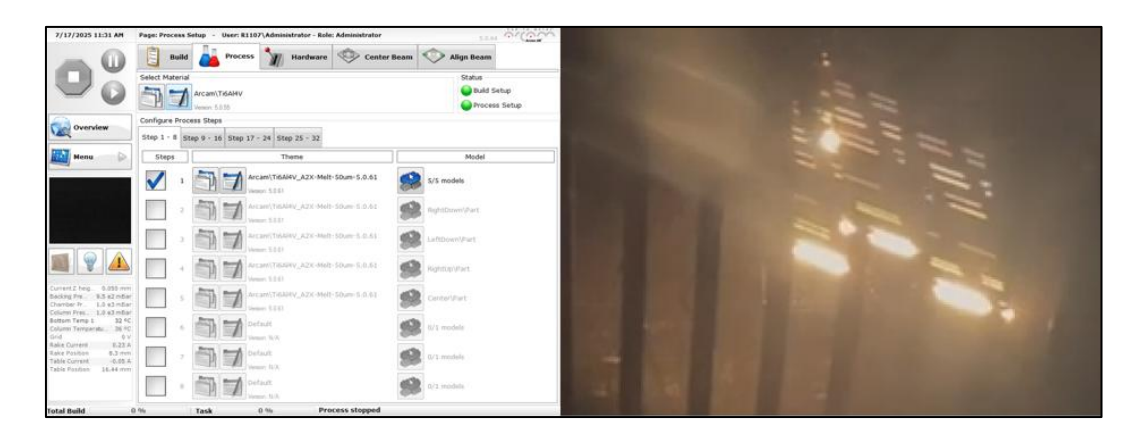


Figure 3.42: Melting parts at the same time

In the other hand, the other configuration consisted of activating five steps, one for each part. Step 1 corresponded to Part 1 (Upper-left one), Step 2 to Part 2 (Lower-right one) and so on with the other steps and parts as seen in Figure 3.43 (left image). This configuration resulted in the melting of each part one by one at the order indicated in the process steps. Figure 3.43 (right image) shows the melting of the first part (upper left), then the melting of the second part is done, until all the parts are fully melted.

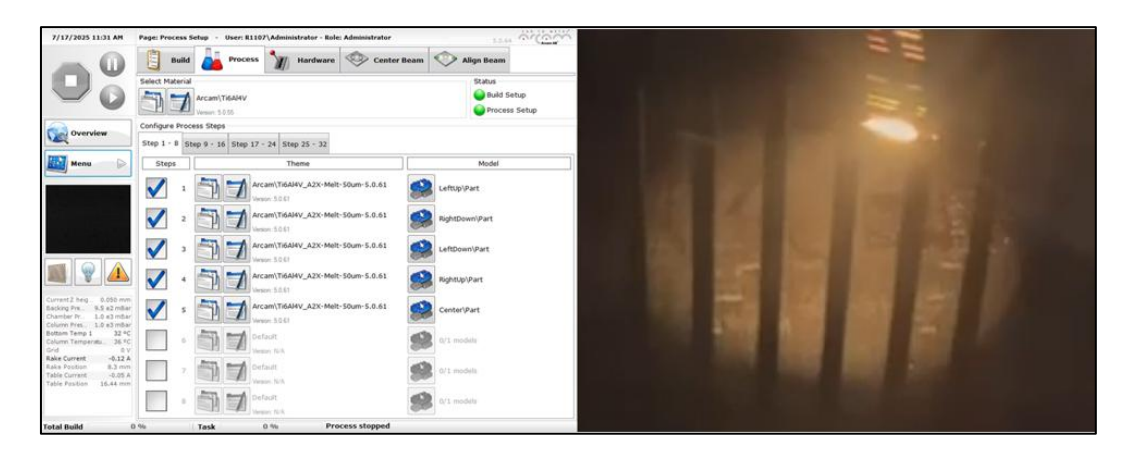


Figure 3.43: Melting parts at configured order

This set of experiments demonstrated that it is possible to control the melting order of the parts. This allows to therefore propose a fusion strategy based on the division of the part into subparts. By controlling the process steps, thus, the order of melting of each subpart, it is possible to melt the part completely in a desired way. Reducing in this way the scanning length and applying lower energy densities at the same time.

This idea of controlling the melting order of models, combined with the knowledge obtained about the process parameters and build themes in the ARCAM A1 machine, it was possible to elaborate an experimental plan to evaluate the influence of different fusion strategies in fabricating parts without support structures.

3.4 Experimental plan with Melt and Point-net theme

To study the effect of different fusion strategies, the Melt build theme and the point net theme were used to plan the first experiments. These first experiments were done with the machine software version of EBMControl 5.0. A series of one-factor-at-a-time (OFAT) experiments were done, and the different approaches are explained in the following sections.

3.4.1 CAD division into small squares (colors)

The first approach was dividing the part into "subparts" in a chessboard pattern. That merged create the original part. These "subparts" are referred as "colors". This was done with the premise of having small scan lengths during melting. Nevertheless, the geometry is kept the same in all cases. Figure 3.44 illustrates this idea of dividing the part into subparts with an example of 4 colors.

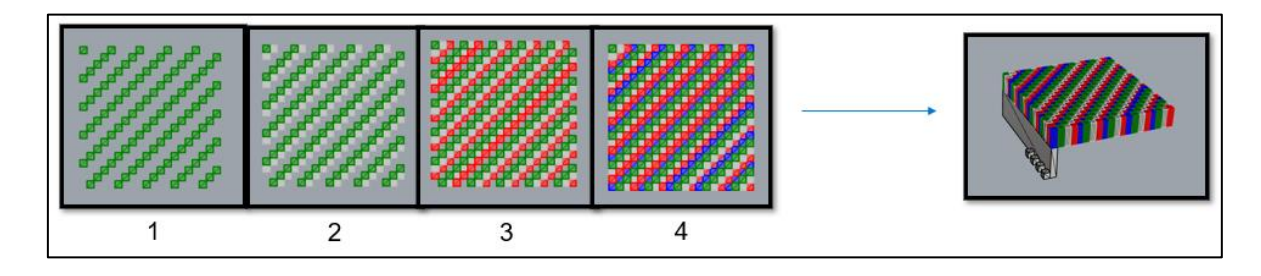


Figure 3.44: Part division into subparts (colors)

Melt theme was used to study a traditional raster strategy and Point-net theme was used to study a point-based scan strategy. Default parameters previously mentioned for each theme were used; however, the contours and the rotating hatch were deactivated for all experiments, and the square size was fixed in 1 mm. 8 total experiments were done with this approach: 4 with Melt theme and 4 with point-net theme. 4 total amounts of colors were studied: 1 color (which is basically the normal part), 2 colors, 3 colors and 4 colors. Figure 3.45 shows the 4 different patterns studied in this first approach.

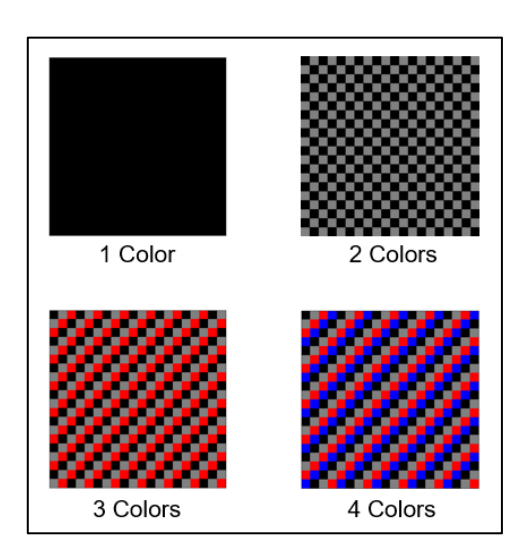


Figure 3.45: Patterns with different amount of colors

The experimental plan for this first approach is summarized in Table 3.4. All the parts were successfully printed without many differences in terms of geometrical accuracy. However, if one should be selected, the one with 4 colors delivered the best results.

Table 3.4: Experimental	plan for study	ing different	number of colors

Part	ARCAM Build theme	Parameter changed
M01	Melt	1 Color
M02	Melt	2 Colors
M03	Melt	3 Colors
M04	Melt	4 Colors
P01	Point-Net	1 Color
P02	Point-Net	2 Colors
P03	Point-Net	3 Colors
P04	Point-Net	4 Colors

3.4.2 Size of squares

The second approach consisted of studying the influence on reducing the square size and therefore, the scan length. For doing this, the square size of the chessboard pattern previously used was reduced to three different values. The number of colors per part was kept constant at 4. While all the other parameters were kept by default for both build themes, keeping the same configuration as the last approach. Figure 3.46 shows the 3 different square sizes studied in the second approach.

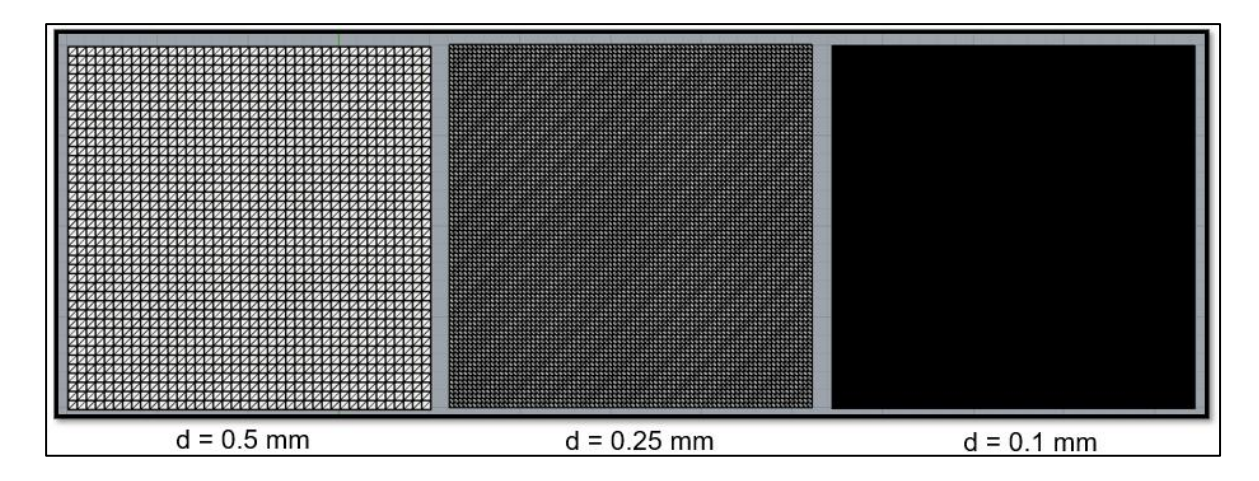


Figure 3.46: Patterns with different square sizes

The experimental plan for this approach is summarized in Table 3.5. However, this build failed due to rake collision. It was seen that the amount of energy density was too high in some parts which caused severe deformation in the process, that then led the rake to collide with the parts and stop the fabrication immediately. In terms of geometrical accuracy, not many conclusions could be obtained. However, in surface quality, qualitatively speaking, was better in the parts with square size of 0.5 mm.

Table 3.5: Experimental plan for studying different square sizes

Part	ARCAM Build theme	Parameter changed
M05	Melt	Square size = 0.5 mm
M06	Melt	Square size = 0.25 mm
M07	Melt	Square size = 0.1 mm
P05	Point-Net	Square size = 0.5 mm
P06	Point-Net	Square size = 0.25 mm
P07	Point-Net	Square size = 0.1 mm

3.4.3 Energy density reduction

After the results of the second approach, it was seen that the energy density applied in those experiments was too high. Therefore, another approach was to reduce the energy density. To do this, in Melt theme, the speed function was increased, while in Point-Net theme, the beam current and spot time was reduced, as explained previously. The number of colors was fixed to 2, and the square size to 0.5 mm. The experimental plan for this approach is summarized in Table 3.6.

Table 3.6: Experimental plan for studying lower energy densities

Part	ARCAM Build theme	Parameter changed
M08	Melt	Speed Function = 70
M09	Melt	Speed Function = 100
M10	Melt	Speed Function = 150
P08	Point-Net	Current = 2.5 mA Spot time = 0.5 ms
P09	Point-Net	Current = 1.5 mA Spot time = 0.25 ms
P10	Point-Net	Current = 1.0 mA Spot time = 0.1 ms

All parts were successfully printed except for one: P10. In P10, the energy density was so low that the electron beam did not fuse the material. Again, not many differences or improvements were observed in terms of geometric accuracy within the experiments done with this approach.

3.4.4 Waiting time between melts

The last approach with EBMControl 5.0 was done with the objective of studying the effect of having some waiting times between melts. For doing this, the part was divided into a different pattern with a much bigger square size. The part is divided into a pattern of 4 colors, the first color is melted, then a waiting time is done by melting another part, then the second color is melted, then other waiting time is done, and in that order is done until all the part is melted. Default parameters with Melt theme were used to fabricate the part. Figure 3.47 shows an image of the pattern used for this approach.

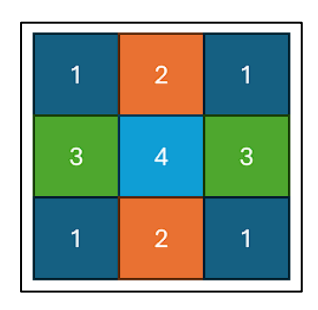


Figure 3.47: Pattern for waiting times between melts

To make the waiting times, the part was placed between some other parts during a build. Then, in the "Process" window, the process steps were configured to make the desired order and sequence. This was done because in EBMControl, there is not an option to indicate precisely a time between melting of parts. Figure 3.48 shows the set-up done for this approach, the part between the other parts without touching each other.

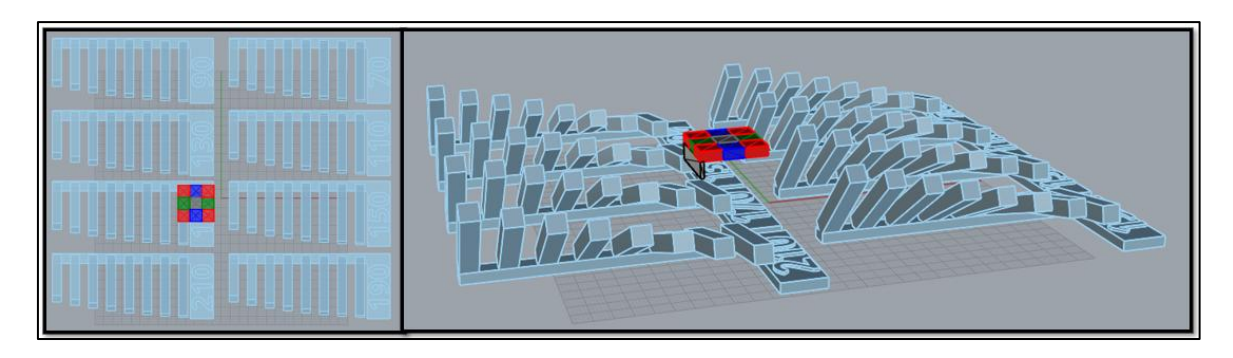


Figure 3.48: Set-up for time between melts (Melt theme)

The choice of these specific parts for the waiting time was arbitrarily, it was just done to introduce some time between melts. The part was successfully printed. However, no significant differences were observed in terms of geometrical accuracy.

3.4.5 Problematic with EBMControl 5.0

The problem of using EBMControl 5.0 with the build themes of "Melt" and Point-Net" is that it doesn't allow to precisely control to the user's desire, the energy density applied into the material. In "Melt" theme, there's multiple ARCAM functions that modify the beam current and scan speed automatically as shown previously. These functions, at least in this machine, are not possible to be deactivated. This means, that with "Melt" theme, is not possible to configure a specific fixed amount of energy density. These ARCAM functions are protected by copyright, and their exact functioning is not clearly understood. In the other hand, in "Point-net" theme, the distance between points cannot be controlled in this machine software version, which is an important parameter to quantify the energy density applied.

The other problem is that with the first methodology applied, it is not possible to control the beam trajectory. The machine does a simple raster hatching strategy with not much personalization possible regardless of the build theme used. This limits the amount of

flexibility to apply different fusion strategies. Additionally, "Wafer" theme allows to precisely control the energy density, but the "multispot" option cannot be disabled in this software version, which significantly alters the resulting fusion strategy applied into the material.

This reason led to explore other options to fabricate the parts. One of these options was to change the software version of the machine. The software version was changed to EBMControl 3.2, and it was found that this version contains more options in the process parameters which allows to precisely control the levels of energy in "Wafer" theme and "Point-Net" theme. However, in "Melt" theme, even though there were more options that apparently allowed to modify the values of beam current and scan speed, it was not possible to control them after multiple experiments. The most influential process parameters identified for each build theme are summarized in the tables below. Highlighted in italic and underlined, the parameters that are only able to be modified in EBMControl 3.2.

Table 3.7: Process parameters for ARCAM Melt theme

Parameter	Effect
Line offset (mm)	Distance between hatching lines
Speed function	ARCAM function which modifies the current and speed depending on the scan length, therefore, the energy density
UseRotatingHatch	Varies between 45° or 90° rotation between layers
Focus offset (mA)	Controls the focusing of the beam

Table 3.8: Process parameters for ARCAM Point-Net theme

Parameter	Effect
Current (mA)	Beam current used for melting
Spot time (ms)	Amount of time the beam stays in one point
<u>Point distance</u> (mm)	Distance between point scans
Focus offset (mA)	Controls the focusing of the beam
<u>Multispot</u>	Deflects the beam rapidly to have quasi-multiple beams at same time

Table 3.9: Process parameters for ARCAM Wafer theme

Parameter	Effect
Current (mA)	Beam current used for melting
Speed (mm/s)	Scan speed for each vector length
Focus offset (mA)	Controls the focusing of the beam
<u>Multispot</u>	Deflects the beam rapidly to have quasi-multiple beams at same time

The change of software version to EBMControl 3.2, allowed to properly control the energy density and fusion strategy applied to melt the material, as it also allowed to control the beam trajectory. This will be explained later in this chapter.

3.5 Experimental plan with Wafer theme

As mentioned earlier, the software version of the machine was changed to EBMControl 3.2. Therefore, all the following experiments were done with EBMControl 3.2 in combination with the Wafer theme, due to its ability to precisely control the process parameters to control the energy density.

3.5.1 Controlled waiting time between melts

The fact that with "Wafer" theme it is possible to control the beam current and scan speed precisely, it is possible to create a specific geometry to precisely control the waiting time between melts. It is worth recalling that in this machine it is not possible to directly control the time between melts or layers, therefore strategies like this one should be used. In this approach, the same pattern of 4 colors as before was used. Additionally, dimensionless extruded lines were used to quantify the waiting time between melts. The part is melted normally with "Melt" theme with default parameters, while the extruded lines are just scanned with a low beam current and 1 mm/s scan speed with "Wafer" theme to precisely control the time by the length of the line. Figure 3.49 shows the set-up done for this approach.

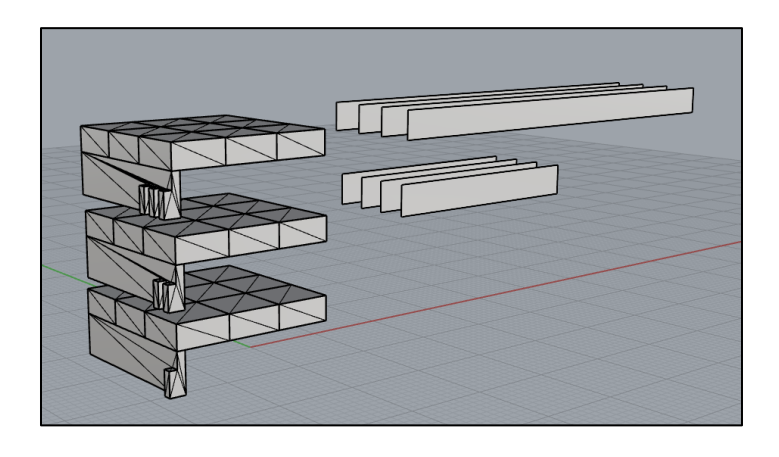


Figure 3.49: Set-up for time between melts (Wafer theme)

The waiting times studied in this approach were 0, 30 and 60 seconds. All the other parameters were kept fixed. The experimental plan for this approach of waiting times between melts is summarized in Table 3.10.

Table 3.10: Experimental plan for studying waiting times between melts with Wafer theme

Part	ARCAM Build theme	Parameter changed
M12	Melt + Wafer	Waiting time = 0 s
M13	Melt + Wafer	Waiting time = 30 s
M14	Melt + Wafer	Waiting time = 60 s

The parts were successfully printed. However, not visible differences or improvements were seen between the parts.

3.5.2 Fusion strategies with Netfabb

After multiple experiments, it was found that with Autodesk Netfabb software it is possible to generate Common Layer Files (.CLF) which can be imported into ARCAM Build Assembler software. Additionally, in some cases, it is also possible to generate directly ARCAM Build Files (.ABF) which can be directly imported into the ARCAM A1 machine. It was found that with "Wafer" theme, it is possible to follow the same trajectory present in the CLF files. This allowed to precisely control the scanning strategy applied into the material.

The ability to generate different hatching strategies with Netfabb, and the fact that with "Wafer" theme it is possible to precisely control the energy density applied into the material provided this method with complete flexibility to apply and study different fusion strategies to fabricate the part.

To quantify the energy density, the Volumetric Energy Density (VED) equations are used. These equations are commonly used in literature for PBF processes to quantify the energy density [104], [105], [106]. In a traditional raster scan, which is the case of "Wafer" theme, equation (3.1) is used, where "U" is the Acceleration voltage (60 kV), "I" is the beam current (mA), "v" is the scan speed (mm/s), "h" is the hatch distance (mm), and "t" is the layer thickness (50 μ m).

$$VED = \frac{U \cdot I}{v \cdot h \cdot t}$$
 (3.1)

In the other hand, for point scan strategies, like in the case of "Point-Net" theme, equation (3.2) is used, where "U" is the Acceleration voltage (60 kV), "I" is the beam current (mA), "t_{on}" is the spot time (ms), "s" is the spot distance (mm), and "t" is the layer thickness (50 µm).

$$VED = \frac{U \cdot I \cdot t_{on}}{s^2 \cdot t} \tag{3.2}$$

VED equations are expressed in (J/mm³) units. It is important to notice that all these parameters are perfectly able to be configured with "Wafer" theme and "Point-Net" theme with EBMControl 3.2. Additionally, the hatch distance can directly be configured when doing the hatching strategy with Netfabb.

In the first experiments done with Netfabb, three fusion strategies were selected, a "normal" line or raster hatching, a "quad islands" hatching, which is similar to a chessboard pattern, and a "radial" hatching. The three fusion strategies used for the first set of experiments with Netfabb are shown in Figure 3.50.

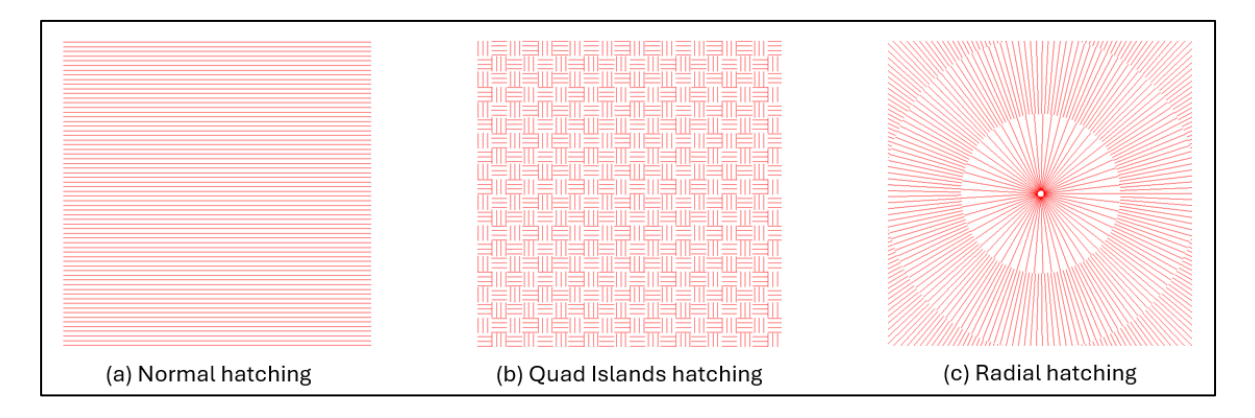


Figure 3.50: Fusion strategies for first set of experiments with Netfabb

For the energy density, the value of 40 J/mm³ was selected. This value has been obtained from latent heat of fusion of pure Titanium equal to 1.76 J/mm^3 and from the latent heat of vaporization of pure Titanium equal to 39.57 J/mm^3 , also considering an absorption coefficient of $\eta = 0.6$. This value has been previously studied by authors working with the same technology and material and it is also the energy value achieved by the automatic functions of ARCAM machines [107], [108].

A total of six parts were planned for this set of experiments with "Wafer" theme. Two levels of energy for each fusion strategy, 40 J/mm³ and 13.33 J/mm³, the energy density was changed by modifying the value of hatch distance (0.1 mm and 0.3 mm respectively). All the other process parameters present in the VED equation were kept the same for all parts: Acceleration voltage (U=60 kV), Beam current (I=15mA), Scan speed (v=4500 mm/s) and Layer thickness (t=0.05 mm), these values are typical values used and are perfectly achievable with the ARCAM A1 machine. Default parameters for each strategy were used, just the layer rotation was deactivated for all experiments. Table 3.11 summarizes the experimental plan followed for the first experiments with different fusion strategies done with Netfabb software and "Wafer" theme. The value of energy density was decreased to a third of the original value to also evaluate its influence in the geometrical accuracy of the printed part without supports.

	Table 3.11: Experim	nental plan for st	tudving different	t fusion strategi	es with Netfabb
--	---------------------	--------------------	-------------------	-------------------	-----------------

Part	ARCAM Build theme	Parameter changed
		Normal hatching
L01	Wafer	$VED = 40 \text{ J/mm}^3$
		h = 0.1 mm
		Normal hatching
L02	Wafer	$VED = 13.33 \text{ J/mm}^3$
		h = 0.3 mm
		Quad Islands hatching
L03	Wafer	$VED = 40 \text{ J/mm}^3$
		h = 0.1 mm
		Quad Islands hatching
L04	Wafer	$VED = 13.33 \text{ J/mm}^3$
		h = 0.3 mm
		Radial hatching
L05	Wafer	$VED = 40 \text{ J/mm}^3$
		h = 0.1 mm
		Radial hatching
L06	Wafer	$VED = 13.33 \text{ J/mm}^3$
		h = 0.3 mm

All the parts were successfully printed. The "Quad Islands" strategy delivered the best results in terms of geometrical accuracy, as expected by the literature review. The second-best results were delivered by the "Normal" hatching and the worst results by the "Radial" hatching. Also, the hatch distance of 0.3 mm delivered the best results in all parts due to a lower energy density applied. It is worth explaining that this same set-up was performed with the same levels of energy with "Point-Net" theme. However, all the prints failed due to external reasons, therefore, this theme was no longer considered for this study.

3.5.3 Design of Experiments for Quad Islands strategy

Based on the results obtained from the first trial of experiments with Netfabb, it was decided to perform a Design of Experiments (DOE) with the Quad Islands fusion strategy, which delivered the best results as expected. This was done with the objective of studying the effect of the parameters of the hatching strategy (square size and gap distance) and the energy density (by modifying hatch distance). Figure 3.51 illustrates the parameters studied for the DOE, where "s" is the square size, "d" the gap distance and "h" the hatch distance.

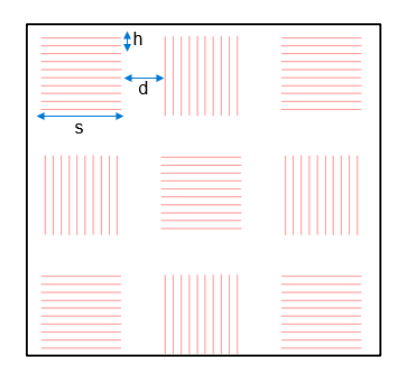


Figure 3.51: Parameters studied for DOE of Quad Islands strategy

A three-factor, three-level Box-Behnken Design (BBD) was chosen to perform the Design of Experiments (DOE) as part of the Response Surface Methodology (RSM), with the objective of studying the influence of each parameter in the output or response factors, which are explained later in this chapter. The factors and levels studied for the DOE are detailed in Table 3.12, where all units are in millimeters (mm).

Table 3.12: Factors and levels for the DOE

Factor	Level [-1]	Level [0]	Level [+1]
Hatch distance (h)	0.1	0.25	0.5
Square size (s)	0.5	0.75	1.0
Gap distance (d)	0.1	0.25	0.5

The total number of experiments in a Box-Behnken Design is calculated with equation (3.3). Where "k" is the number of factors (3 in this case), and "c₀" is the number of center points. A total of 4 center points were used to estimate the experimental error and improve the precision of the model.

Total number of experiments =
$$2k(k-1) + c_0$$
 (3.3)

After applying equation (3.3) a total of 16 experiments were obtained. A Python routine together with the PyDOE2 library was used to generate the experimental runs. Same as the previous experiments, all the other process parameters present in the VED equation were kept the same for all parts: Acceleration voltage (U=60 kV), Beam current (I=15mA), Scan speed (v=4500 mm/s) and Layer thickness (t=0.05 mm).

Table 3.13: Experimental plan for studying Quad Islands strategy

Part	Hatch distance	Square size	Gap distance
1 art	(h)	(s)	(d)
Q01	0.1	0.5	0.25
Q02	0.5	0.5	0.25
Q03	0.1	1.0	0.25
Q04	0.5	1.0	0.25
Q05	0.1	0.75	0.1
Q06	0.5	0.75	0.1
Q07	0.1	0.75	0.5
Q08	0.5	0.75	0.5
Q09	0.25	0.5	0.1
Q10	0.25	1.0	0.1
Q11	0.25	0.5	0.5
Q12	0.25	1.0	0.5
Q13	0.25	0.75	0.25
Q14	0.25	0.75	0.25
Q15	0.25	0.75	0.25
Q16	0.25	0.75	0.25

All the parts were successfully printed. However, in some of the parts the bonding was not strong enough to withstand the stresses during powder removal step, causing these parts to fragmentate and collapse. These parts were: Q02, Q04, Q08, Q11 and Q12. All the other parts were properly consolidated, with different levels of geometrical accuracy, density and porosity. The evaluation methodology to assess the parts are explained in the following subchapter.

3.6 Evaluation methods to assess part quality

To assess the quality of the parts fabricated without support structures, three parameters were measured. First, the geometrical accuracy of the fabricated part by using a Scanner 3D to scan the parts. Then, the density and porosity of the part is measured using an analytical balance and a recipient with demineralized water.

3.6.1 Geometrical accuracy measurement

For the measurement of geometrical and dimensional accuracy of the parts, a metrology grade 3D scanner from the company Creaform is used, more specially, the HandySCAN 3D Silver 700, which has an accuracy of up to 0.030 mm [109]. The software used for the 3D scanner is VXelements. A black plate with circular markers is used as a reference grid, then the part is placed on top, and it is scanned from multiple angles until a good recreation of the geometry is obtained. Figure 3.52 shows the set-up used for the 3D scanning of the parts.



Figure 3.52: Physical set-up for the 3D scanning of the parts

A minimum of two scans per part were done, with the objective of scanning all the part from all possible angles. When the first scan is done, the part is oriented in the next direction and scanned again, this process is repeated until all the part is correctly scanned. Then, all the scans are aligned with three common points in order to position them as it were a single part. Then, the aligned scans are merged to recreate a single part with all the features of the geometry scanned from all angles, obtaining in this way, the scanned part with all the features properly registered. At the end, an STL file is exported with the scanned part. The operation of aligning and merging two scans together is shown in Figure 3.53.

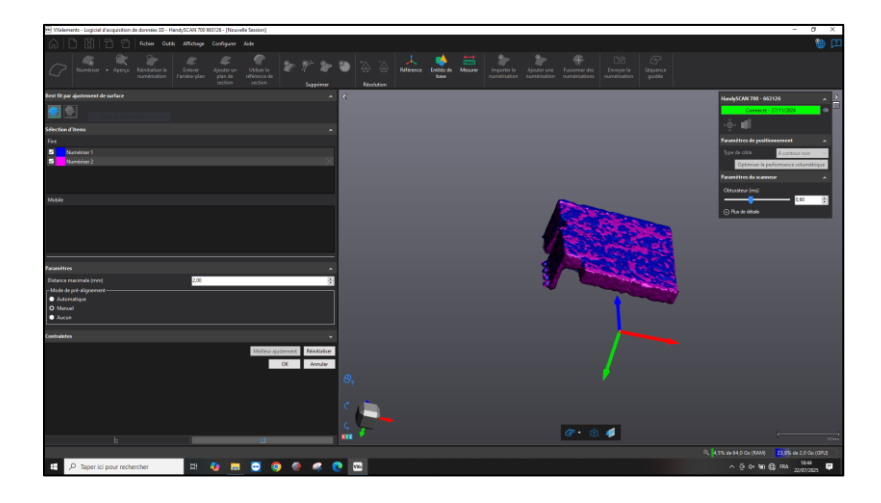


Figure 3.53: Aligning and merging of scans

After the scanned part is properly exported in STL format. It is imported into the software CloudCompare, where the comparison with the CAD file is done. A Python routine is used to generate the CAD file with the identification cuboids corresponding to the scanned part, then the STL is also imported into CloudCompare. Then, in the software, the two meshes are aligned again by picking 4 points in common between the two meshes. Once they're properly aligned, the option "Compute cloud/mesh distance" is used. The CAD part is used as "reference" while the scanned part is used as "compared". The scalar field is generated, showing the distances between the scanned part and the CAD part. Figure 3.54 shows an example of a scalar field of a comparison between a scanned part and its CAD.

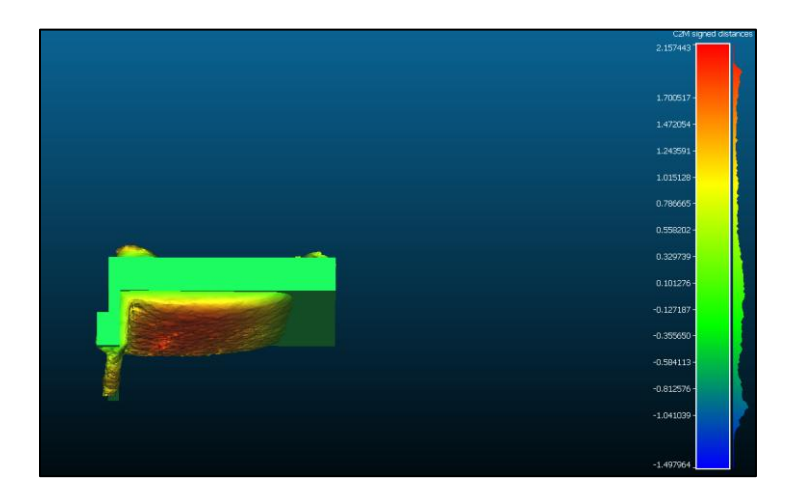


Figure 3.54: Scalar field between scanned part and its CAD

Finally, the software is used to compute a series of statistical parameters with the data. Using a Gaussian distribution, it is possible to export a .CSV file with all the points and the distances. With this, it is possible to calculate the Mean deviation, Standard Deviation, Root mean square (RMS), Min deviation and Max deviation. All these parameters help to quantify the amount of deformation in the part and allow to measure the geometrical accuracy of the parts fabricated. Due to lime limitation with the equipment, only the parts done with "Wafer" theme and Netfabb (LXX and QXX) were analyzed with the 3D scanner and the software CloudCompare. These parts were selected because they were the ones where the energy density and the fusion strategy was completely controlled as mentioned earlier.

3.6.2 Measurement of density and porosity

To measure the density of the parts, the Archimedes method was used. Taking as reference the instructions proposed by the standards ASTM B311 and ISO 3369. The analytical balance used was a KERN ABS 120-4 with readability of 0.1 mg.



Figure 3.55: Analytical balance used for measurements

Additionally, a laboratory beaker with demineralized water from the brand Onyx is used as the measurement liquid. The procedure for measuring the density was the following: First, the part is tied with a thin cotton thread. Then, the part is put on the balance, and the mass of the part is recorded (m_{air}). Then, the beaker with demineralized water is placed on the balance and the balance is set to zero with the TARE button. Finally, the part hanging from the thread is submerged completely into the liquid without touching the walls and once the measured value stabilizes, the mass is recorded (m_{sub}). Figure 3.56 shows an image of the set-up used for measuring the density of the parts.



Figure 3.56: Physical set-up for measuring density

Once the mass in air (m_{air}) and submerged mass (m_{sub}) of the part is obtained, equation (3.4) is used to calculate the part's density. The density of the demineralized water is obtained from standardized tables [110], with a value of 0.9975 g/cm³ corresponding to the measured temperature of 23°C.

$$\rho_{part} = \frac{m_{air}}{m_{sub}} \cdot \rho_{H2O} \tag{3.4}$$

Once the density of the part is calculated (ρ_{part}), equation (3.5) is used to calculate the part's porosity. Where ρ_0 is the density of Ti6Al4V alloy, which has a value of 4.43 g/cm³ [111].

$$P = \left(1 - \frac{\rho_{part}}{\rho_0}\right) \cdot 100 \tag{3.5}$$

The measurements of density and porosity reveal important information on the quality of the parts. Low density and high porous parts directly correlate with low mechanical properties like fatigue and tensile strength. It also permits to identify defects like lack of fusion, balling, or delamination.

Measuring the deviation from the CAD model alongside density and porosity provides a comprehensive assessment of the quality of parts fabricated without supports. The mean deviation quantifies geometric accuracy, revealing distortions, warping, or sagging typically caused by poor thermal management in unsupported features. Meanwhile, density and porosity measurements expose internal defects related to insufficient fusion or overheating. Together, these metrics offer insight into both external dimensional fidelity and internal structural integrity, giving a broad understanding of the part quality.

4 Results and Discussion

In this chapter, the results obtained for each experiment are presented. As mentioned before, the porosity measurement was done for all the experiments, providing insightful information on the mechanical properties of the parts manufactured without support structures. However, the geometric accuracy measurement was only done for the experiments where the energy density and fusion strategy was totally controlled (Wafer theme with Netfabb software). In this chapter, only the graphs with the synthesized data are shown. However, all the raw data and pictures are available in the Appendix section.

4.1 Results of Melt and Point-Net theme experiments

This section describes the results of porosity measurements for the parts manufactured with the "Melt" and "Point-Net" theme with EBMControl 5.0. Additionally, it presents the results of the first experiments done with EBMControl 3.2 where Wafer mode was used to control the time between melts as explained in the previous section. It is worth recalling that in all these experiments there were not observed any significant differences between the parts in terms of geometrical accuracy from a qualitative point of view, since a pronounced warping in the overhang area is observed in all parts. Nevertheless, the porosity measurements provide good information on the mechanical integrity of the parts depending on the parameters used with ARCAM Build themes.

4.1.1 Results by number of colors

The first approach explored the division of the part into subparts or colors as explained before. The results are presented in Figure 4.1. This graph shows the results of porosity for 1 Color, 2 Colors, 3 Colors and 4 Colors respectively. It is seen that "Melt" theme parts (MXX) have very similar values of porosity as "Point-Net" theme parts (PXX) with the exemption of M1 and P1, where in P1 only the "foot" and borders where fabricated. It is seen that porosity increases when the amount of colors increases, only until 4 colors are reached, then it reaches an intermediate value. Regarding the porosity values, the lowest value is obtained by the M1 part, as expected, since it uses the default optimized parameters by ARCAM. The measured value is 1.366%, which is very similar to the value of ~1.50%

reported by Ran et al [112] using the same material and method of measurement. Regarding the geometrical accuracy (qualitatively speaking), no significant differences were seen.

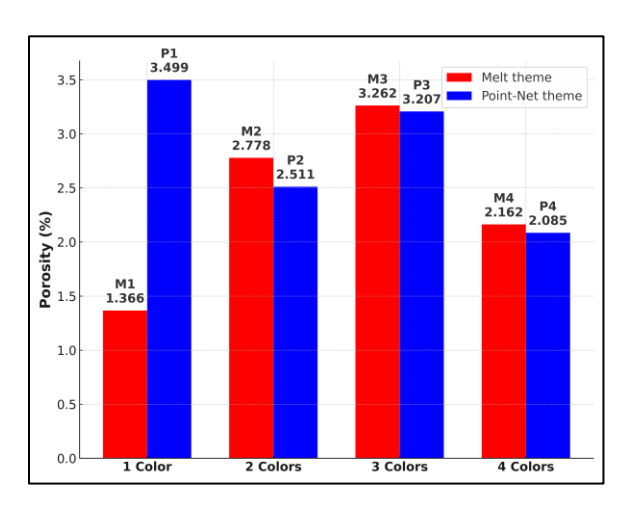


Figure 4.1: Results of measured porosity vs number of colors

4.1.2 Results by size of squares

The second approach involved reducing the square size, therefore the scan length. Three values were studied (0.5, 0.25 and 0.1 mm) with both "Melt" and "Point-Net" themes. As mentioned previously, the build failed due to severe deformation in one of the parts, which caused the rake to deform all the other parts. Therefore, the results obtained may not be correct. No significant trends are observed; however, an increase of porosity is seen for all the parts compared to the previous experimental run (Square size = 1 mm). The results are presented in Figure 4.2.

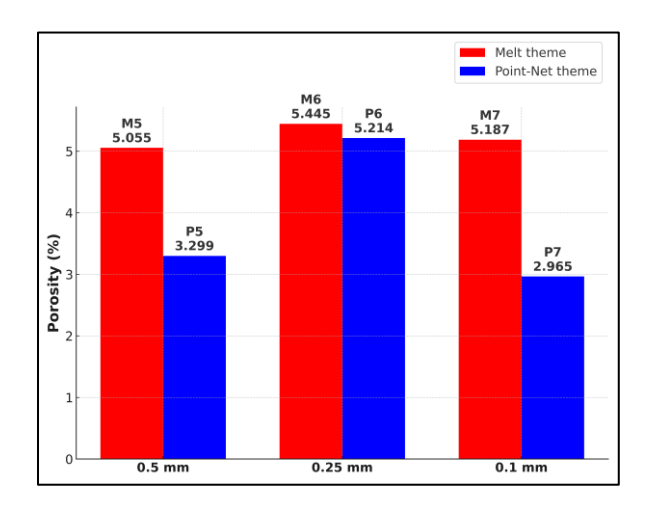


Figure 4.2: Results of measured porosity vs size of squares

4.1.3 Results by energy density reduction

This approach consisted of arbitrarily reducing the energy density in both themes. Three levels for each theme were studied. In "Melt" theme, the Speed Function was increased from

70, 100 to 150 respectively. While in "Point-Net" theme, the beam current and spot time was reduced to I = 2.5 mA / t = 0.5 ms, I = 1.5 mA / t = 0.25 ms and I = 1 mA / t = 0.1 ms respectively. The results are presented in Figure 4.3. A strong correlation is found between the energy density and porosity. As expected, the lower the energy density, the higher the level of porosity in the part with both build themes. Only P10 was not fabricated since the energy was too low to fuse the material. Nevertheless, no significant improvements were seen among the parts in terms of geometrical accuracy.

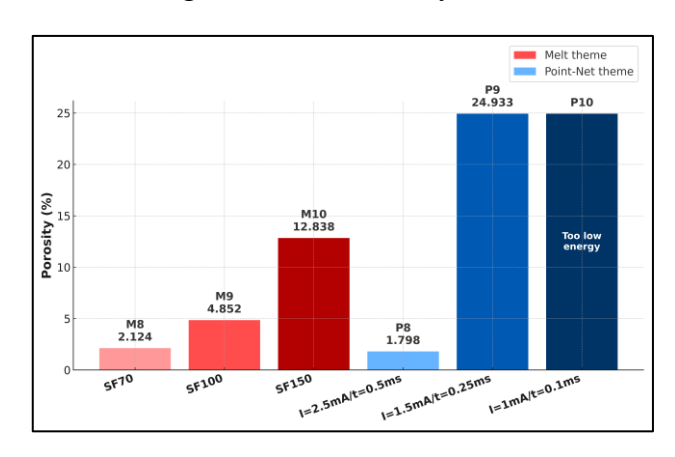


Figure 4.3: Results of measured porosity vs energy density

4.1.4 Results by time between melts

As explained in the methodology section, this approach consisted of trying different waiting times between melts. M11 was done with EBMControl 5.0, therefore it was not possible to exactly control the time between melts. While M12, M13 and M14 were done with EBMControl 3.2 with the help of "Wafer" theme, to precisely control the time between melts. Qualitatively speaking, the best results are observed in M11. Then, a slight improvement is observed with the increase in waiting time in M12, M13 and M14. However, warping is still observed in all parts to some extent. In terms of porosity, M12 delivered the best results from all the experiments. No trends are observed; however, it is seen that increasing the waiting time doesn't have much of an impact in the porosity of the part. The results are presented in Figure 4.4.

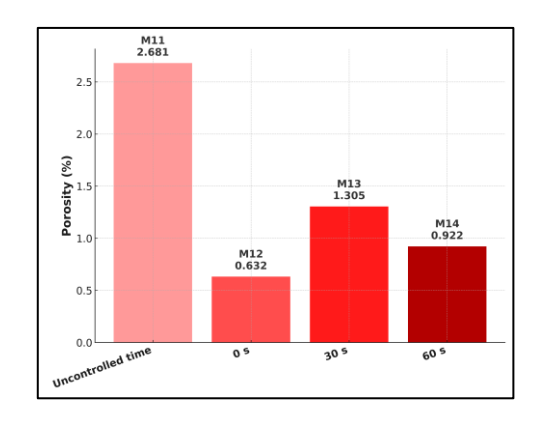


Figure 4.4: Results of measured porosity vs time between melts

4.2 Results of Wafer theme experiments

This section describes the results of the experiments done with "Wafer" theme and EBMControl 3.2. In these experiments, it was possible to control precisely the energy density and fusion strategy applied to manufacture the parts with Netfabb software. For these parts, the density and porosity of the samples was measured, but also the geometrical accuracy as explained before.

4.2.1 Results by different fusion strategies

As explained in the methodology section, three fusion strategies with two different levels of energy density were studied in this approach: Normal hatching (L01 and L02), Quad Islands hatching (L03 and L04) and Radial hatching (L05 and L06). Again, the same correlation between energy density and porosity is observed (lower energy density equals to higher porosity). Best results in terms of porosity are observed in L01, this should be expected since it uses the same parameters as the automatic functions of ARCAM. The results of the porosity measurements are presented in Figure 4.5.

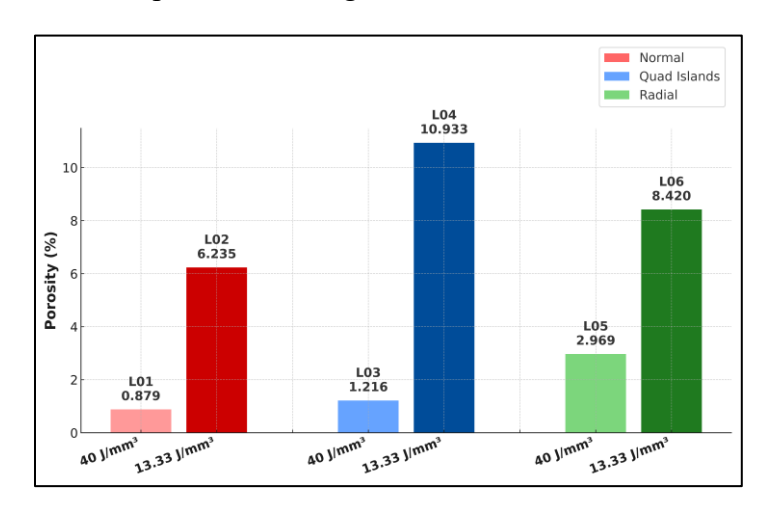


Figure 4.5: Results of measured porosity vs different fusion strategies

Regarding geometrical accuracy, several data were collected. However, three main indicators were selected as the most influential: Mean deviation, Root Mean Square (RMS) and Max deviation. The measurements confirmed the qualitative observations, L04 delivered the best results in terms of geometrical accuracy in all three indicators, while L06 delivered the worst results. Therefore, it was demonstrated again that Quad Islands strategy (L03 and L04) delivers the best results quantitatively and qualitatively, followed by the normal hatching (L01 and L02) and in last place, the radial hatching (L05 AND L06). The measurements of deviation for geometrical accuracy are shown in Figure 4.6. Additionally, Figure 4.7 shows pictures of the six parts manufactured in this experimental run. In here, it is clearly seen that L04 possess the least defects, with practically no warping and just some side loss at the bottom region. Due to this, as previously stated, it was decided to perform the next run of experiments focusing on the Quad Islands strategy, with the objective of finding a set of parameters that could deliver the best results.

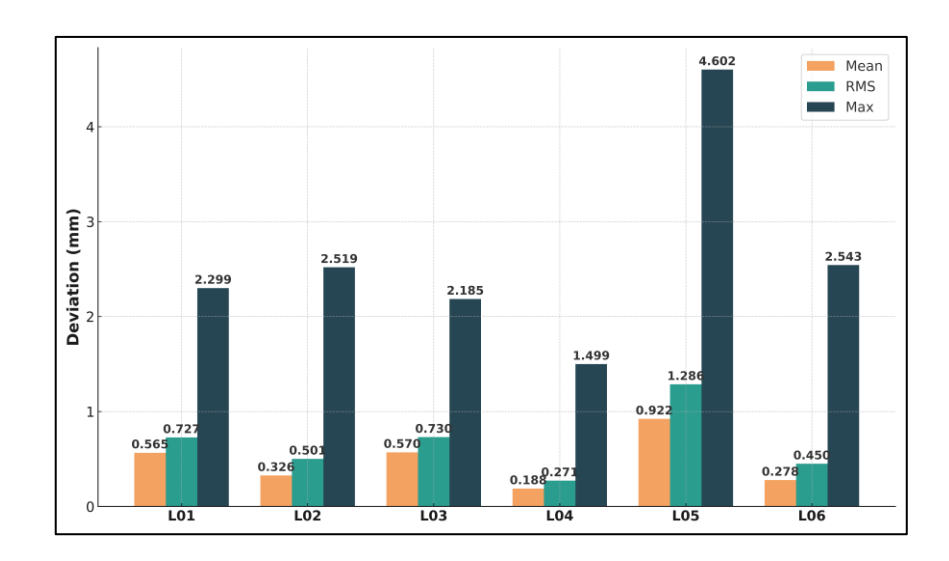


Figure 4.6: Results of measured deviation vs different fusion strategies

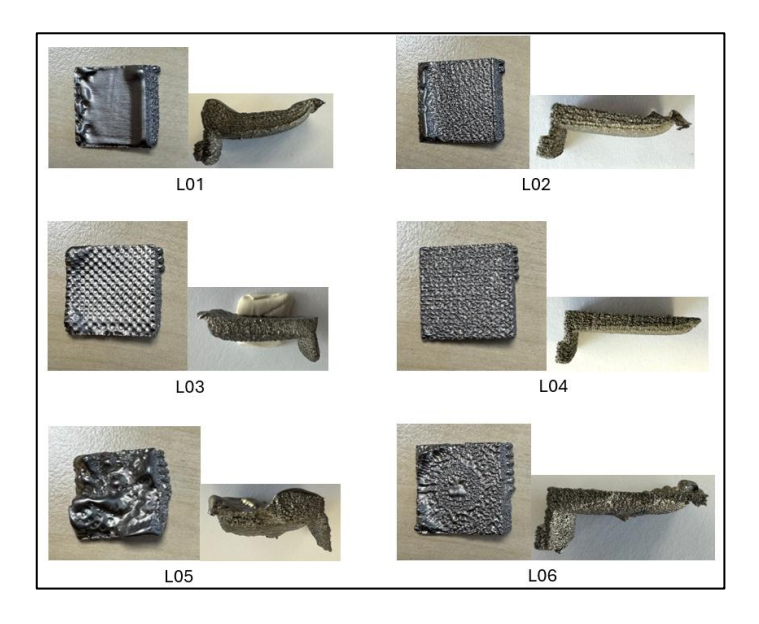


Figure 4.7: Results by different fusion strategies (pictures)

4.2.2 Results of DOE for Quad Islands strategy

The last approach consisted of performing a Design of Experiments (DOE) with a Box-Behnken Design (BBD) of three levels and three factors for the Quad Islands strategy. As mentioned before, all parts were successfully printed except for Q02, Q04, Q08, Q11 and Q12 that got fragmentated and collapsed during powder removal. From a qualitative point of view, in terms of geometrical accuracy, very good results were obtained in some parts. Some parts presented no visible defects in terms of deformation (no warping or side loss). By far, the best results that were obtained in this study. However, it is important to measure the impact of the strategy and parameters selected in the density and porosity of the fabricated part. Results of the measurement of porosity for this experimental run can be seen in Figure 4.8. Best results in terms of porosity were obtained in Q05, which is expected since it had the highest energy density (smallest hatch distance studied in this run). In the other hand, worst measured results were present in Q06, also expected since it had the highest hatch distance studied in the DOE. Q06 is so porous that it is possible for light to pass

through the surface. It has a very poor bonding that caused a region of the part to easily fragmentate.

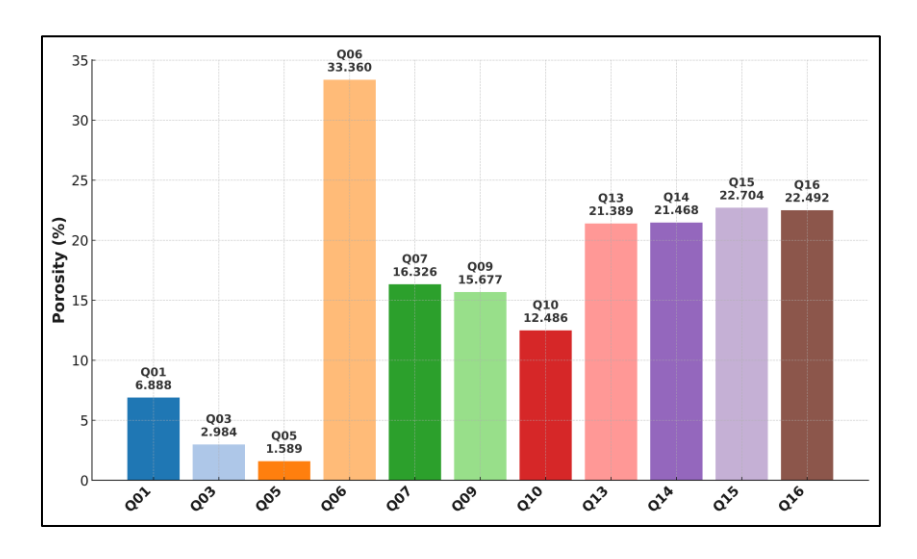


Figure 4.8: Results of measured porosity in Quad Islands strategy

Regarding geometrical accuracy, as previously anticipated, the best qualitative results were observed in parts located at the center of the design (Q13, Q14, Q15, Q16) and in parts like Q06 and Q07, where practically no defects or deformation was observed. These qualitative results were confirmed by the measurements of deviation which can be seen in Figure 4.9. When observing the maximum deviation, which is the highest deviation value from the CAD model, which in this case represents the part defects like warping or side loss; it can be seen that the previously mentioned parts are the ones with the best results. Q06 appears a bit higher but this is due to the fragmentated region and not because of geometrical deformation.

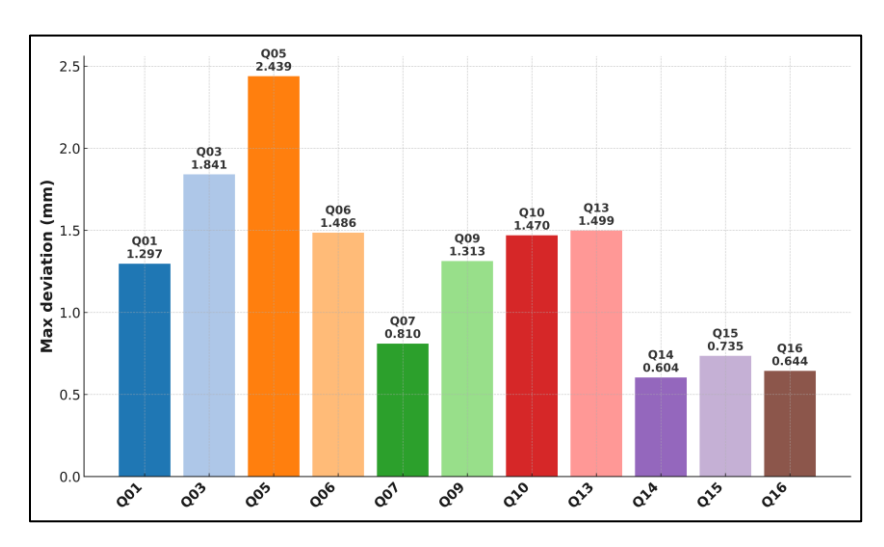


Figure 4.9: Results of measured max deviation in Quad Islands strategy

Additionally, pictures of the results of this experimental run can be seen in Figure 4.10. The best and worst results of this approach were identified, and if only geometrical accuracy is considered, it could be said that replicating the parameters of Q16 per example could deliver good results when printing without support structures. However, it is important to fully

understand the effect of each parameter in both the porosity and the geometrical accuracy of the part, in order to find a set of parameters that delivers a balance between the two. Essentially, a part with good geometrical accuracy and without much porosity that could reduce the mechanical properties would be desired. And for this, it is important to study the effect of each parameter.

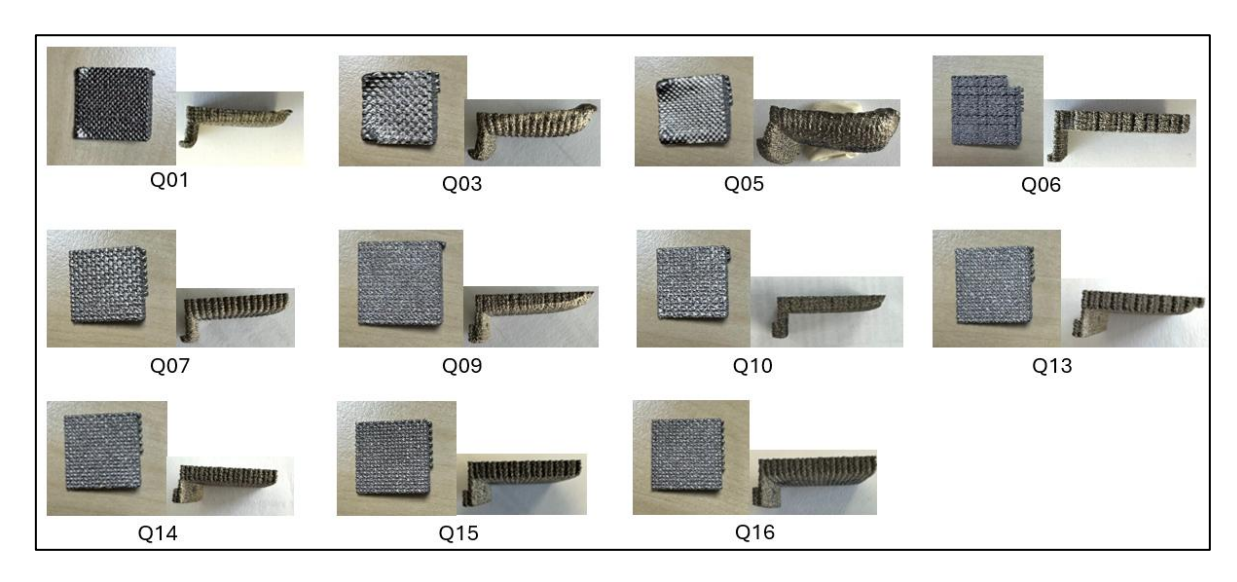


Figure 4.10: Results by Quad Island strategy (pictures)

4.2.3 Effects of Quad Islands parameters

To study the individual effect of each parameter (hatch distance, square size and gap distance) in both the porosity and geometrical accuracy, a series of main effect plots were done to visualize the relations between parameters and outputs. The first main effects plots are the porosity one, shown in the first row of Figure 4.11. The previously mentioned correlation between hatch distance and porosity is clearly visualized here, an increase of hatch distance (therefore reduction of energy density) also increases the level of porosity in the part. Square size seems to not have a direct lineal relation, but it's highest at 0.75 mm. Finally, gap distance seems to also increase the level of porosity. These results are expected since longer distance between scans can induce Lack of Fusion (LoF) defects which then result as pores in the material [113].

In the other hand, the main effects plots of deviation (Mean, RMS and Max) are presented in the next three rows of Figure 4.11. Regarding the hatch distance, it seems to not have a direct linear relation with deviation, but best results are obtained with a value of 0.25 mm in all three indicators. A stronger trend is observed in the square size, where a lower value seems to result in a smaller average deviation from the CAD. This is confirmed in literature, where smaller scan lengths lead to lower thermal deformations in PBF technologies [114], [115]. Finally, gap distance seems to have a very strong relation with deviation, where increasing it reduces the deviation in all three indicators.

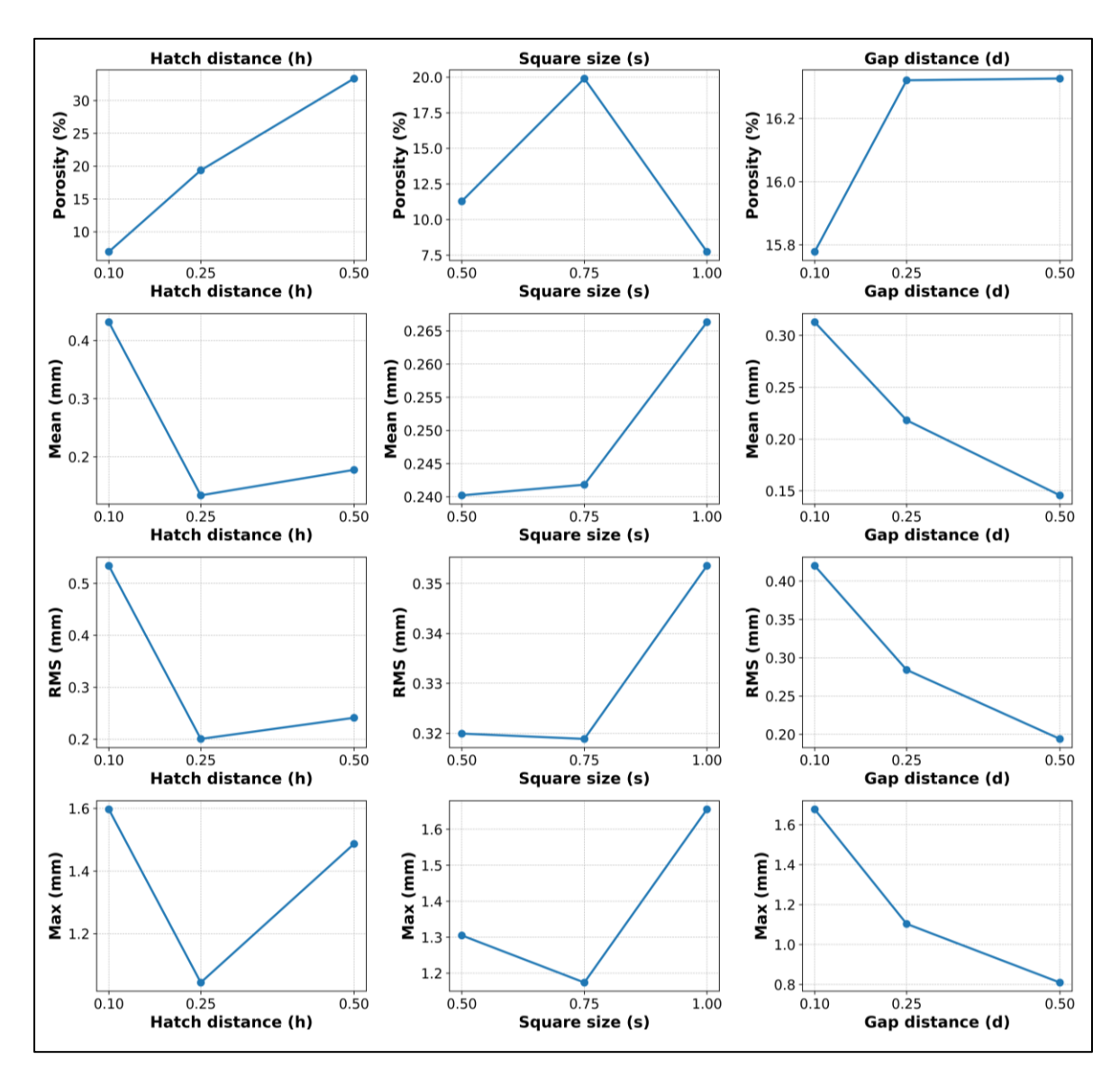


Figure 4.11: Main effects plots for porosity and deviation

In order to visualize the overall effect of the parameters in the porosity and geometrical accuracy, it is necessary to study as well the interaction between them. For this reason, it was decided to include interaction plots, which can be seen in Figure 4.12. Interaction plots reveal when the effect of one factor changes with another, which is critical to estimate two-way interactions and curvature in Box–Behnken designs.

Regarding the porosity, it is seen that in the completely covered regions the interaction between hatch distance and square size reveals that regardless of the square size, porosity seems to increase with the hatch distance. This same phenomenon (porosity \propto hatch distance) occurs in the interaction between hatch distance and a fixed gap distance. A more complex interaction is seen between square size and gap distance, where when the gap distance is the lowest (0.1 mm), square size seems to not have a big impact. However, when gap distance is increased to the intermediate value (0.25 mm), porosity results tend to be good with the smallest value of square size (0.5 mm), and even better with the highest value

of square size (1 mm). Worst results are seen with the intermediate value of square size (0.75 mm).

In the other hand, deviation interactions also provide valuable information on the effects of the parameters. It is seen that in the completely covered regions the interaction between hatch distance and square size reveals that regardless of the square size, an increase in the hatch distance decreases the average deviation. The same occurs in the interaction between hatch distance and gap distance, at a fixed gap distance, overall deviations decrease with the increase of hatch distance. Finally, in the interaction between square size and gap distance, it is seen that at the lowest gap distance (0.1 mm), an increase in the square size from the lowest (0.5 mm) to the intermediate value (0.75 mm) tends to increase the overall deviation, after this intermediate value, an increase of the square size decreases again the overall deviation to its lowest value. However, this behavior is completely reversed if the gap distance is increased to 0.25 mm, where the lowest value of deviation is found in the intermediate value of square size (0.75 mm).

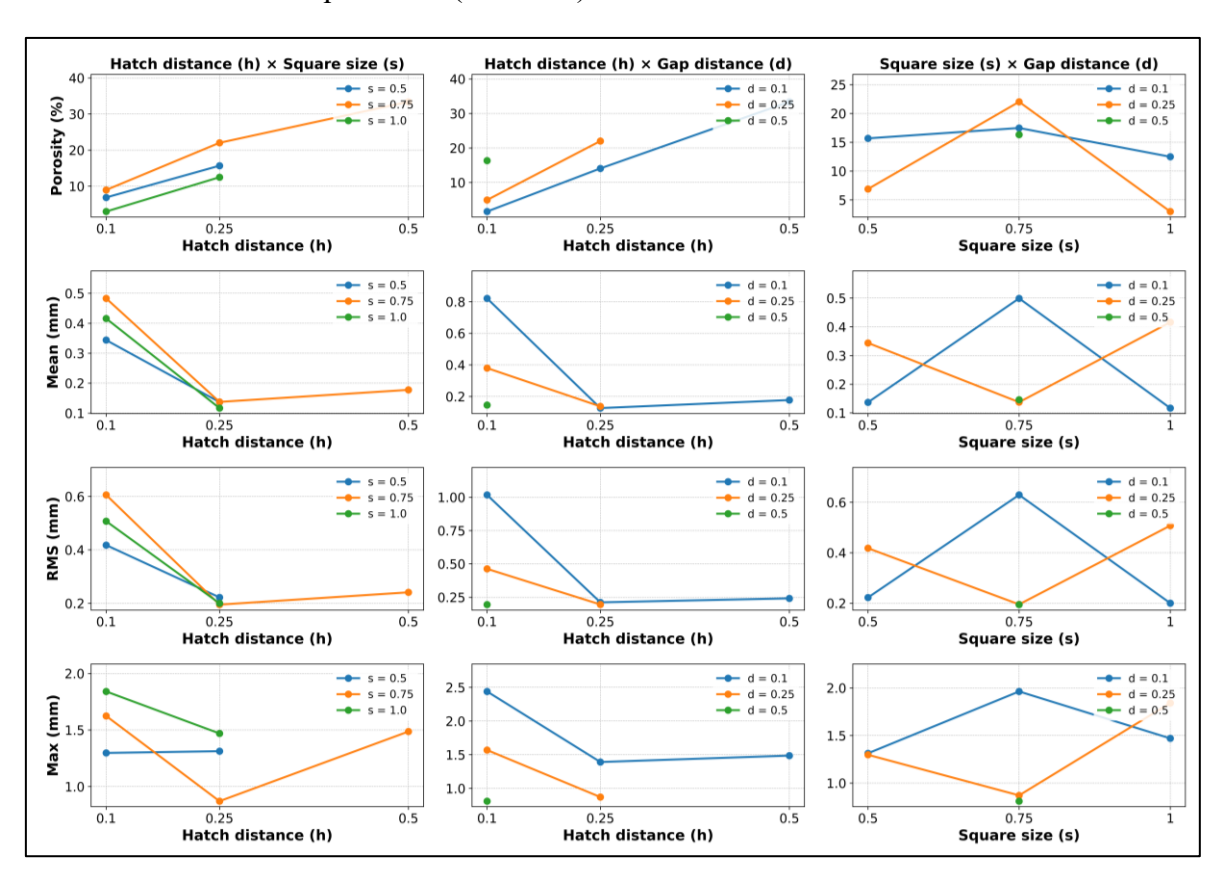


Figure 4.12: Interaction plots for porosity and deviation

To further understand the effect and influence of the parameters in the porosity and geometrical accuracy of the parts, an Analysis of Variance (ANOVA) with Response Surface Methodology (RSM) was performed. After adjusting a series of regression models with the reduction of the non-influential parameters with the p-value, a final set of equations was obtained that relate the indicators (Porosity, Mean, RMS and Max) to the parameters of the Quad Islands strategy (hatch distance, square size and gap distance).

For the porosity, a two-factor interaction (2FI) model was obtained. The equation for porosity can be seen in equation (4.1), where "h" is hatch distance, "s" is square size, and "d" is gap distance, all inputs are entered directly in millimeters (mm). Porosity is obtained directly in percentage (%). This model equation has a R² value of 0.9909, Adjusted R² value of 0.9849, Adeq Precision of 41.5566 and Lack of Fit F-value of 4.99, which means that this model is well adjusted to the data.

Porosity =
$$-4.192 + 67.930 \cdot h - 7.095 \cdot s + 21.310 \cdot d + 147.461 \cdot h \cdot d$$
 (4.1)

For the mean deviation, a Quadratic model was obtained. The equation for mean deviation can be seen in equation (4.2), Mean deviation is obtained directly in millimeters (mm). This model equation has a R² value of 0.9830, Adjusted R² value of 0.9661, Adeq Precision of 24.0677 and Lack of Fit F-value of 2.99, which means that this model is also well adjusted to the data.

Mean =
$$-0.628 - 5.042 \cdot h + 5.467 \cdot s - 1.636 \cdot d + 5.683 \cdot h^2 - 3.610 \cdot s^2$$
 (4.2)

For the RMS deviation, also a Quadratic model was obtained. The equation for RMS deviation can be seen in equation (4.3), RMS deviation is obtained directly in millimeters (mm). This model equation has a R² value of 0.9805, Adjusted R² value of 0.9609, Adeq Precision of 22.4662 and Lack of Fit F-value of 0.7669, which represents a good fit.

$$RMS = -0.736 - 5.751 \cdot h + 6.530 \cdot s - 2.027 \cdot d + 6.326 \cdot h^2 - 4.309 \cdot s^2$$
(4.3)

For the max deviation, again a Quadratic model was obtained. The equation for max deviation can be seen in equation (4.4), Max deviation is obtained directly in millimeters (mm). This model equation has a R² value of 0.7583, Adjusted R² value of 0.6548, Adeq Precision of 7.6206 and Lack of Fit F-value of 0.3218, which represents an inferior fir compared to others.

$$Max = 3.564 - 10.688 \cdot h - 3.797 \cdot d + 14.584 \cdot h^2$$
(4.4)

Additionally, the models were tested with the values of L04 part (closest but still outside the modeled range) obtaining a percentual error of \sim 17% for porosity and \sim 21% for mean deviation. Figure 4.13 shows the 3D Surface graphs that represent the respective models for the porosity, Mean deviation, RMS deviation and Max deviation. In the 3D surface graphs, the most influential parameters can be seen (hatch distance and gap distance in all cases). These parameters were determined by their p-value (lowest).

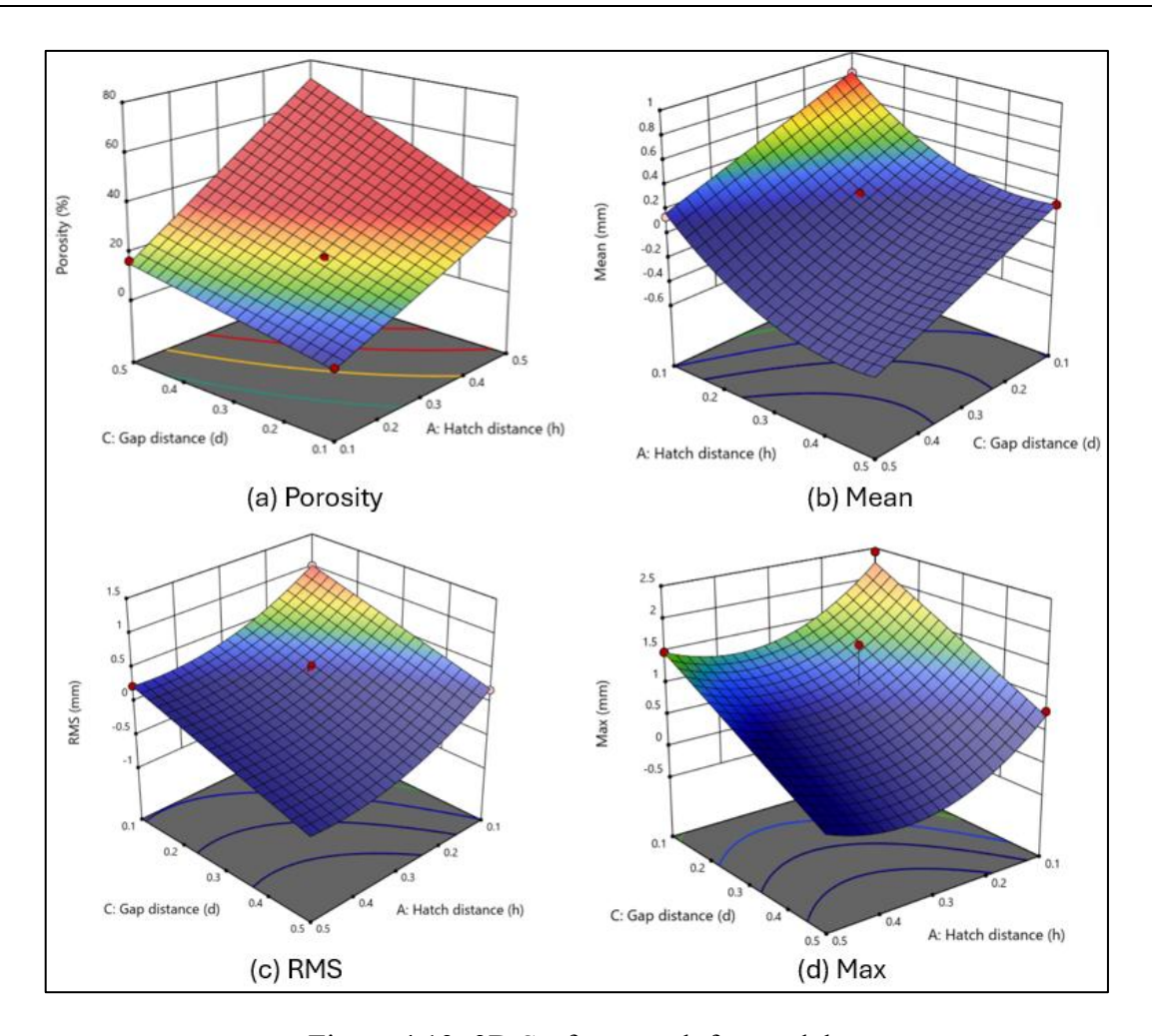


Figure 4.13: 3D Surface graph for models

The results obtained in this study provide insightful information on the ability to use Quad Islands strategy to minimize the use of support structures during manufacturing. For example, if the parameters of Q16 are used (h=0.25, s=0.75 and d=0.25), it is expected to achieve the best studied results in terms of geometrical accuracy, quantitatively and qualitatively speaking. However, it must be considered that these parameters delivered a high level of porosity (~22%), which is very decremental for the mechanical properties of the material.

If the model equations obtained are used to perform a numerical optimization, with a priority on reducing the mean deviation and the porosity, the following set of parameters is a possible solution: hatch distance = 0.1 mm, square size = 0.1 mm and gap distance = 0.416. This set of parameters is expected to deliver the following results: Mean deviation = 0.101 mm and Porosity = 10.505%. Achieving in this way, a part without much geometric deformation and with reduced, yet still quite high, level of porosity.

5 Conclusions

This work consisted of performing a series of experiments on an ARCAM A1 machine, which explored the influence of different fusion strategies, energy density values and process parameters on the geometrical accuracy and porosity of parts manufactured without the use of support structures with EB-PBF technology. Based on the results, it was concluded:

- 1) It is possible to reduce geometric deformations in overhang regions just by changing the fusion strategy to a segmented or discrete scanning method like in Quad Islands strategy.
- 2) Results can also be improved if the volumetric energy density is optimized. However, decreasing the energy density also increases the porosity of the material.
- 3) It was found that each parameter of the fusion strategy has an important effect in the results. Higher hatch distances and gap distances produce lower deformations but increased porosity. Lower square sizes generally reduce thermal deformations due to shorter scanning lengths. Quad Islands strategy and these parameters: (h=0.25, s=0.75 and d=0.25) delivered the best results in terms of geometrical accuracy, with no significant warping or side loss and a mean geometric deviation of only ~0.1 mm; but with a level of porosity of ~22%.

This work demonstrated the fact that it is possible to prevent common geometric defects by optimizing the fusion strategy when manufacturing with EB-PBF, potentially reducing the need for use of support structures. However, modifying the fusion strategy also impacts the density and porosity of the material, which has a significant impact in the mechanical properties. Therefore, it is up to the user whether it is worth sacrificing mechanical properties to some extent for the benefits of manufacturing parts without support structures.

Suggestions for further work

It is suggested to evaluate the impact of other factors and process parameters, for example: random scanning, layer rotation, point-net theme. Additionally, it would be beneficial to develop thermo-mechanical simulations to evaluate the impact of the fusion strategies in the thermal gradients and deformations during the manufacturing process.

Bibliography

- [1] M. Korpela, N. Riikonen, H. Piili, A. Salminen, and O. Nyrhilä, "Additive Manufacturing-Past, Present, and the Future," *Technical, Economic and Societal Effects of Manufacturing 4.0: Automation, Adaption and Manufacturing in Finland and Beyond*, pp. 17–41, Jan. 2020, doi: 10.1007/978-3-030-46103-4 2/TABLES/2.
- J. Edgar and S. Tint, "'Additive Manufacturing Technologies: 3D Printing, Rapid Prototyping, and Direct Digital Manufacturing', 2nd Edition: By Ian Gibson (Deakin University, Australia), David Rosen (Georgia Institute of Technology, USA) and Brent Stucker (University of Louisville, USA), Springer Science+Business Media, New York, USA, 2015, 498 pages, ISBN: 978-1-4939-2112-6, £81.00, €96.29, US\$119.00," *Johnson Matthey Technology Review*, vol. 59, no. 3, pp. 193–198, Apr. 2015, doi: 10.1595/205651315X688406.
- [3] J. L. Amaya-Rivas *et al.*, "Future trends of additive manufacturing in medical applications: An overview," *Heliyon*, vol. 10, no. 5, p. e26641, Mar. 2024, doi: 10.1016/J.HELIYON.2024.E26641/ASSET/CE7A9AAA-6976-42D3-A5C5-EC293D9F3FE3/MAIN.ASSETS/GR001.JPG.
- [4] M. Armstrong, H. Mehrabi, and N. Naveed, "An overview of modern metal additive manufacturing technology," *J Manuf Process*, vol. 84, pp. 1001–1029, Dec. 2022, doi: 10.1016/J.JMAPRO.2022.10.060.
- [5] "ISO/ASTM 52900:2021(en), Additive manufacturing General principles Fundamentals and vocabulary." Accessed: Mar. 31, 2025. [Online]. Available: https://www.iso.org/obp/ui/en/#iso:std:iso-astm:52900:ed-2:v1:en
- [6] S. Rouf *et al.*, "Additive manufacturing technologies: Industrial and medical applications," *Sustainable Operations and Computers*, vol. 3, pp. 258–274, Jan. 2022, doi: 10.1016/J.SUSOC.2022.05.001.
- [7] A. Vafadar, F. Guzzomi, A. Rassau, and K. Hayward, "Advances in Metal Additive Manufacturing: A Review of Common Processes, Industrial Applications, and Current Challenges," *Applied Sciences 2021, Vol. 11, Page 1213*, vol. 11, no. 3, p. 1213, Jan. 2021, doi: 10.3390/APP11031213.
- [8] S. Pratheesh Kumar, S. Elangovan, R. Mohanraj, and J. R. Ramakrishna, "Review on the evolution and technology of State-of-the-Art metal additive manufacturing processes," *Mater Today Proc*, vol. 46, pp. 7907–7920, Jan. 2021, doi: 10.1016/J.MATPR.2021.02.567.

- [9] E. Toyserkani, D. Sarker, O. Obehi Ibhadode, F. Liravi, P. Russo, and K. Taherkhani, "Metal additive manufacturing," *Metal Additive Manufacturing*, pp. 1–594, Oct. 2021, doi: 10.1002/9781119210801.
- [10] M. Fera, R. Macchiaroli, F. Fruggiero, and A. Lambiase, "A new perspective for production process analysis using additive manufacturing—complexity vs production volume," *International Journal of Advanced Manufacturing Technology*, vol. 95, no. 1–4, pp. 673–685, Mar. 2018, doi: 10.1007/S00170-017-1221-1/METRICS.
- [11] R. E. Laureijs, J. B. Roca, S. P. Narra, C. Montgomery, J. L. Beuth, and E. R. H. Fuchs, "Metal additive manufacturing: Cost competitive beyond low volumes," *Journal of Manufacturing Science and Engineering, Transactions of the ASME*, vol. 139, no. 8, Aug. 2017, doi: 10.1115/1.4035420/376354.
- [12] C. Zhang *et al.*, "Additive manufacturing of functionally graded materials: A review," *Materials Science and Engineering: A*, vol. 764, p. 138209, Sep. 2019, doi: 10.1016/J.MSEA.2019.138209.
- [13] M. Srivastava and S. Rathee, "Additive manufacturing: recent trends, applications and future outlooks," *Progress in Additive Manufacturing 2021 7:2*, vol. 7, no. 2, pp. 261–287, Oct. 2021, doi: 10.1007/S40964-021-00229-8.
- [14] D. Dev Singh, T. Mahender, and A. Raji Reddy, "Powder bed fusion process: A brief review," *Mater Today Proc*, vol. 46, pp. 350–355, Jan. 2021, doi: 10.1016/J.MATPR.2020.08.415.
- [15] I. Gibson, D. Rosen, B. Stucker, and M. Khorasani, "Powder Bed Fusion," *Additive Manufacturing Technologies*, pp. 125–170, 2021, doi: 10.1007/978-3-030-56127-75.
- [16] A. Wiberg, "Towards Design Automation for Additive Manufacturing A Multidisciplinary Optimization approach Anton Wiberg FACULTY OF SCIENCE AND ENGINEERING," *Linköping Studies in Science*, p. 69, 2019, Accessed: May 13, 2025. [Online]. Available: www.liu.se
- [17] A. Mazzoli, "Selective laser sintering in biomedical engineering," *Med Biol Eng Comput*, vol. 51, no. 3, pp. 245–256, Mar. 2013, doi: 10.1007/S11517-012-1001-X/FIGURES/4.
- [18] E. M. Sefene, "State-of-the-art of selective laser melting process: A comprehensive review," *J Manuf Syst*, vol. 63, pp. 250–274, Apr. 2022, doi: 10.1016/J.JMSY.2022.04.002.
- [19] J. Nandy, H. Sarangi, and S. Sahoo, "A Review on Direct Metal Laser Sintering: Process Features and Microstructure Modeling," *Lasers in Manufacturing and Materials Processing*, vol. 6, no. 3, pp. 280–316, Sep. 2019, doi: 10.1007/S40516-019-00094-Y/TABLES/4.
- [20] M. Baumers, C. Tuck, and R. Hague, "Selective Heat Sintering Versus Laser Sintering: Comparison of Deposition Rate, Process Energy Consumption and Cost Performance," 2015, *University of Texas at Austin*. Accessed: Jun. 29, 2025. [Online]. Available: https://hdl.handle.net/2152/89312
- [21] D. Zhang *et al.*, "Metal Alloys for Fusion-Based Additive Manufacturing," *Adv Eng Mater*, vol. 20, no. 5, p. 1700952, May 2018, doi: 10.1002/ADEM.201700952.
- [22] F. Lupi, A. Pacini, and M. Lanzetta, "Laser powder bed additive manufacturing: A review on the four drivers for an online control," *J Manuf Process*, vol. 103, pp. 413–429, Oct. 2023, doi: 10.1016/J.JMAPRO.2023.08.022.
- [23] F. Calignano, M. Galati, and L. Iuliano, "A Metal Powder Bed Fusion Process in Industry: Qualification Considerations," *Machines 2019, Vol. 7, Page 72*, vol. 7, no. 4, p. 72, Nov. 2019, doi: 10.3390/MACHINES7040072.

- [24] A. Staub, "Mitigation of Thermal History-related Issues in Selective Laser Melting," Oct. 2022, doi: 10.3929/ETHZ-B-000574668.
- [25] "Arcam Q10 Technical Data", Accessed: May 13, 2025. [Online]. Available: www.arcam.com
- [26] "SDS EOS M 290 | EOS GmbH." Accessed: May 13, 2025. [Online]. Available: https://www.eos.info/metal-solutions/metal-printers/data-sheets/sds-eos-m-290
- [27] E. Damri, E. Tiferet, D. Braun, Y. I. Ganor, M. Chonin, and I. Orion, "Effects of Gas Pressure during Electron Beam Energy Deposition in the EBM Additive Manufacturing Process," *Metals 2021, Vol. 11, Page 601*, vol. 11, no. 4, p. 601, Apr. 2021, doi: 10.3390/MET11040601.
- [28] N. Hrabe, T. Gnäupel-Herold, and T. Quinn, "Fatigue properties of a titanium alloy (Ti–6Al–4V) fabricated via electron beam melting (EBM): Effects of internal defects and residual stress," *Int J Fatigue*, vol. 94, pp. 202–210, Jan. 2017, doi: 10.1016/J.IJFATIGUE.2016.04.022.
- [29] M. Leary, T. Maconachie, A. Sarker, O. Faruque, and M. Brandt, "Mechanical and thermal characterisation of AlSi10Mg SLM block support structures," *Mater Des*, vol. 183, p. 108138, Dec. 2019, doi: 10.1016/J.MATDES.2019.108138.
- [30] M. Roudnicka, M. Misurak, and D. Vojtech, "Differences in the Response of Additively Manufactured Titanium Alloy to Heat Treatment-Comparison between SLM and EBM," *MANUFACTURING TECHNOLOGY*, vol. 19, no. 4, 2019, Accessed: Jul. 19, 2025. [Online]. Available: http://www.scopus.com
- [31] S. Lewin *et al.*, "Additively manufactured mesh-type titanium structures for cranial implants: E-PBF vs. L-PBF," *Mater Des*, vol. 197, p. 109207, Jan. 2021, doi: 10.1016/J.MATDES.2020.109207.
- [32] T. De Terris, T. Baffie, and C. Ribière, "Additive manufacturing of pure copper: a review and comparison of physical, microstructural, and mechanical properties of samples manufactured with Laser-Powder Bed Fusion (L-PBF), Electron Beam Melting (EBM) and Metal Fused Deposition Modelling (MFDM) technologies," *International Journal of Material Forming*, vol. 16, no. 4, pp. 1–25, Jul. 2023, doi: 10.1007/S12289-023-01755-2/TABLES/13.
- [33] C. Körner, "Additive manufacturing of metallic components by selective electron beam melting a review," *International Materials Reviews*, vol. 61, no. 5, pp. 361–377, 2016, doi: 10.1080/09506608.2016.1176289.
- [34] L. Dall'Ava, H. Hothi, A. Di Laura, J. Henckel, and A. Hart, "3D Printed Acetabular Cups for Total Hip Arthroplasty: A Review Article," *Metals 2019, Vol. 9, Page 729*, vol. 9, no. 7, p. 729, Jun. 2019, doi: 10.3390/MET9070729.
- [35] L. C. Zhang, Y. Liu, S. Li, and Y. Hao, "Additive Manufacturing of Titanium Alloys by Electron Beam Melting: A Review," *Adv Eng Mater*, vol. 20, no. 5, p. 1700842, May 2018, doi: 10.1002/ADEM.201700842.
- [36] L. E. Murr, "Metallurgy of additive manufacturing: Examples from electron beam melting," *Addit Manuf*, vol. 5, pp. 40–53, Jan. 2015, doi: 10.1016/J.ADDMA.2014.12.002.
- [37] "Additive manufacturing using selective electron beam melting FAU CRIS." Accessed: Jul. 19, 2025. [Online]. Available: https://cris.fau.de/publications/118839644/
- [38] M. F. Zäh and S. Lutzmann, "Modelling and simulation of electron beam melting," *Production Engineering*, vol. 4, no. 1, pp. 15–23, Feb. 2010, doi: 10.1007/S11740-009-0197-6/FIGURES/8.

- [39] X. Tan, Y. Yihongkok, S. B. Tor, and C. K. Chua, "Application of Electron Beam Melting (EBM) in Additive Manufacturing of an Impeller," *Proceedings of the International Conference on Progress in Additive Manufacturing*, vol. 0, pp. 327–332, 2014, doi: 10.3850/978-981-09-0446-3 076.
- [40] L. Portolés, O. Jordá, L. Jordá, A. Uriondo, M. Esperon-Miguez, and S. Perinpanayagam, "A qualification procedure to manufacture and repair aerospace parts with electron beam melting," *J Manuf Syst*, vol. 41, pp. 65–75, Oct. 2016, doi: 10.1016/J.JMSY.2016.07.002.
- [41] V. Lunetto, M. Galati, L. Settineri, and L. Iuliano, "Unit process energy consumption analysis and models for Electron Beam Melting (EBM): Effects of process and part designs," *Addit Manuf*, vol. 33, p. 101115, May 2020, doi: 10.1016/J.ADDMA.2020.101115.
- [42] C. Ghibaudo *et al.*, "Information-rich quality controls prediction model based on non-destructive analysis for porosity determination of AISI H13 produced by electron beam melting," *International Journal of Advanced Manufacturing Technology*, vol. 126, no. 3–4, pp. 1159–1173, May 2023, doi: 10.1007/S00170-023-11153-2/FIGURES/1.
- [43] X. Gong, T. Anderson, and K. Chou, "Review on Powder-Based Electron Beam Additive Manufacturing Technology," *ASME/ISCIE 2012 International Symposium on Flexible Automation, ISFA 2012*, pp. 507–515, Jul. 2013, doi: 10.1115/ISFA2012-7256.
- [44] A. Ataee, Y. Li, G. Song, and C. Wen, "Metal scaffolds processed by electron beam melting for biomedical applications," *Metallic Foam Bone: Processing, Modification and Characterization and Properties*, pp. 83–110, Jan. 2017, doi: 10.1016/B978-0-08-101289-5.00003-2.
- [45] J. A. Tamayo, M. Riascos, C. A. Vargas, and L. M. Baena, "Additive manufacturing of Ti6Al4V alloy via electron beam melting for the development of implants for the biomedical industry," *Heliyon*, vol. 7, no. 5, p. e06892, May 2021, doi: 10.1016/J.HELIYON.2021.E06892.
- [46] A. Talib Khanjar and N. Hadi Jasim Al Hasan, "A Brief Review of Electron beam melting (EBM) manufacturing of Ti-6Al-4V alloy for biomedical applications," *Journal of Manufacturing Innovations*, vol. 1, no. 1, pp. 83–102, Jan. 2023, doi: 10.22055/JOMI.2024.7.
- [47] A. Nouri and A. Sola, "Electron beam melting in biomedical manufacturing," *Metallic Biomaterials Processing and Medical Device Manufacturing*, pp. 271–314, Jan. 2020, doi: 10.1016/B978-0-08-102965-7.00008-4.
- [48] M. K. Kolamroudi, M. Asmael, M. Ilkan, and N. Kordani, "Developments on Electron Beam Melting (EBM) of Ti–6Al–4V: A Review," *Transactions of the Indian Institute of Metals*, vol. 74, no. 4, pp. 783–790, Apr. 2021, doi: 10.1007/S12666-021-02230-9/TABLES/1.
- [49] I. Buj-Corral, A. Tejo-Otero, and F. Fenollosa-Artés, "Development of AM Technologies for Metals in the Sector of Medical Implants," *Metals 2020, Vol. 10, Page 686*, vol. 10, no. 5, p. 686, May 2020, doi: 10.3390/MET10050686.
- [50] M. Galati, "Electron beam melting process: a general overview," *Addit Manuf*, pp. 277–301, Jan. 2021, doi: 10.1016/B978-0-12-818411-0.00014-8.
- [51] P. Wang, W. J. Sin, M. L. S. Nai, and J. Wei, "Effects of Processing Parameters on Surface Roughness of Additive Manufactured Ti-6Al-4V via Electron Beam Melting," *Materials 2017, Vol. 10, Page 1121*, vol. 10, no. 10, p. 1121, Sep. 2017, doi: 10.3390/MA10101121.

- [52] E. Attar, "Simulation of Selective Electron Beam Melting Processes," Technischen Fakultät der Universität Erlangen-Nürnberg, 2011. Accessed: Jul. 20, 2025. [Online]. Available: https://www.researchgate.net/publication/296063041_Simulation_of_Selective_Electron_Beam_Melting_Processes
- [53] P. Karimi, E. Sadeghi, J. Ålgårdh, and J. Andersson, "EBM-manufactured single tracks of Alloy 718: Influence of energy input and focus offset on geometrical and microstructural characteristics," *Mater Charact*, vol. 148, pp. 88–99, Feb. 2019, doi: 10.1016/J.MATCHAR.2018.11.033.
- [54] J. Romano, L. Ladani, J. Razmi, and M. Sadowski, "Temperature distribution and melt geometry in laser and electron-beam melting processes A comparison among common materials," *Addit Manuf*, vol. 8, pp. 1–11, Oct. 2015, doi: 10.1016/J.ADDMA.2015.07.003.
- [55] M. Q. Zafar, C. C. Wu, H. Zhao, J. Wang, and X. Hu, "Finite element framework for electron beam melting process simulation," *The International Journal of Advanced Manufacturing Technology 2020 109:7*, vol. 109, no. 7, pp. 2095–2112, Jul. 2020, doi: 10.1007/S00170-020-05707-X.
- [56] N. Ahmed, I. Barsoum, G. Haidemenopoulos, and R. K. A. Al-Rub, "Process parameter selection and optimization of laser powder bed fusion for 316L stainless steel: A review," *J Manuf Process*, vol. 75, pp. 415–434, Mar. 2022, doi: 10.1016/J.JMAPRO.2021.12.064.
- [57] A. Ducato, L. Fratini, M. La Cascia, and G. Mazzola, "An Automated Visual Inspection System for the Classification of the Phases of Ti-6Al-4V Titanium Alloy," *Lecture Notes in Computer Science (including subseries Lecture Notes in Artificial Intelligence and Lecture Notes in Bioinformatics)*, vol. 8048 LNCS, no. PART 2, pp. 362–369, 2013, doi: 10.1007/978-3-642-40246-3 45.
- [58] M. Xiu, Y. T. Tan, S. Raghavan, M. H. Goh, M. Ling, and S. Nai, "The Effect of Heat Treatment on Microstructure, Microhardness and Pitting Corrosion of Ti6Al4V Produced by Electron Beam Melting Additive Manufacturing Process," *The International Journal of Advanced Manufacturing Technology*, Nov. 2021, doi: 10.21203/RS.3.RS-1071502/V1.
- [59] X. Tan *et al.*, "Graded microstructure and mechanical properties of additive manufactured Ti–6Al–4V via electron beam melting," *Acta Mater*, vol. 97, pp. 1–16, Sep. 2015, doi: 10.1016/J.ACTAMAT.2015.06.036.
- [60] S. S. Al-Bermani, M. L. Blackmore, W. Zhang, and I. Todd, "The origin of microstructural diversity, texture, and mechanical properties in electron beam melted Ti-6Al-4V," *Metall Mater Trans A Phys Metall Mater Sci*, vol. 41, no. 13, pp. 3422–3434, Dec. 2010, doi: 10.1007/S11661-010-0397-X/FIGURES/13.
- [61] A. Safdar, "A study on Electron Beam Melted Ti-6Al-4V," 2012. Accessed: Jul. 20, 2025. [Online]. Available: https://portal.research.lu.se/en/publications/a-study-on-electron-beam-melted-ti-6al-4v
- [62] H. K. Rafi, N. V. Karthik, H. Gong, T. L. Starr, and B. E. Stucker, "Microstructures and mechanical properties of Ti6Al4V parts fabricated by selective laser melting and electron beam melting," *J Mater Eng Perform*, vol. 22, no. 12, pp. 3872–3883, Dec. 2013, doi: 10.1007/S11665-013-0658-0/FIGURES/14.
- [63] T. Pasang *et al.*, "Directionally-Dependent Mechanical Properties of Ti6Al4V Manufactured by Electron Beam Melting (EBM) and Selective Laser Melting (SLM)," *Materials 2021, Vol. 14, Page 3603*, vol. 14, no. 13, p. 3603, Jun. 2021, doi: 10.3390/MA14133603.

- [64] X. Zhao *et al.*, "Comparison of the microstructures and mechanical properties of Ti–6Al–4V fabricated by selective laser melting and electron beam melting," *Mater Des*, vol. 95, pp. 21–31, Apr. 2016, doi: 10.1016/J.MATDES.2015.12.135.
- [65] H. R. Javidrad and F. Javidrad, "Review of state-of-the-art research on the design and manufacturing of support structures for powder-bed fusion additive manufacturing," *Progress in Additive Manufacturing 2023 8:6*, vol. 8, no. 6, pp. 1517–1542, Mar. 2023, doi: 10.1007/S40964-023-00419-6.
- [66] S. Weber, J. Montero, M. Bleckmann, and K. Paetzold, "PARAMETERS ON SUPPORT STRUCTURE DESIGN FOR METAL ADDITIVE MANUFACTURING," *Proceedings of the Design Society: DESIGN Conference*, vol. 1, pp. 1145–1154, 2020, doi: 10.1017/DSD.2020.14.
- [67] X. Wang and K. Chou, "Effect of support structures on Ti-6Al-4V overhang parts fabricated by powder bed fusion electron beam additive manufacturing," *J Mater Process Technol*, vol. 257, pp. 65–78, Jul. 2018, doi: 10.1016/J.JMATPROTEC.2018.02.038.
- [68] W. Ameen, M. K. Mohammed, A. Al-Ahmari, N. Ahmed, and S. H. Mian, "Investigation of support structure parameters and their affects during additive manufacturing of Ti6Al4V alloy via electron beam melting," *Proceedings of the Institution of Mechanical Engineers, Part L: Journal of Materials: Design and Applications*, Nov. 2020, doi: 10.1177/1464420720981668;WEBSITE:WEBSITE:SAGE;WGROUP:STRING:PU BLICATION.
- [69] P. Lin, M. Wang, V. A. Trofimov, Y. Yang, and C. Song, "Research on the Warping and Dross Formation of an Overhang Structure Manufactured by Laser Powder Bed Fusion," *Applied Sciences 2023, Vol. 13, Page 3460*, vol. 13, no. 6, p. 3460, Mar. 2023, doi: 10.3390/APP13063460.
- [70] L. Newton, N. Senin, E. Chatzivagiannis, B. Smith, and R. Leach, "Feature-based characterisation of Ti6Al4V electron beam powder bed fusion surfaces fabricated at different surface orientations," *Addit Manuf*, vol. 35, p. 101273, Oct. 2020, doi: 10.1016/J.ADDMA.2020.101273.
- [71] E. Bol, G. M. Kelley, and M. Ramulu, "Characterisation of defects following MicroCT sampling inspection of specimens produced by electron beam powder bed fusion," *Virtual Phys Prototyp*, vol. 19, no. 1, Dec. 2024, doi: 10.1080/17452759.2024.2384660; JOURNAL: JOURNAL: NVPP20; REQUESTEDJ OURNAL: JOURNAL: NVPP20; PAGE: STRING: ARTICLE/CHAPTER.
- [72] H. R. Javidrad and F. Javidrad, "Review of state-of-the-art research on the design and manufacturing of support structures for powder-bed fusion additive manufacturing," *Progress in Additive Manufacturing 2023 8:6*, vol. 8, no. 6, pp. 1517–1542, Mar. 2023, doi: 10.1007/S40964-023-00419-6.
- [73] S. Ghaoui *et al.*, "Analysis of geometrical defects in overhang fabrications in electron beam melting based on thermomechanical simulations and experimental validations," *Addit Manuf*, vol. 36, p. 101557, Dec. 2020, doi: 10.1016/J.ADDMA.2020.101557.
- [74] L. D. Bobbio, S. Qin, A. Dunbar, P. Michaleris, and A. M. Beese, "Characterization of the strength of support structures used in powder bed fusion additive manufacturing of Ti-6Al-4V," *Addit Manuf*, vol. 14, pp. 60–68, Mar. 2017, doi: 10.1016/J.ADDMA.2017.01.002.
- [75] F. Ceccanti, A. Giorgetti, and P. Citti, "A Support Structure Design Strategy for Laser Powder Bed Fused Parts," *Procedia Structural Integrity*, vol. 24, pp. 667–679, Jan. 2019, doi: 10.1016/J.PROSTR.2020.02.059.

- [76] H. R. Javidrad and F. Javidrad, "Review of state-of-the-art research on the design and manufacturing of support structures for powder-bed fusion additive manufacturing," *Progress in Additive Manufacturing 2023 8:6*, vol. 8, no. 6, pp. 1517–1542, Mar. 2023, doi: 10.1007/S40964-023-00419-6.
- [77] W. Ameen, A. Al-Ahmari, and M. K. Mohammed, "Self-supporting overhang structures produced by additive manufacturing through electron beam melting," *International Journal of Advanced Manufacturing Technology*, vol. 104, no. 5–8, pp. 2215–2232, Oct. 2019, doi: 10.1007/S00170-019-04007-3/FIGURES/35.
- [78] J. Jiang, X. Xu, and J. Stringer, "Support Structures for Additive Manufacturing: A Review," *Journal of Manufacturing and Materials Processing 2018, Vol. 2, Page 64*, vol. 2, no. 4, p. 64, Sep. 2018, doi: 10.3390/JMMP2040064.
- [79] S. Ford and M. Despeisse, "Additive manufacturing and sustainability: an exploratory study of the advantages and challenges," *J Clean Prod*, vol. 137, pp. 1573–1587, Nov. 2016, doi: 10.1016/J.JCLEPRO.2016.04.150.
- [80] "Understanding build failures in Laser Powder Bed Fusion: An overview." Accessed: Jul. 22, 2025. [Online]. Available: https://www.metal-am.com/articles/understanding-build-failures-in-laser-powder-bed-fusion-an-overview/
- [81] R. Samant, R. Ranjan, K. Mhapsekar, and S. Anand, "Octree data structure for support accessibility and removal analysis in additive manufacturing," *Addit Manuf*, vol. 22, pp. 618–633, Aug. 2018, doi: 10.1016/J.ADDMA.2018.05.031.
- [82] A. Dimopoulos, M. Salimi, T. H. Gan, and P. Chatzakos, "Support Structures Optimisation for High-Quality Metal Additive Manufacturing with Laser Powder Bed Fusion: A Numerical Simulation Study," *Materials*, vol. 16, no. 22, p. 7164, Nov. 2023, doi: 10.3390/MA16227164/S1.
- [83] K. Cooper, P. Steele, B. Cheng, and K. Chou, "Contact-Free Support Structures for Part Overhangs in Powder-Bed Metal Additive Manufacturing," *Inventions 2018, Vol. 3, Page 2*, vol. 3, no. 1, p. 2, Dec. 2017, doi: 10.3390/INVENTIONS3010002.
- [84] J. Hajnys, M. Pagáč, J. Měsíček, J. Petru, and M. Król, "Influence of Scanning Strategy Parameters on Residual Stress in the SLM Process According to the Bridge Curvature Method for AISI 316L Stainless Steel," *Materials*, vol. 13, no. 7, p. 1659, Apr. 2020, doi: 10.3390/MA13071659.
- [85] L. Mugwagwa, D. Dimitrov, S. Matope, and I. Yadroitsev, "Evaluation of the impact of scanning strategies on residual stresses in selective laser melting," *International Journal of Advanced Manufacturing Technology*, vol. 102, no. 5–8, pp. 2441–2450, Jun. 2019, doi: 10.1007/S00170-019-03396-9/METRICS.
- [86] X. Gao, F. Okigami, N. Avedissian, and W. Zhang, "An experimental and modeling study on warping in additively manufactured overhang structures," *Addit Manuf*, vol. 81, p. 104017, Feb. 2024, doi: 10.1016/J.ADDMA.2024.104017.
- [87] Colibrium Additive, "EBM Point Melt Technology." Accessed: Sep. 08, 2025. [Online]. Available: https://www.colibriumadditive.com/sites/default/files/EBM%20Point%20Melt%20-%20One%20Pager%20v2.pdf
- [88] K. O'Donnell, M. J. Quintana, and P. C. Collins, "Understanding the Effect of Electron Beam Melting Scanning Strategies on the Aluminum Content and Materials State of Single Ti-6Al-4V Feedstock," *Materials*, vol. 16, no. 19, p. 6366, Oct. 2023, doi: 10.3390/MA16196366.

- [89] Y. S. Lee *et al.*, "Role of scan strategies on thermal gradient and solidification rate in electron beam powder bed fusion," *Addit Manuf*, vol. 22, pp. 516–527, Aug. 2018, doi: 10.1016/J.ADDMA.2018.04.038.
- [90] V. Viale, J. Stavridis, A. Salmi, F. Bondioli, and A. Saboori, "Optimisation of downskin parameters to produce metallic parts via laser powder bed fusion process: an overview," *International Journal of Advanced Manufacturing Technology*, vol. 123, no. 7–8, pp. 2159–2182, Dec. 2022, doi: 10.1007/S00170-022-10314-Z/METRICS.
- [91] D. Wang, Y. Yang, Z. Yi, and X. Su, "Research on the fabricating quality optimization of the overhanging surface in SLM process," *International Journal of Advanced Manufacturing Technology*, vol. 65, no. 9–12, pp. 1471–1484, Apr. 2013, doi: 10.1007/S00170-012-4271-4/METRICS.
- [92] "Arcam electron beam metal 3D printer Metal Industries." Accessed: Jul. 12, 2025. [Online]. Available: https://research.csiro.au/metals/add-manufacturing/aus-innovation/arcam-electron-beam-metal-3d-printer/
- [93] "(PDF) Characterization and optimization of lattice structures made by Electron Beam Melting." Accessed: Jul. 12, 2025. [Online]. Available: https://www.researchgate.net/publication/286677530_Characterization_and_optimiz ation of lattice structures made by Electron Beam Melting
- [94] J. R. Stojković, M. Stojković, R. Turudija, J. Aranđelović, and D. Marinkovic, "Adjustable Elasticity of Anatomically Shaped Lattice Bone Scaffold Built by Electron Beam Melting Ti6Al4V Powder," *Metals 2023, Vol. 13, Page 1522*, vol. 13, no. 9, p. 1522, Aug. 2023, doi: 10.3390/MET13091522.
- [95] "Titanium Ti6Al4V Arcam AB Catalogue PDF | Documentation technique | Brochure." Accessed: Jul. 13, 2025. [Online]. Available: https://pdf.aeroexpo.online/fr/pdf-en/arcam-ab/titanium-ti6al4v/171999-4381.html#open19664
- [96] A. Montelione, S. Ghods, R. Schur, C. Wisdom, D. Arola, and M. Ramulu, "Powder Reuse in Electron Beam Melting Additive Manufacturing of Ti6Al4V: Particle Microstructure, Oxygen Content and Mechanical Properties," *Addit Manuf*, vol. 35, p. 101216, Oct. 2020, doi: 10.1016/J.ADDMA.2020.101216.
- [97] C. De Formanoir, S. Michotte, O. Rigo, L. Germain, and S. Godet, "Electron beam melted Ti-6Al-4V: Microstructure, texture and mechanical behavior of the as-built and heat-treated material," *Materials Science & Engineering A*, vol. 652, pp. 105–119, 2015, doi: 10.1016/j.msea.2015.11.052.
- [98] M. Suard, "Caractérisation et optimisation de structures treillis fabriquées par EBM", Accessed: Jul. 22, 2025. [Online]. Available: https://theses.hal.science/tel-01241583v1
- [99] G. Mirone, R. Barbagallo, and S. Di Bella, "Effect of process parameters on the mechanical properties of a Titanium alloy fabricated by Electron Beam Melting (EBM)," *IOP Conf Ser Mater Sci Eng*, vol. 1214, no. 1, p. 012001, Jan. 2022, doi: 10.1088/1757-899X/1214/1/012001.
- [100] C. J. Smith *et al.*, "Dimensional accuracy of Electron Beam Melting (EBM) additive manufacture with regard to weight optimized truss structures," *J Mater Process Technol*, vol. 229, pp. 128–138, Mar. 2016, doi: 10.1016/J.JMATPROTEC.2015.08.028.
- [101] A. H. Chern, D. W. Galicki, T. A. Mcfalls, T. B. Fritts, and R. S. Kitchen, "DEVELOPMENT OF A POWDER BED ELECTRON BEAM ADDITIVE

- MANUFACTURING (EBAM) PARAMETER SET FOR PRINTING FULLY DENSE, CRACK-FREE, MOLYBDENUM PARTS".
- [102] B. Kirim and E. Soylemez, "Understanding Process Parameters Strategy to Simulate the Thermal Models of Electron Beam Melting," 2022, Accessed: Jul. 23, 2025. [Online]. Available: https://www.researchgate.net/publication/363819482
- [103] Yuxing Cui, "Process Monitoring and Closed Loop Control in Electron Beam Melting Process using Near Infrared Imaging Yuxing Cui," 2018.
- [104] M. A. Buhairi *et al.*, "Review on volumetric energy density: influence on morphology and mechanical properties of Ti6Al4V manufactured via laser powder bed fusion," *Progress in Additive Manufacturing 2022 8:2*, vol. 8, no. 2, pp. 265–283, Jul. 2022, doi: 10.1007/S40964-022-00328-0.
- [105] E. M. Pechlivani, L. Melidis, S. Pemas, K. Katakalos, D. Tzovaras, and A. A. Konstantinidis, "On the Effect of Volumetric Energy Density on the Characteristics of 3D-Printed Metals and Alloys," *Metals 2023, Vol. 13, Page 1776*, vol. 13, no. 10, p. 1776, Oct. 2023, doi: 10.3390/MET13101776.
- [106] S. Megahed, V. Aniko, and J. H. Schleifenbaum, "Electron Beam-Melting and Laser Powder Bed Fusion of Ti6Al4V: Transferability of Process Parameters," *Metals* 2022, *Vol.* 12, Page 1332, vol. 12, no. 8, p. 1332, Aug. 2022, doi: 10.3390/MET12081332.
- [107] A. T. Silvestri, S. Foglia, R. Borrelli, S. Franchitti, C. Pirozzi, and A. Astarita, "Electron beam melting of Ti6Al4V: Role of the process parameters under the same energy density," *J. Manuf. Process*, vol. 60, pp. 162–179, Dec. 2020, doi: 10.1016/J.JMAPRO.2020.10.065.
- [108] C. de Formanoir *et al.*, "Increasing the productivity of laser powder bed fusion: Influence of the hull-bulk strategy on part quality, microstructure and mechanical performance of Ti-6Al-4V," *Addit Manuf*, vol. 33, p. 101129, May 2020, doi: 10.1016/J.ADDMA.2020.101129.
- [109] "HandySCAN 3D|SILVER Series | Portable Professional 3D Scanner for High Accurary." Accessed: Aug. 04, 2025. [Online]. Available: https://www.creaform3d.com/en/products/portable-3d-scanners/handyscan-3d-silver-series-professional-3d
- [110] "Water Density, Specific Weight and Thermal Expansion Coefficients Temperature and Pressure Dependence." Accessed: Aug. 04, 2025. [Online]. Available: https://www.engineeringtoolbox.com/water-density-specific-weight-d 595.html
- [111] D. Khrapov, A. Koptyug, R. Surmenev, and M. Surmeneva, "Expanding manufacturability of sheet-based triply periodic minimal surfaces by electron beam powder bed fusion in Wafer theme," *Mater Today Commun*, vol. 40, p. 109580, Aug. 2024, doi: 10.1016/J.MTCOMM.2024.109580.
- [112] J. Ran, F. Jiang, X. Sun, Z. Chen, C. Tian, and H. Zhao, "Microstructure and Mechanical Properties of Ti-6Al-4V Fabricated by Electron Beam Melting," *Crystals 2020, Vol. 10, Page 972*, vol. 10, no. 11, p. 972, Oct. 2020, doi: 10.3390/CRYST10110972.
- [113] H. Gong, K. Rafi, T. Starr, and B. Stucker, "The Effects of Processing Parameters on Defect Regularity in Ti-6Al-4V Parts Fabricated By Selective Laser Melting and Electron Beam Melting".
- [114] X. Zhao, Y. Wei, R. Mansour, S. Dadbakhsh, and A. Rashid, "Effect of Scanning Strategy on Thermal Stresses and Strains during Electron Beam Melting of Inconel 625: Experiment and Simulation," *Materials*, vol. 16, no. 1, p. 443, Jan. 2023, doi: 10.3390/MA16010443/S1.

[115] D. Xie *et al.*, "A Review on Distortion and Residual Stress in Additive Manufacturing," *Chinese Journal of Mechanical Engineering: Additive Manufacturing Frontiers*, vol. 1, p. 100039, 2022, doi: 10.1016/j.cjmeam.2022.100039.

Appendix

Appendix A: Table of all manufactured parts and their process parameters

Part	EBMControl version	Build theme	Parameters							
M1	5,0	Melt	1 color - normal	Rotating hatch = 0	Contours = 0	Speed Function = 70	Default parameters	Square size = 1 mm	-	-
M2	5,0	Melt	2 colors	Rotating hatch = 0	Contours = 0	Speed Function = 70	Default parameters	Square size = 1 mm	-	-
М3	5,0	Melt	3 colors	Rotating hatch = 0	Contours = 0	Speed Function = 70	Default parameters	Square size = 1 mm	-	-
M4	5,0	Melt	4 colors	Rotating hatch = 0	Contours = 0	Speed Function = 70	Default parameters	Square size = 1 mm	-	-
P1	5,0	Point Net	1 color - normal	Current = 3.5mA	Spot time = 0.6 ms	Focus offset = 0 mA	Default parameters	Square size = 1 mm	-	-
P2	5,0	Point Net	2 colors	Current = 3.5mA	Spot time = 0.6 ms	Focus offset = 0 mA	Default parameters	Square size = 1 mm	-	-
P3	5,0	Point Net	3 colors	Current = 3.5mA	Spot time = 0.6 ms	Focus offset = 0 mA	Default parameters	Square size = 1 mm	-	-
P4	5,0	Point Net	4 colors	Current = 3.5mA	Spot time = 0.6 ms	Focus offset = 0 mA	Default parameters	Square size = 1 mm	-	-
M5	5,0	Melt	4 colors	Rotating hatch = 0	Contours = 0	Speed Function = 70	Default parameters	Square size = 0.5 mm	-	-
M6	5,0	Melt	4 colors	Rotating hatch = 0	Contours = 0	Speed Function = 70	Default parameters	Square size = 0.25 mm	-	-
M7	5,0	Melt	4 colors	Rotating hatch = 0	Contours = 0	Speed Function = 70	Default parameters	Square size = 0.1 mm	-	-
P5	5,0	Point Net	4 colors	Current = 3.5mA	Spot time = 0.6 ms	Focus offset = 0 mA	Default parameters	Square size = 0.5 mm	-	-
P6	5,0	Point Net	4 colors	Current = 3.5mA	Spot time = 0.6 ms	Focus offset = 0 mA	Default parameters	Square size = 0.25 mm	-	-
P7	5,0	Point Net	4 colors	Current = 3.5mA	Spot time = 0.6 ms	Focus offset = 0 mA	Default parameters	Square size = 0.1 mm	-	-
M8	5,0	Melt	2 colors	Rotating hatch = 0	Contours = 0	Speed Function = 70	Default parameters	Square size = 0.5 mm	-	-
M9	5,0	Melt	2 colors	Rotating hatch = 0	Contours = 0	Speed Function = 100	Default parameters	Square size = 0.5 mm	-	-
M10	5,0	Melt	2 colors	Rotating hatch = 0	Contours = 0	Speed Function = 150	Default parameters	Square size = 0.5 mm	-	-
P8	5,0	Point Net	2 colors	Current = 2.5mA	Spot time = 0.5 ms	Focus offset = 0 mA	Default parameters	Square size = 0.5 mm	-	-
P9	5,0	Point Net	2 colors	Current = 1.5mA	Spot time = 0.25 ms	Focus offset = 0 mA	Default parameters	Square size = 0.5 mm	-	-
M11	5,0	Melt	Waiting time = ?	Rotating hatch = 0	Contours = 0	Speed Function = 70	Default parameters	Square size = 6.67 mm	,	-
M12	3,2	Melt + Wafer	Waiting time = 0 s	Rotating hatch = 0	Contours = 0	Speed Function = 70	Default parameters	Square size = 6.67 mm	,	-
M13	3,2	Melt + Wafer	Waiting time = 30 s	Rotating hatch = 0	Contours = 0	Speed Function = 70	Default parameters	Square size = 6.67 mm	,	-
M14	3,2	Melt + Wafer	Waiting time = 60 s	Rotating hatch = 0	Contours = 0	Speed Function = 70	Default parameters	Square size = 6.67 mm	,	-
L01	3,2	Wafer	Normal hatch	Current = 15 mA	Speed = 4500 mm/s	Hatch distance = 0.1 mm	Contours = 0	Rotating hatch = 0	i	-
L02	3,2	Wafer	Normal hatch	Current = 15 mA	Speed = 4500 mm/s	Hatch distance = 0.3 mm	Contours = 0	Rotating hatch = 0	i	-
L03	3,2	Wafer	Quad Islands hatch	Current = 15 mA	Speed = 4500 mm/s	Hatch distance = 0.1 mm	Contours = 0	Rotating hatch = 0	Quad size = 1 mm	Quad gap = 0 mm
L04	3,2	Wafer	Quad Islands hatch	Current = 15 mA	Speed = 4500 mm/s	Hatch distance = 0.3 mm	Contours = 0	Rotating hatch = 0	Quad size = 1 mm	Quad gap = 0 mm
L05	3,2	Wafer	Radial hatch	Current = 15 mA	Speed = 4500 mm/s	Hatch distance = 0.1 mm	Contours = 0	Rotating hatch = 0	Ringh width = 5 mm	Min radius = 0 mm
L06	3,2	Wafer	Radial hatch	Current = 15 mA	Speed = 4500 mm/s	Hatch distance = 0.3 mm	Contours = 0	Rotating hatch = 0	Ringh width = 5 mm	Min radius = 0 mm
Q01	3,2	Wafer	Quad Islands hatch	Current = 15 mA	Speed = 4500 mm/s	Hatch distance = 0.1 mm	Contours = 0	Rotating hatch = 0	Quad size = 0.5 mm	Quad gap = 0.25 mm
Q03	3,2	Wafer	Quad Islands hatch	Current = 15 mA	Speed = 4500 mm/s	Hatch distance = 0.1 mm	Contours = 0	Rotating hatch = 0	Quad size = 1 mm	Quad gap = 0.25 mm
Q05	3,2	Wafer	Quad Islands hatch	Current = 15 mA	Speed = 4500 mm/s	Hatch distance = 0.1 mm	Contours = 0	Rotating hatch = 0	Quad size = 0.75 mm	Quad gap = 0.1mm
Q06	3,2	Wafer	Quad Islands hatch	Current = 15 mA	Speed = 4500 mm/s	Hatch distance = 0.5 mm	Contours = 0	Rotating hatch = 0	Quad size = 0.75 mm	Quad gap = 0.1mm
Q07	3,2	Wafer	Quad Islands hatch	Ourrent = 15 mA	Speed = 4500 mm/s	Hatch distance = 0.1 mm	Contours = 0	Rotating hatch = 0	Quad size = 0.75 mm	Quad gap = 0.5 mm
Q09	3,2	Wafer	Quad Islands hatch	Ourrent = 15 mA	Speed = 4500 mm/s	Hatch distance = 0.25 mm	Contours = 0	Rotating hatch = 0	Quad size = 0.5 mm	Quad gap = 0.1 mm
Q10	3,2	Wafer	Quad Islands hatch	Ourrent = 15 mA	Speed = 4500 mm/s	Hatch distance = 0.25 mm	Contours = 0	Rotating hatch = 0	Quad size = 1 mm	Quad gap = 0.1 mm
Q13	3,2	Wafer	Quad Islands hatch	Ourrent = 15 mA	Speed = 4500 mm/s	Hatch distance = 0.25 mm	Contours = 0	Rotating hatch = 0	Quad size = 0.75 mm	Quad gap = 0.25 mm
Q14	3,2	Wafer	Quad Islands hatch	Ourrent = 15 mA	Speed = 4500 mm/s	Hatch distance = 0.25 mm	Contours = 0	Rotating hatch = 0	Quad size = 0.75 mm	Quad gap = 0.25 mm
Q15	3,2	Wafer	Quad Islands hatch	Ourrent = 15 mA	Speed = 4500 mm/s	Hatch distance = 0.25 mm	Contours = 0	Rotating hatch = 0	Quad size = 0.75 mm	Quad gap = 0.25 mm
Q16	3,2	Wafer	Quad Islands hatch	Current = 15 mA	Speed = 4500 mm/s	Hatch distance = 0.25 mm	Contours = 0	Rotating hatch = 0	Quad size = 0.75 mm	Quad gap = 0.25 mm

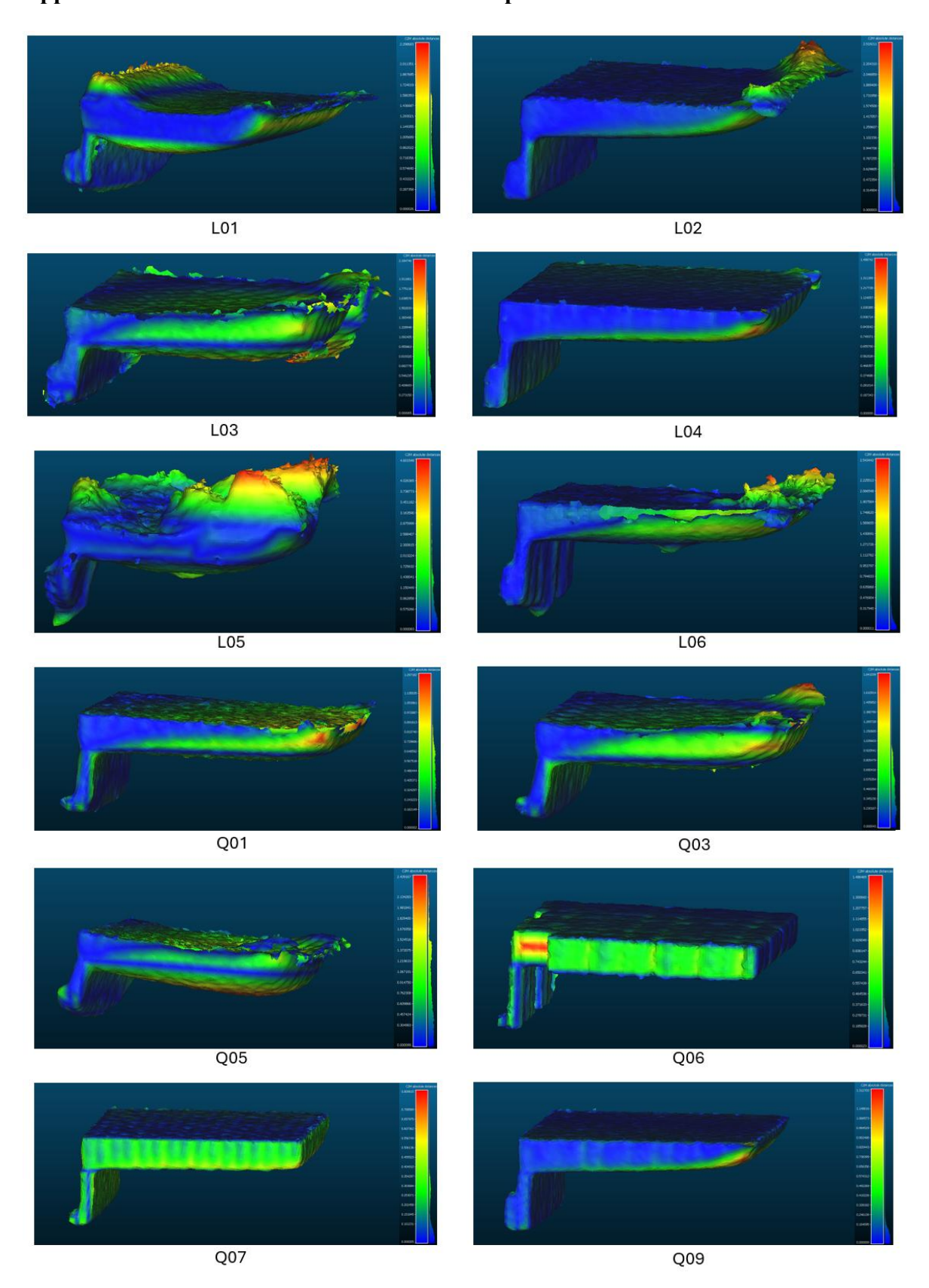
Appendix B: Table of parts with their measured density and porosity

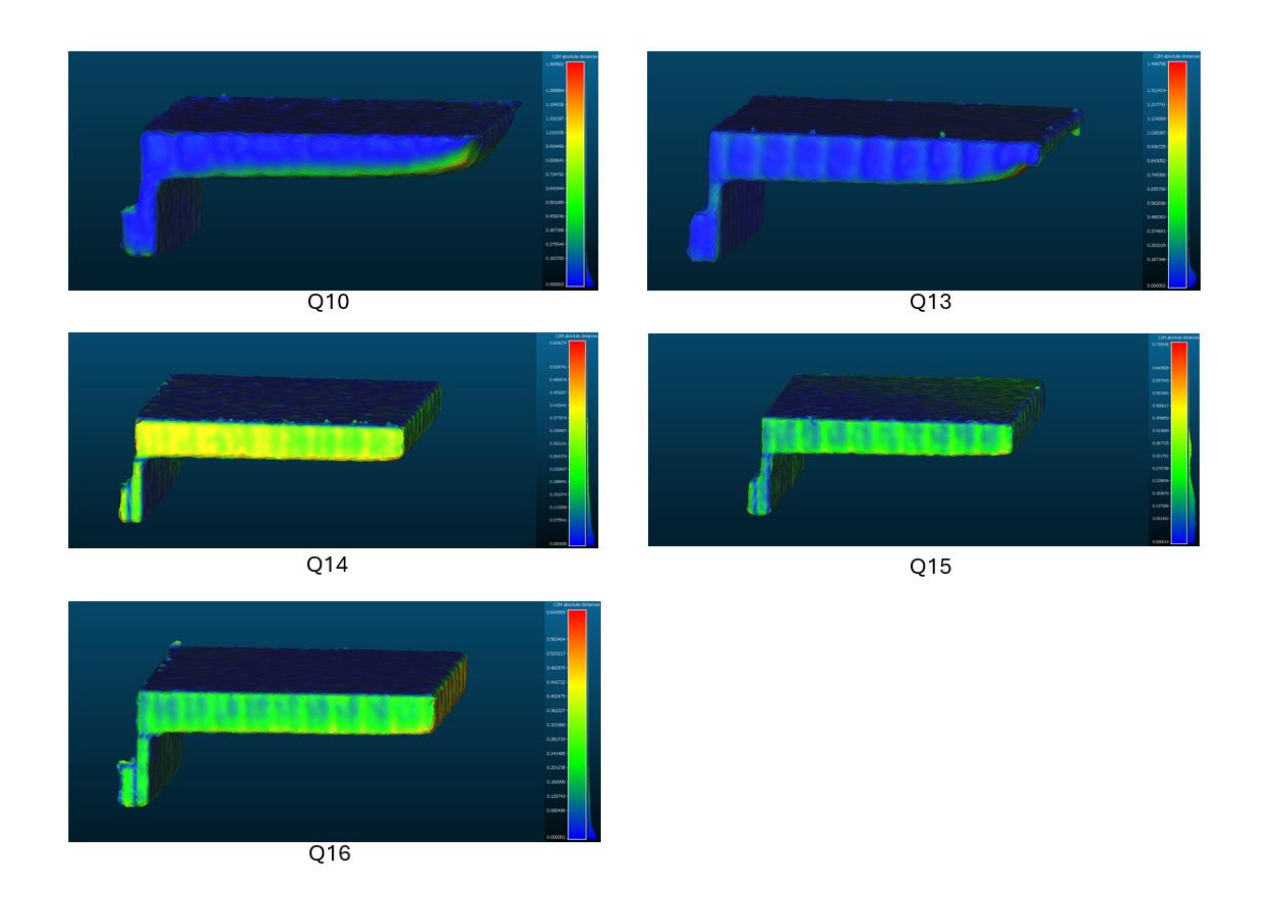
Sample	Density (g/cm3)	Density (%)	Porosity (%)
M1	4.369	98.634	1.366
M2	4.307	97.222	2.778
M3	4.285	96.738	3.262
M4	4.334	97.838	2.162
P1	4.275	96.501	3.499
P2	4.319	97.489	2.511
Р3	4.288	96.793	3.207
P4	4.338	97.915	2.085
M5	4.206	94.945	5.055
M6	4.189	94.555	5.445
M7	4.200	94.813	5.187
P5	4.284	96.701	3.299
P6	4.199	94.786	5.214
P7	4.299	97.035	2.965
M8	4.336	97.876	2.124
M9	4.215	95.148	4.852
M10	3.861	87.162	12.838
P8	4.350	98.202	1.798
P9	3.325	75.067	24.933
P10	-	-	-
M11	4.311	97.319	2.681
M12	4.402	99.368	0.632
M13	4.372	98.695	1.305
M14	4.389	99.078	0.922
L01	4.391	99.121	0.879
L02	4.154	93.765	6.235
L03	4.376	98.784	1.216
L04	3.946	89.067	10.933
L05	4.298	97.031	2.969
L06	4.057	91.580	8.420
Q01	4.125	93.112	6.888
Q02	-	-	-
Q03	4.298	97.016	2.984
Q04	-	-	-
Q05	4.360	98.411	1.589
Q06	2.952	66.640	33.360
Q07	3.707	83.674	16.326
Q08	-	-	-
Q09	3.736	84.323	15.677
Q10	3.877	87.514	12.486
Q11	-	-	-
Q12	-	-	-
Q13	3.482	78.611	21.389
Q14	3.479	78.532	21.468
Q15	3.424	77.296	22.704
Q16	3.434	77.508	22.492

Appendix C: Table of parts with their measured geometric deviation (Mean, SD, RMS and Max)

Sample	Mean (mm)	SD (mm)	RMS (mm)	Max (mm)
L01	0.565 0.457		0.727	2.299
L02	0.326	0.380	0.501	2.519
L03	0.570	0.456	0.730	2.185
L04	0.188	0.196	0.271	1.499
L05	0.922	0.896	1.286	4.602
L06	0.278	0.354	0.450	2.543
Q01	0.344	0.237	0.418	1.297
Q02	-	-	-	-
Q03	0.416	0.290	0.507	1.841
Q04	-	-	-	-
Q05	0.820	0.601	1.017	2.439
Q06	0.178	0.163	0.241	1.486
Q07	0.146	0.128	0.194	0.810
Q08	-	-	-	-
Q09	0.137	0.175	0.222	1.313
Q10	0.117	0.162	0.200	1.470
Q11	-	-	-	-
Q12	-	-	-	-
Q13	0.162	0.214	0.268	1.499
Q14	0.125	0.109	0.166	0.604
Q15	0.161	0.114	0.197	0.735
Q16	0.101	0.109	0.148	0.644

Appendix D: Scalar fields between all scanned part and their CAD





Appendix E: Pictures of all manufactured parts

